Measurement and Analysis of Coherent Synchrotron Radiation Effects at FLASH

Dissertation

zur Erlangung des Doktorgrades
des Departments Physik
der Universität Hamburg

vorgelegt von

Bolko Beutner
aus Hamburg

Hamburg
2007

Gutachter der Dissertation	Prof. Dr. Jörg Roßbach Prof. Dr. Götz Heinzelmann
Gutachter der Disputation	Prof. Dr. Jörg Roßbach Prof. Dr. Klaus Fredenhagen
Datum der Disputation	13. November 2007
Vorsitzender des Prüfungsausschusses	Dr. Hans Dierk Rüter
Vorsitzender des Promotionsausschusses	Prof. Dr. Günter Huber
Dekan der Fakultät für Mathematik, Informatik und Naturwissenschaften	Prof. Dr. Arno Frühwald

Abstract

The vacuum-ultra-violet Free Electron Laser in Hamburg (FLASH) is a linac driven SASE-FEL. High peak currents are produced using magnetic bunch compression chicanes. In these magnetic chicanes, the energy distribution along an electron bunch is changed by effects of Coherent Synchrotron Radiation (CSR). Energy changes in dispersive bunch compressor chicanes lead to transverse displacements along the bunch. These CSR induced displacements are studied using a transverse deflecting RF-structure.

Experiments and simulations concerning the charge dependence of such transverse displacements are presented and analysed. In these experiments an over-compression scheme is used which reduces the peak current downstream the bunch compressor chicanes. Therefore other self interactions like space charge forces which might complicate the measurements are suppressed.

Numerical simulations are used to analyse the beam dynamics under the influence of CSR forces. The results of these numerical simulations are compared with the data obtained in the over-compression experiments at FLASH.

Zusammenfassung

Der vakuum ultraviolett freie Elektronen Laser in Hamburg (FLASH) ist ein durch einen Linearbeschleuniger betriebener SASE-FEL. Die hohen Spitzenströme werden in magnetischen Bunchkommpressionsschikanen erzeugt. In diesen magnetischen Schikanen wird die Energieverteilung entlang des Elektronenpakets durch Effekte der kohärenten Synchrotronstrahlung (CSR) geändert. Energieänderungen in dispersiven Bunchkommpressionsschikanen führen zu transversalen Verschiebungen entlang des Teilchenpakets. Diese, durch CSR erzeugten, Verschiebungen werden mit Hilfe einer transversal ablenkenden HF-Struktur studiert.

Experimente und Simulationen welche sich mit der Ladungsabhängigkeit dieser transversalen Verschiebungen befassen werden vorgestellt und analysiert. Diese Experimente basieren auf einem Überkompressions Schema welches den Spitzenstrom hinter den Bunchkompressoren reduziert. Daher sind andere Selbstwechselwirkungen, welche die Messungen verkomplizieren könnten, unterdrückt.

Numerische Simulationen wurden genutzt um die Strahldynamik unter dem Einfluss von CSR Kräften zu untersuchen. Die Resultate dieser numerischen Berechnungen werden mit den Daten von Überkompressionsexperimenten bei FLASH verglichen.

Contents

1 Introduction

Single pass free electron lasers are a promising and challenging technology to generate high quality radiation for various applications. Such free electron lasers are driven by bunches of highly relativistic electrons interacting with magnetic devices called undulators. These electron beams need a very good beam quality in order to meet the requirements of the lasing process. One such requirement is the high charge density of the electron beam. High charge densities, however, give rise to strong electromagnetic fields generated by the beam itself. Interactions of these fields with the electron beam distort the beam quality. Precise knowledge of these self-interactions is therefore mandatory for the successful design and operation of a free electron laser. Direct experimental studies of self-interactions are challenging. Beam diagnostic systems are not able to measure all properties of an electron beam and are also not available at all positions along the linac. This lack of information can be supplemented by numerical simulations. They are also needed to understand the beam dynamics to find ways of improvement. Numerical simulations are, therefore, a powerful tool in the analysis of the beam dynamics at present free electron laser facilities as well as in the design of future accelerators.

One of these self-interactions, the effect of *coherent synchrotron radiation* (CSR), is the focus of this thesis. Particles deflected in magnetic fields emit synchrotron radiation and the resulting energy changes, especially in the longer, coherently emitted wavelength regime, have a significant impact on the beam dynamics and the performance of a free electron laser.

This thesis is split in to two parts. First, a numerical study of the effects of coherent synchrotron radiation on the beam and the corresponding development of numerical tools were performed. Second, experimental studies of such effects were done at the FLASH facility at DESY, Hamburg. Dedicated experiments to measure CSR effects, using a transverse deflecting RF-structure, were done and compared with simulations.

The unique properties of the FLASH linac allowed rather direct and novel observations of coherent synchrotron radiation effects on the electron beam. From the comparison of the experimental and the numerical results, one gains important information on the beam dynamics, the quality of the numerical tools, and the abilities of the diagnostic installed in the electron linac.

The FLASH based studies provide important data on the optimisation of forthcoming projects like the European XFEL in Hamburg.

In Chapter 2 an introduction to free electron lasers and the FLASH facility at DESY is given. Beam dynamics in general and at FLASH are discussed in Chapter 3. After a short introduction, concerning mostly the longitudinal dynamics and self-interactions of the bunch, the beam dynamics at FLASH are discussed in greater detail. Finally an

experimental setup to study CSR effects at FLASH is described, and analysed.

An important part of this thesis is the numerical analysis of the beam dynamics which is presented in Chapter 4. After a brief overview of numerical beam dynamics simulations, and an introduction to different tracking codes, modifications made to the *ASTRA* tracking code are presented and compared with established codes.

Finally, in Chapter 5, measurements at FLASH using the setup from Chapter 3, are presented. After a description of the experimental setup and a summary of the measured data the data analysis and the results are given and compared with the results of numerical simulations.

2 FLASH

2.1 Free Electron Lasers

Synchrotron radiation is a powerful diagnostic tool applied in disciplines ranging from physics, chemistry, and biology to material sciences, geophysics, and medicine. It encompasses a broad spectrum, ranging from the infrared to the hard X-ray regime. Synchrotron radiation is generated when high energy electrons are deflected in magnetic fields.

In the first generation of synchrotron light sources the synchrotron light was generated in bending magnets. Higher brilliance[1] can be reached using periodically alternating transverse magnetic fields as in wigglers or undulators.

In an undulator, the electrons are forced on an oscillating orbit, and they emit spontaneous radiation with a narrow bandwidth around a resonance wavelength λ_{photon} given by

$$\lambda_{\text{photon}} = \frac{\lambda_{\text{undulator}}}{2\gamma^2}\left(1+\frac{K^2}{2}\right), \tag{2.1}$$

$$\gamma = \frac{E}{m_e c^2}, \tag{2.2}$$

$$K = \frac{eB_{\text{undulator}}\lambda_{\text{undulator}}}{2\pi m_e c}, \tag{2.3}$$

and higher harmonics thereof [Mad71]. Here, E is the electron energy, e the electron charge, m_e the electron rest mass, c the speed of light in vacuum, $\lambda_{\text{undulator}}$ the undulator period, $B_{\text{undulator}}$ is the peak transverse deflecting magnetic field in the undulator, and K the undulator parameter.

In a free-electron laser (FEL), considered to be the fourth generation of synchrotron light sources, the electrons radiate coherently, thus increasing the dependence of the output power on the number of electrons N_e from $\sim N_e$ to $\sim N_e^2$. As a result, one gets increased peak brilliance by up to ~ 10 orders of magnitude. While the average

[1] For many experiments the relevant figure of merit is the *brilliance* (or spectral brightness). Brilliance is defined as a function of frequency given by the number of photons emitted by the source per unit time into a unit solid angle, per unit surface of the source, and into a unit bandwidth of frequencies around the given one. The units in which it is usually expressed are photons/s/mm2/mrad2/0.1% BW, where 0.1% BW denotes a bandwidth of $10^{-3}\omega$ centered around the frequency ω. As one can appreciate from the definition, brilliance puts a premium not only on the photon flux (photons per second in a given bandwidth), but also on the high phase space density of the photons, i.e. on being radiated out of a small area and with high directional collimation. It thus also determines to what extent the radiation can be focused onto an experiment.

brilliance is $\sim$ 4 orders of magnitude higher compared to spontaneous radiation light sources[2]. Additionally the radiation pulses in a FEL are much shorter (on the order of 10 to 100 fs) and the radiation is transversely coherent.

An overview of the peak brilliance for different light sources is given in Fig. 2.1.

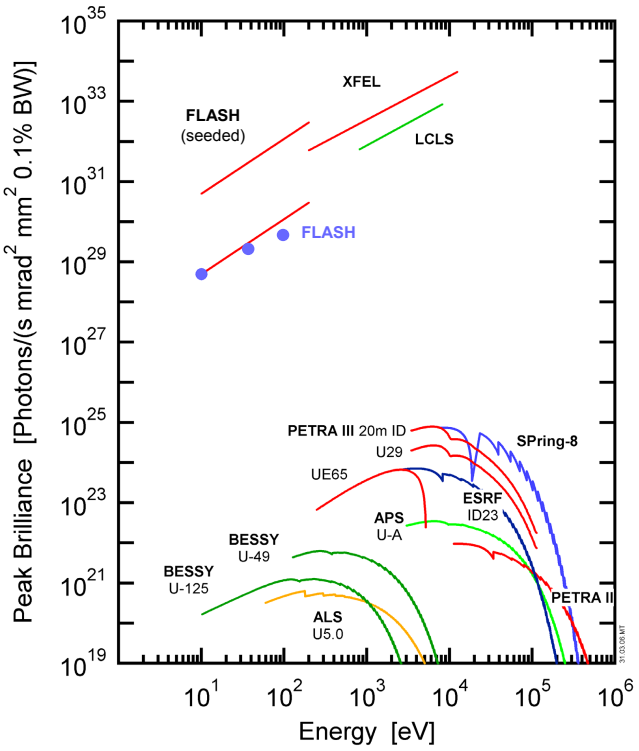

Figure 2.1: Peak brilliance of FELs versus 3rd generation SR light sources. Blue spots show experimental performance of FLASH (figure from [XFEL]).

In an oscillator FEL an optical cavity similar to that in a classical laser is used to amplify the synchrotron radiation light in many reflection cycles. This works only for wavelengths in the infrared, visible, and soft ultraviolet regime. No suitable mirrors are available for shorter wavelengths. Therefore, FELs in the X-ray regime need to achieve laser amplification and saturation within a single pass of the electrons through the undulator.

The interaction of the undulator radiation with the electron bunch produces a longitudinal density modulation inside the electron bunch of the order of the radiation wavelength, called micro bunching. These density modulations build up exponentially, which leads to an exponential growth of the coherent radiation along the undulator.

[2]The peak power scales like $P_{\mathrm{peak}} \sim N^2$, the average power goes with the repetition rate f_{rep} like $P_{\mathrm{ave}} \sim N^2 \cdot f_{\mathrm{rep}}$. Typical numbers for FELs are of the order $f_{\mathrm{rep}} \sim 10^3$ Hz (FLASH/XFEL) and synchrotron light sources $f_{\mathrm{rep}} = 250 - 500$ MHz (Petra III).

The micro bunching process can be started through an interaction of the electron bunch with an external laser inside the undulator. The external (seed) laser imprints a density modulation on the bunch which is amplified if the resonance condition Eq. 2.1 is fulfilled. No laser for a seeding process is available in the X-ray regime, so one relies on self-amplified spontaneous emission (SASE). In the SASE process the spontaneous radiation from the undulator is used to seed the same electron bunch which emitted the radiation [Bon84][Sal99] (see Fig. 2.2).

The lasing process depends critically on the quality of the driving electron beam. In case of a mono-energetic beam matching the resonance energy and neglecting three-dimensional effects, the radiation energy gain $G(z)$ increases exponentially along the undulator [Sal99]

$$G(z) \propto \exp\left(\frac{z}{L_G}\right) \quad \text{for } z \gg L_G \tag{2.4}$$

and the gain length L_G is proportional to

$$L_G \propto \left(\frac{\sigma_t^2}{I_0}\right)^{1/3}. \tag{2.5}$$

The quantity σ_t denotes the transverse RMS beam size and I_0 is the peak current. A high peak current and a small transverse beam size are needed to obtain a short gain length.

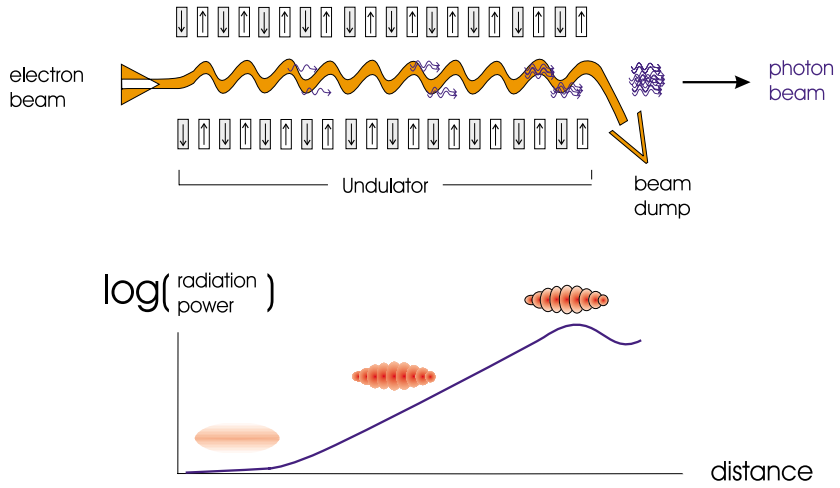

Figure 2.2: Electrons and radiation interact along the undulator. Micro bunches develop in the longitudinal bunch profile and the radiation power grows exponentially (figure taken from [TESLA]).

Realistic beams are not mono-energetic and three dimensional properties like the transverse emittance cannot be neglected. A beam energy spread induces a longitudinal velocity spread, which drastically increases the gain length if it exceeds a critical limit

[Sal99]. This is, because an FEL operates like a narrow-band amplifier. Due to Eq. 2.1, a large beam energy width corresponds to a large spread of wavelength that cannot be amplified simultaneously in an FEL. The transverse beam emittance leads to additional longitudinal velocity spread, since particles with the same energies but different angles with respect to the design orbit have different longitudinal velocities. This velocity spread can be considered as an additional contribution to the energy spread. Assuming a Gaussian transverse phase space distribution, this contribution is proportional to the square of the emittance [Sal99]. Therefore, an electron beam with a small energy spread and a small transverse emittance is essential to drive a free electron laser.

2.2 FLASH

FLASH is a user facility for soft X-ray FEL radiation at DESY, Hamburg [TTF02]. It is the second phase of the TESLA Test Facility (TTF) which provided a proof of principle of self-amplified spontaneous emission (SASE) in the wavelength range 80−120 nm [And00]. FLASH demonstrated SASE operation in 2005 at a wavelength of 32 nm [Ayv06]. In 2007, FLASH operates in a wavelength range from 13 − 60 nm [Ros06][Ack07]. Shorter wavelengths require additional accelerating modules (ACC6), foreseen for 2007.

In the final stage, the electron beam is accelerated up to 1GeV by six accelerating modules, leading to a radiation wavelength of 6.4 mm or 194 eV photon energy.

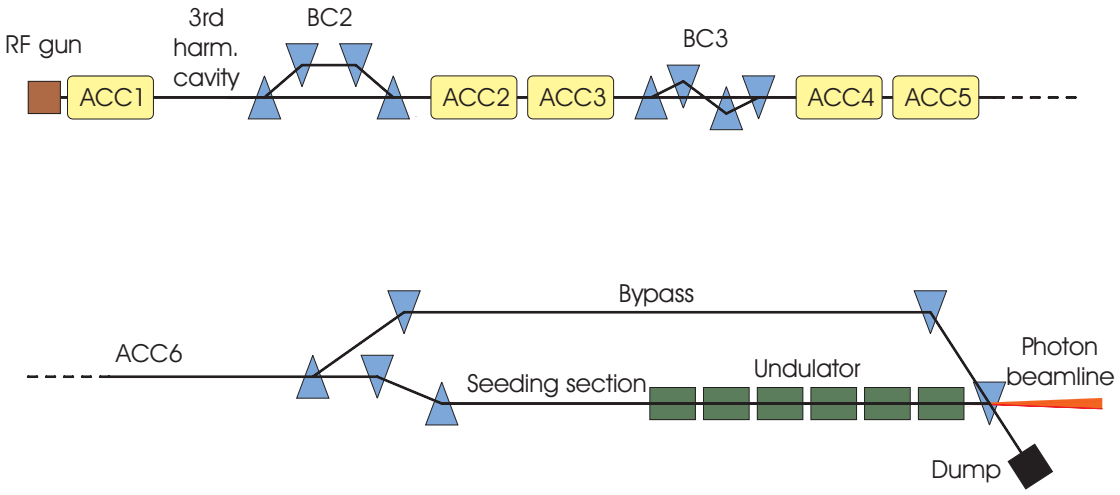

Figure 2.3: Sketch of FLASH. The blue triangles indicate dipole magnets, the yellow boxes TESLA acceleration modules. The accelerating modules ACC6, ACC7, and the 3rd harmonic cavity as well as the seeding beam line are not installed in 2007.

The schematic layout of FLASH is shown in Fig. 2.3. The electron beam of about 1 nC is produced in the 1.5-cell RF gun cavity [Kra04][Sch04] and accelerated by a TESLA type module[3] to around 130 MeV. In the following bunch compressor chicane, called BC2 for historical reasons, the bunch length can be reduced by about a factor of 10 [Lim02]. Before the second compression step in BC3 the electrons are accelerated in modules ACC2 and ACC3 to an energy of 380 MeV. In the second bunch compressor (BC3) the bunch length is further reduced by about a factor of 4. The design of BC2 and BC3 are different. While BC2 is a simple four-bend-chicane, BC3 has a S-shape and consists of six dipoles of equal bending strength (see Fig. 2.4 and [Stu04]). In total the electron bunches are compressed from a length of 2 mm RMS at the exit of the gun to approximately 50 μm RMS. FLASH parameters are summarised in Appendix A.

[3] A cryomodule consists of eight superconducting niobium RF cavities (comprising nine resonator cells each) which work at a frequency of 1.3 GHz.

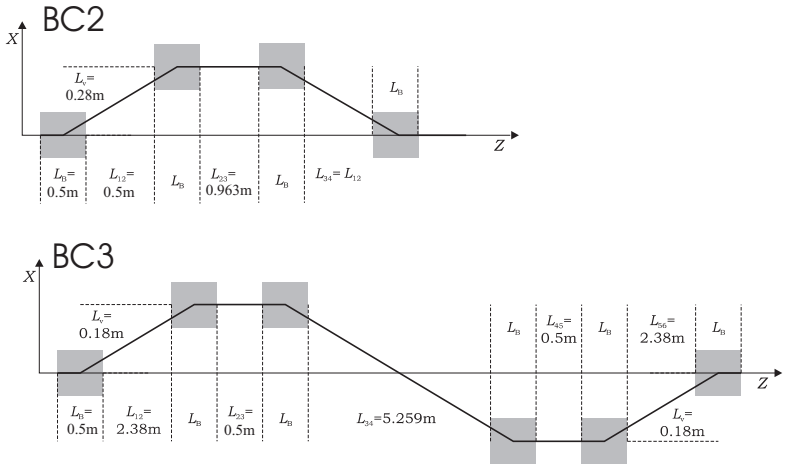

Figure 2.4: Sketch of the bunch compressors chicanes BC2 and BC3 in FLASH.

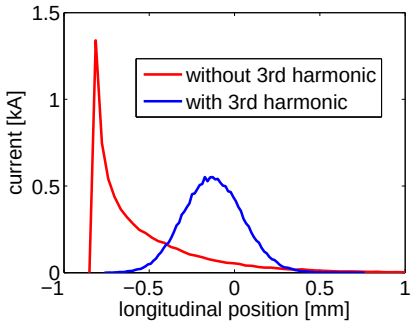

Figure 2.5: Examples of current profiles of the electron bunches with and without the 3rd harmonic cavity. Bunch head to the left.

The 30 m long planar undulator [Pfl00] consists of NdFeB permanent magnets and has a fixed gap of 12 mm, a period length of $\lambda_{\text{undulator}} = 27.3$ mm, and a peak magnetic field $B_{\text{undulator}} = 0.47$ T which lead to an undulator parameter of $K = 1.2$.

A collimator section protects the undulator by removing particles with energy deviation larger than $\pm 3\%$ or with large betatron amplitudes. It is also possible to bypass the collimator and undulator to facilitate machine commissioning and tests of accelerator components. Finally, a dipole magnet deflects the electron beam into a dump, while the FEL radiation propagates to the experimental hall.

The nominal FLASH operation mode with 200 fs long pulses of FEL radiation, based on linearised bunch compression, is not available due to the lack of a key element - a 3rd harmonic RF cavity. For this reason FLASH is operating in the nonlinear compression mode (see section 3.1.5) with 30 fs long radiation pulses until the installation of the

3rd harmonic cavity. Nonlinear compression leads to the formation of a short high-current leading peak in the density distribution that produces FEL radiation. The main advantage of this operation mode is the short radiation pulse length generated by the sharp high current spike which is favourable for certain synchrotron radiation experiments. Current profiles of the electron bunches with and without the 3rd harmonic cavity are shown in Fig. 2.5. Compression parameters are summarised in Tab. A.2.

3 Beam Dynamics

3.1 Bunch Compression

3.1.1 Introduction

Linac-based free-electron lasers require very short, (< 100 fs) high-brightness electron beams with peak currents on the order of kilo-amperes. These bunches cannot be produced directly in electron guns because space charge forces would destroy the beam quality within a short distance. So it is necessary to start with a low intensity bunch with a peak current of a few tens of Amperes, accelerate it to energies where the space charge forces are weakened sufficiently by the $1/\gamma^2$ scaling, and then reduce the bunch length to increase the peak current.

To compress a bunch longitudinally, the time of flight through some section must be shorter for the tail of the bunch than it is for the head. The usual technique starts out by introducing a correlation between the longitudinal position of the particles in the bunch and their energy using a radio frequency (RF) accelerating system. At high energies the velocity spread induced by such an energy chirp is negligible, due to relativistic effects. The different path lengths followed by the head and tail of the bunch through a dispersive section, made up of four dipole magnets, compress the bunch length.

Figure 3.1 illustrates the principle: The longitudinal phase space is represented by a tilted ellipse after applying the energy chirp. In this case we assume a linear correlation between the energy of a particle and the longitudinal position. During the compression the particles with lower energies fall back, thus shearing the ellipse. Minimal bunch length is achieved when the longitudinal phase space ellipse is vertical. The minimal bunch length achievable is determined by the conservation of the total volume (emittance) in the longitudinal phase space.

3.1.2 Dispersive Beam Lines

To describe a particle state we use a coordinate system which moves along the orbit of a reference particle with the design energy E and momentum p (Fig. 3.2). The coordinates x and y yield the distance to the design orbit while x' and y' represent the angle relative to the design momentum. s is the longitudinal distance to the reference particle and $\delta = \Delta E/E$ is the normalised energy difference from the design energy E.

The transformation of the phase space coordinates $(x, x', y, y', s, \delta)$ of an electron can

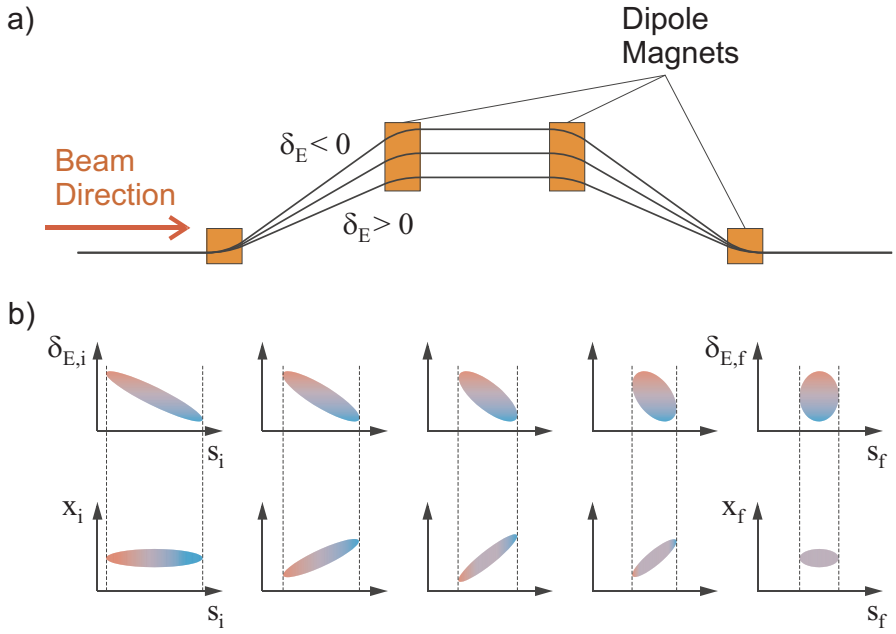

Figure 3.1: Longitudinal bunch compression in a 4-bending-magnet chicane.

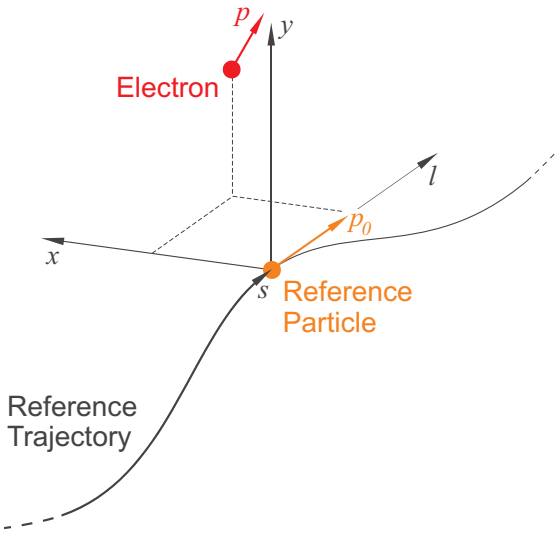

Figure 3.2: The distance of a particle to the orbit of a reference particle of design energy and momentum is used as a spatial coordinate x and y respectively. The transverse momentum p_x, being proportional to the angle $x' = \frac{dx}{ds}$ between the particle momentum p and the tangent to the design orbit at s is the momentum coordinate in the phase space representation of the particle state. s is the longitudinal distance to the reference particle.

be described to first order by a linear matrix formalism [Bro82]:

$$\begin{pmatrix} x_f \\ x'_f \\ y_f \\ y'_f \\ s_f \\ \delta_f \end{pmatrix} = \mathbf{R} \begin{pmatrix} x_i \\ x'_i \\ y_i \\ y'_i \\ s_i \\ \delta_i \end{pmatrix} \tag{3.1}$$

The Matrix elements R_{16} to R_{56} of $\mathbf{R}$ are called the dispersion. The dispersion describes how a phase space coordinate changes when the energy differs from the design energy E. To first order they are defined as the slope between a phase space coordinate and the relative energy deviation δ, as

$$R_{16} = \frac{\Delta x}{\delta} \tag{3.2}$$

$$R_{26} = \frac{\Delta y}{\delta} \tag{3.3}$$

$$R_{36} = \frac{\Delta x'}{\delta} \tag{3.4}$$

$$R_{46} = \frac{\Delta y'}{\delta} \tag{3.5}$$

$$R_{56} = \frac{\Delta s}{\delta}. \tag{3.6}$$

The matrix elements of the dispersion are called transverse (x and y), angular (x' and y') and longitudinal (s) dispersion.

The longitudinal position changes induced by the longitudinal dispersion are of special interest in the bunch compression process. In general, considering higher order contributions, any curved beam line section introduces a path length difference for particles with a relative energy deviation δ:

$$\Delta s = R_{56} \cdot \delta + T_{566} \cdot \delta^2 + U_{5666} \cdot \delta^3 + \cdots \tag{3.7}$$

3.1.3 RF Acceleration

We focus now on the details of bunch compression starting with the induced energy correlation. The energy of a particle after acceleration in an RF section with phase ϕ, peak RF voltage V, and initial energy E_0, is given by

$$E(s) = eV \cos(\phi + \frac{2\pi}{\lambda} s) + E_0, \tag{3.8}$$

where s is the longitudinal position in the bunch and $E = E(0)$ is the beam energy.

The RF phase of maximum acceleration $\phi = 0°$ is called *on crest*. For $\pi < \phi < 0$ (Fig. 3.3) the bunch head gains less energy than the bunch tail .

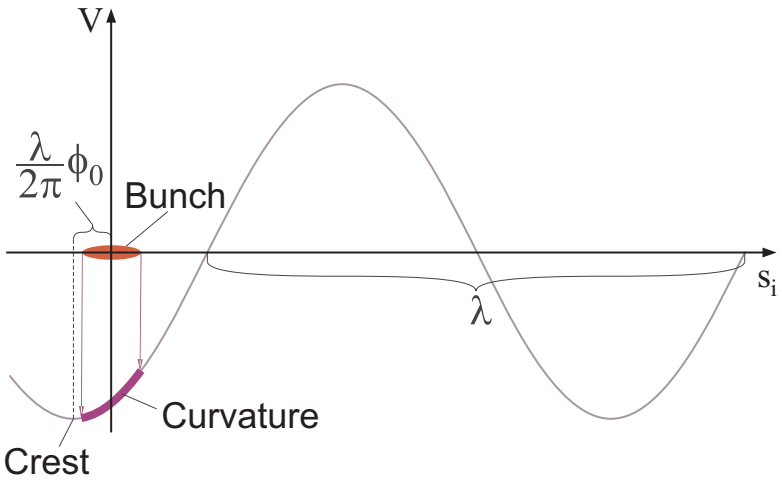

Figure 3.3: The longitudinal phase space is shaped by the sinusoidal time dependence of the RF wave. The electrons undergo an acceleration depending on the longitudinal position l_i with respect to the bunch centre. Leading particles experience a lower voltage V than the trailing ones with the appropriate phase offset ϕ_0.

Since the bunch length (typically in the order of a mm or less) is much smaller than the RF wavelength ($\lambda = 23.1$ cm for $\nu = 1.3$ GHz) we expand Eq. 3.8:

$$E(s) = E(0) + E'(0)s + \frac{1}{2}E''(0)s^2 + \mathcal{O}(s^3) \tag{3.9}$$

$$= E_0 + eV\left(\cos\phi - \frac{2\pi}{\lambda}\sin(\phi)s - \frac{2\pi^2}{\lambda^2}\cos(\phi)s^2\right), \tag{3.10}$$

with a beam energy $E = E(0) = E_0 + eV\cos\phi$.

The relative energy deviation δ of a particle with longitudinal displacement s after RF acceleration is

$$\delta_{\mathrm{RF}} = \frac{\Delta E}{E} = \frac{E(s) - E(0)}{E} \tag{3.11}$$

$$= -\frac{2\pi eV}{E\lambda}\sin\phi s - \frac{2\pi^2 eV}{E\lambda^2}\cos\phi s^2 \tag{3.12}$$

$$\approx As + Bs^2, \tag{3.13}$$

introducing the linear chirp factor $A = -\frac{2\pi eV}{E\lambda}\sin\phi$. In the following, only the linear chirp A is considered, nonlinearities are omitted.

To obtain the total relative energy offset to the reference one defines

$$\delta_E = As + \delta_i \tag{3.14}$$

where δ_i is by definition, not correlated along the bunch length. It is the contribution to the net energy spread due to the initial (random) intrinsic energy spread within the beam. This uncorrelated energy spread is, for instance, determined by space charge interactions in the injector area.

3.1.4 Compression in Linear Approximation

The longitudinal position of a particle after a dispersive section (i.e. a bunch compressor chicane) is (see Eq. 3.1)

$$s_f = s_i + R_{56}\delta. \tag{3.15}$$

Therefore, the difference $s_f - s_i \approx R_{56}\delta$ is the distance a particle moved in the co-moving reference system of the ideal particle.

We ignore radiation effects and bunch interactions with the vacuum chamber walls, and assume that the particle energy has not been changed in the bend system. Rewriting s_f with the linear chirp factor A, we have

$$s_f = s_i + (1 + AR_{56})s_i + R_{56}\delta_i. \tag{3.16}$$

Taking an ensemble average over all particles in the bunch using the notation $\langle ... \rangle$, and using the definition $\langle s\delta_i \rangle = 0$, the second moment of the distribution ($\sigma_{s_f} \equiv \sqrt{\langle (s_f - \langle s_f \rangle)^2 \rangle}$) is the final RMS bunch length

$$\sigma_{s_f} = \sqrt{(1 + AR_{56})^2\sigma_{s_i}^2 + R_{56}^2\sigma_{\delta_i}^2}, \tag{3.17}$$

where $\sigma_{s_i} \equiv \sqrt{\langle s_i^2 \rangle}$ is the initial RMS bunch length, and $\sigma_{\delta_i} \equiv \sqrt{\langle \delta_i^2 \rangle}$ is the RMS relative intrinsic energy spread (uncorrelated component).

For 'full' compression where $1 + AR_{56} = 0$, the final bunch length is limited by the product of intrinsic energy spread (compare Fig. 3.1), σ_{δ_i}, and the R_{56} of the compressor:

$$\check{\sigma}_{s_f} \approx |R_{56}|\sigma_{\delta_i}. \tag{3.18}$$

With a high-brightness RF-photo cathode source, the intrinsic energy spread is extremely small and the bunch length is simply scaled from its original length as

$$\sigma_{s_f} \approx |1 + AR_{56}|\sigma_{s_i} = \sigma_{s_i}/C, \tag{3.19}$$

where C is the compression factor, $C \equiv \sigma_{s_i}/\sigma_{s_f}$, with C typically $\gg 1$. The limit of very short bunches in this case is usually due to higher order aberrations in the longitudinal phase space, which will be discussed later.

In addition to bunch length compression, the intrinsic (uncorrelated) relative energy spread is magnified by the compression factor: $\sigma_{\delta_f} = C\sigma_{\delta_i}$, preserving the longitudinal emittance. In FEL applications this final intrinsic energy spread can be as important as the transverse emittance.

3.1.5 Non-Linearities in Bunch Compression

The situation is different if one considers nonlinear contributions to the longitudinal beam dynamics. An example is the evolution of longitudinal phase space during bunch compression shown in Fig. 3.4, after a linac section and magnetic chicane.

After the chicane, the non-linearity of the chirp, together with the T_{566} of the chicane, dominates the shape of the bunch and a sharp spike develops at the head of the charge distribution with a width depending on the intrinsic energy spread (right plot). This sharp spike typically contains around $10-15\%$ of the particles of the bunch. This spike can also lead to a local transverse emittance dilution [RLi00], as described in the next sections.

Recalculating the final bunch length (compare Eq. 3.17) including the second order chirp factor B (Eq. 3.13) and including higher order longitudinal dispersion T_{566} (Eq. 3.7) one obtains with $|\delta_i| << 1$ and $|\frac{T_{566}}{R_{56}}| \sim 1$

$$\sigma_{s_f} = \sqrt{(1 + AR_{56} + 2s_i(BR_{56} + T_{566}A^2))^2\sigma_{s_i}^2 + R_{56}^2\sigma_{\delta_i}^2} \tag{3.20}$$

which is dependent on s_i. Each slice along the bunch around a position s_i is compressed differently due to the non uniformly correlated energy spread. With the choice of an off-crest phase ϕ one chooses how a slice around s_i is compressed. A slice around the initial longitudinal position s_i is driven to full compression if $1+AR_{56}+2s_i(BR_{56}+T_{566}A^2) = 0$ is fulfilled. This condition implies that for a given phase ϕ the slice around

$$s_i(\phi) \approx \frac{1 - \frac{2\pi eV}{E\lambda}\sin\phi R_{56}}{2\left(\frac{2\pi^2 eV}{E\lambda^2}\cos\phi R_{56} + \frac{3}{2}R_{56}\left(\frac{2\pi eV}{E\lambda}\sin\phi\right)^2\right)} \tag{3.21}$$

is in full compression using Eq. 3.12 and $T_{566} \approx -3/2R_{56}$ [Stu04].

Slices with less total chirp are not fully compressed while a higher total chirp leads to over-compression. The high energy particles in those slices overtake the leading ones, increasing bunch length again.

Such a nonlinear compression scenario is relatively stable under phase jitter and drifts in the accelerating modules upstream. A slightly varying RF phase changes only the longitudinal slice of the bunch which forms the compressed spike.

3.2 Self-Field Effects

A SASE-FEL driver linac has to provide bunches of such ultra-high charge density that the interaction with their own electromagnetic field (self-field) in an undulator magnet is strong enough to start the SASE process from shot noise. This ability to produce strong self-fields can severely deteriorate the beam quality in the magnetic chicanes used for bunch compression. Although they are normally designed to avoid coupling from incoming energy deviations to transverse phase space (for example, R_{16} and R_{26} and higher order terms will be zero in a chicane made up from rectangular bending magnets only) particle energy changes inside the chicanes due to self-fields like coherent

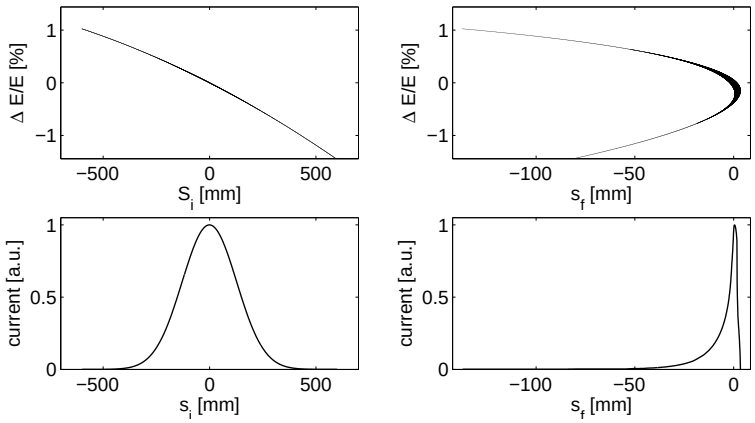

Figure 3.4: Nonlinear contributions like a small, hardly visible quadratic contribution to the energy chirp in the initial particle distribution (left) and T_{566} contributions lead to a nonuniform compression of the bunch (right). In such a situation it is not possible to concentrate most of the particles in a highly charged spike. Most of the particles form a long tail with a low charge density ρ.

synchrotron radiation or space charge fields may cause transverse emittance growth [Der95][ICFA05].

In a rigid bunch in linear motion with the velocity of light, the head particles influence the tail via diffraction and multiple diffraction of their primary field, *e.g.*, via geometrical wakes. The curved motion of charged particles due to magnetic guiding fields causes radiation of electro-magnetic waves, causing the head and tail particles to interact. Tail-head effects are usually much stronger since most of the power is radiated into the forward direction. Space charge forces are not negligible because they interact over a much longer distance compared to the bunch compressor magnets.

3.2.1 Space Charge Effects for Steady State Linear Motion

For a round Gaussian beam with charge q, RMS length σ_z, and RMS radius σ_r, the longitudinal field in free space is [Doh00]:

$$E_z(r=0,z,t) = -\frac{q}{4\pi\epsilon_0}\frac{1}{\gamma\sigma_r\sigma_z}\int_{-\infty}^{\infty} g'(z-s+x)F\left(x\gamma\frac{\sigma_z}{\sigma_r}\right)dx, \tag{3.22}$$

with

$$F(\xi) = \sqrt{\frac{\pi}{2}}\exp\left(\frac{\xi^2}{2}\right)\left[1-\mathrm{erf}\left(\frac{|\xi|}{\sqrt{2}}\right)\right] \approx \frac{1}{\sqrt{1+\xi^2}} \quad \text{for } |\,\xi\,| \gg 1 \tag{3.23}$$

and

$$g'(x) = \frac{-x}{\sqrt{2\pi}}e^{-\frac{x^2}{2}} \tag{3.24}$$

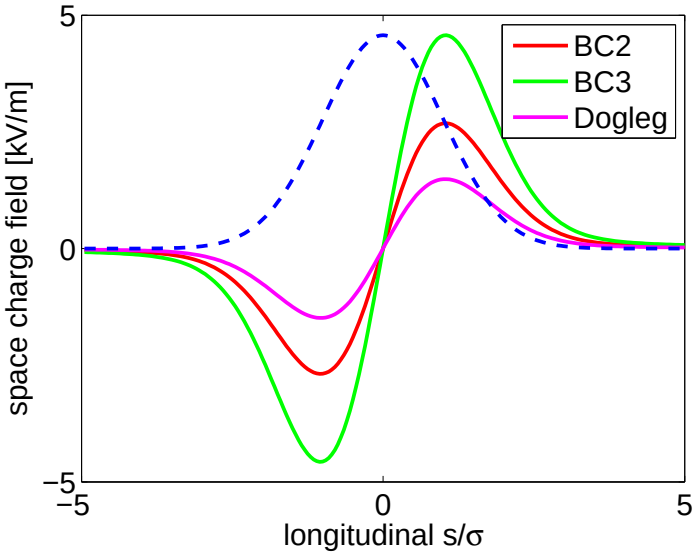

Figure 3.5: Longitudinal space charge forces for different positions along the FLASH linac. The plots include data from after the bunch compressor chicanes (BC2 : $\sigma = 0.4$ mm $E = 127$ MeV and BC3 : $\sigma = 0.1$ mm $E = 380$ MeV) and the dogleg ($\sigma = 0.1$ mm $E = 700$ MeV) for a bunch charge of $q = 1$ nC. The head of the bunch is on the right hand side and its shape is presented as the dashed line.

The head of the bunch experiences an accelerating force from the charge centre of mass while the tail is decelerated. Since space charge forces scale down with increasing energy as $\sim \frac{1}{\gamma^2}$ (see [Jac98] and [Gel06]) the strongest contributions are just downstream of the RF gun and the bunch compressors (Fig. 3.5). Typical values for the space charge forces at FLASH are 5 kV/m at 380 MeV with a bunch length of 0.1 mm.

3.2.2 Transverse Space Charge Forces

The radial transverse space charge fields of a round beam with radius r_0 and uniform transverse particle density are [Wie03]

$$\left.\begin{aligned} E_r(r,z) &= \tfrac{1}{4\pi\varepsilon_0} q\lambda(z) \tfrac{r}{r_0^2} \\ B_\varphi(r,z) &= -\tfrac{c\mu_0}{4\pi} q\lambda(z)\beta \tfrac{r}{r_0^2} \\ &= -E_r(r,z)\tfrac{\beta}{c} \end{aligned}\right\} \text{for } r \le r_0 \tag{3.25}$$

and

$$\left.\begin{aligned} E_r(r,z) &= \tfrac{1}{4\pi\varepsilon_0} q\lambda(z) \tfrac{1}{r} \\ B_\varphi(r,z) &= -\tfrac{c\mu_0}{4\pi} q\lambda(z)\beta \tfrac{1}{r} \\ &= -E_r(r,z)\tfrac{\beta}{c} \end{aligned}\right\} \text{for } r \ge r_0, \tag{3.26}$$

with local longitudinal particle density $\lambda(z)$, and $\varepsilon_0\mu_0 = \frac{1}{c^2}$. The charge density functions $\lambda(z)$ is normalised $\int_{-\infty}^{\lambda}(z)dz = 1$ where q is the bunch charge. For $r \gg r_0$ Eq. 3.26 is also true for arbitrary beam cross sections and transverse particle distributions.

The total radial electromagnetic force is

$$\begin{aligned} E(r,z) &= (E_r + v \times B_\varphi) \cdot \vec{e}_r && (3.27)\\ &= E_r - \beta c E_r \frac{\beta}{c} && (3.28)\\ &= E_r \left(1 - \beta^2\right) \; = \; E_r \frac{1}{\gamma^2}. && (3.29) \end{aligned}$$

The transverse space charge force is therefore given as

$$E(r,z) = \begin{cases} \frac{1}{4\pi\varepsilon_0}\frac{q\lambda(z)}{\gamma^2}\frac{r}{r_0^2} & \text{for } r \le r_0 \\ \frac{1}{4\pi\varepsilon_0}\frac{q\lambda(z)}{\gamma^2}\frac{1}{r} & \text{for } r \ge r_0 \end{cases} . \tag{3.30}$$

Transverse space charge forces are estimated with $r = r_0$, and $\lambda(z) = 1/\sigma_z$ (with the bunch length σ_z) as

$$E(r_0) = \frac{1}{4\pi\varepsilon_0}\frac{q}{\sigma_z\gamma^2}\frac{1}{r_0}. \tag{3.31}$$

For a typical beam size of FLASH $r_0 = 70$ μm and $\sigma_z = 1$ mm we estimate $E(r_0) = 1.68$ kV/m, and $E(r_0) = 67.05$ V/m, at 100 MeV, and 500 MeV beam energy respectively.

3.2.3 Coherent and Incoherent Synchrotron Radiation in Steady State Circular Motion

We assume a thin Gaussian bunch of N electrons with constant longitudinal RMS dimension σ_z on an orbit with radius ρ in stationary circular motion. The total radiated power as a function of the bunch length is sketched in Fig. 3.6. The abscissa of the diagram in Fig. 3.6 is normalised to $\sigma_0 \approx R/\gamma^3$ (which is about a quarter of the critical photon wavelength).

Three regimes can be distinguished (small transition regimes are neglected) [Sch96]. If the longitudinal distance between individual particles is sufficiently large, they radiate independently, or incoherently, so that the power

$$P_0 = N\frac{1}{6\pi}\frac{e^2 c}{\epsilon_0}\frac{\gamma^4}{R^2}, \tag{3.32}$$

is N times the power radiated by one electron. In the other extreme, particles in a longitudinal range smaller than σ_0 radiate fully coherently, independent of the fine structure of the longitudinal distribution. In this regime of fully coherent radiation, the particles radiate as one point charge with a power of:

$$P_f = N^2\frac{1}{6\pi}\frac{e^2 c}{\epsilon_0}\frac{\gamma^4}{R^2}, \tag{3.33}$$

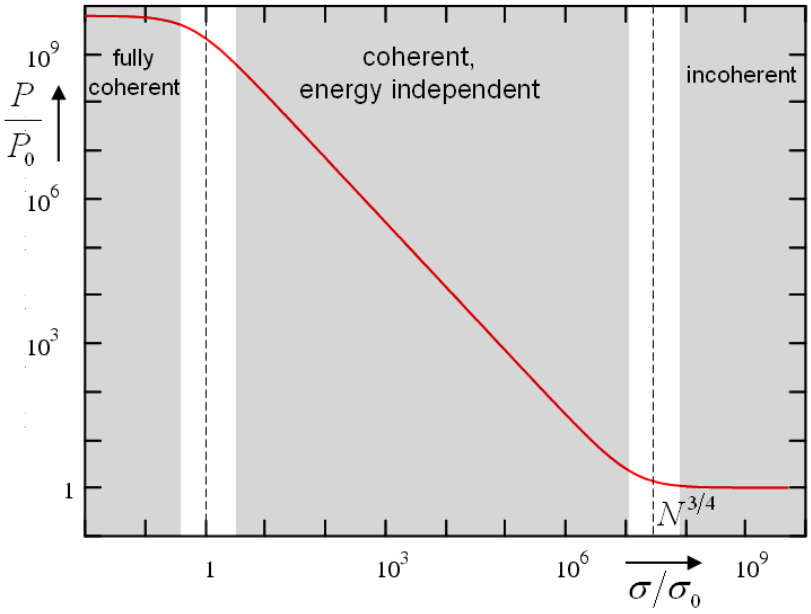

Figure 3.6: Regimes of fully coherent, energy-independent coherent and incoherent radiation [ICFA05].

which is N times the power of the incoherent radiation. Between these two extremes is a regime of coherent radiation with $P \propto N^2$ that does not depend on the energy γ, but on the RMS bunch length σ_z.

The power of the coherent [Sch96], but energy independent radiation is

$$P_{csr} = N^2 x \frac{e^2 c}{\epsilon_0} \frac{1}{R^{2/3}\sigma_z^{4/3}}, \quad \text{with } x = \frac{\Gamma(5/6)}{4\pi^{3/2}} \frac{1}{\sqrt[3]{6}} \approx 0.0279. \tag{3.34}$$

The transition to the incoherent regime is approximately at $\sigma_z = N^{3/4}\sigma_0$. Fig. 3.7 shows the radiated power as function of the energy for a Gaussian bunch with 1 nC charge. Curvature radii between 1 and 20 m and bunch lengths of the order of 10 to 100 μm are typical for the FLASH, XFEL, and LCLS bunch compressors. The choice of the energy for a bunch compression stage is a compromise between radiation and space charge effects which scale with $q/\sigma_z\gamma^2$. This usually leads to a working point in the regime of energy independent coherent radiation.

Assuming steady state conditions in the last magnet of a bunch compressor we can estimate the energy loss due to CSR. For the first chicane BC2 of FLASH, we find a radiated power of 23 kW, corresponding an energy loss of 0.04 mJ ($R = 1.65$ m $q = 1$ nC and $\sigma = 0.4$ mm). In BC3 the radiated power is 67 kW resulting in an energy loss of 0.1 mJ($R = 5.3$ m $q = 1$ nC and $\sigma = 0.1$ mm). If we assume a sharp spike of $\sigma = 5$ μm with a charge $q = 0.1$ nC at the head of the bunch the radiated power in the last

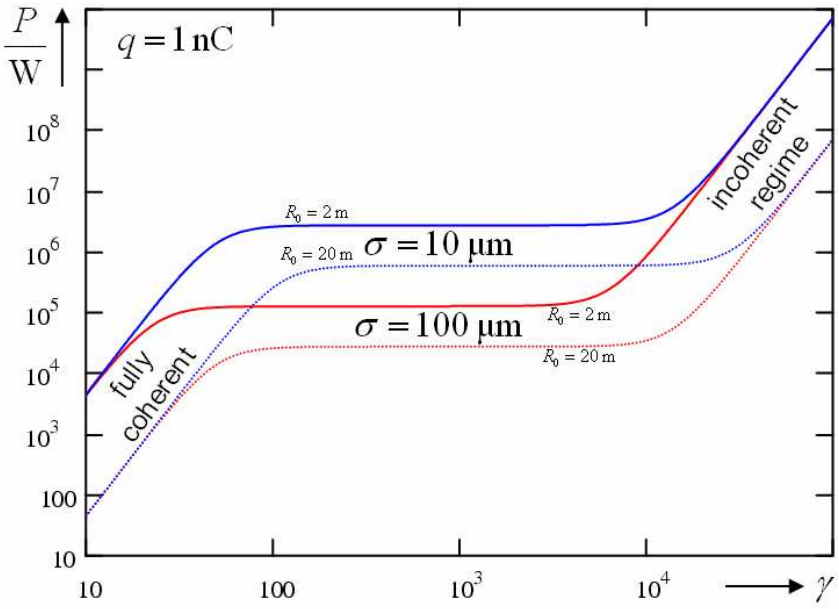

Figure 3.7: Radiated power versus energy of a bunch with the charge of 1 nC [ICFA05].

dipole of BC3 would be 363 kW which corresponds to an energy loss of 0.06 mJ. The particle number N is given by q/e. From the energy loss of a bunch of 0.04 mJ, 0.1 mJ, and 0.06 mJ we estimate an energy loss per particle of 38 keV, 112 keV, and 606 keV, respectively.

The effect of the CSR on the energy distribution inside the bunch is a geometrical effect as illustrated in Fig. 3.8. Since the bunch propagates on a curved trajectory and the emitted radiation travels along a straight line, the path lengths are different. Therefore, the electro-magnetic field emitted at the tail of the bunch, overtakes the leading electrons in a distance Δl with respect to the emitting electron, were l is the longitudinal phase-space coordinate.

For the energy change along the bunch per distance travelled for periodical circular motion one can write [Sal97]

$$\frac{dE(s,\rho)}{cdt} \simeq -\frac{2e^2}{\sqrt[3]{3R^2}} \int_{-\infty}^{s} \frac{ds'}{\sqrt[3]{s-s'}} \frac{d\lambda(s')}{ds'} \tag{3.35}$$

with the bending radius R the bending angle α and the charge density λ, which reduces to

$$\frac{dE(s,\rho)}{cdt} = -\frac{2Ne^2}{\sqrt{2\pi}\sqrt[3]{3R^2\sigma^4}} F(\frac{s}{\sigma},\rho) \tag{3.36}$$

for a Gaussian charge profile with the form factor

$$F(\xi) = \int_{-\infty}^{\xi} \frac{-\xi' e^{-\xi'^2/2}}{\sqrt[3]{\xi - \xi'}} dx'. \tag{3.37}$$

In Fig. 3.8 this steady state rate of energy change along a bending magnet of BC3 at FLASH is plotted for a Gaussian bunch.

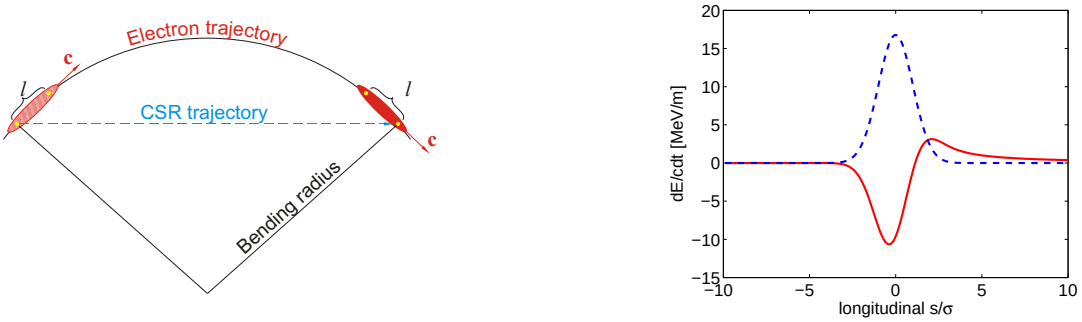

Figure 3.8: (left) Inside a bending magnet the radiation, which is emitted from trailing electrons, can catch up with the leading electrons which are Δl further forward. There the radiation is party absorbed. Figure is taken from [Bol05]. (right) Energy loss per unit length along the bunch due to coherent synchrotron radiation. The longitudinal charge distribution (dashed line) has a Gaussian shape. The energy loss (solid line) was calculated using Eq. 3.37, which represents the steady state regime. A Gaussian bunch of charge $q = Ne = 0.5$ nC and a RMS length of $\sigma = 5$ μm (dashed line) moves in a dipole with a bending radius of $R = 5.3$ m, which approximates the situation in BC3.

3.2.4 Transient CSR Effects

The bending magnets at FLASH are too short to consider only the steady state CSR fields. The transient behaviour of the CSR fields of a one-dimensional bunch of arbitrary charge density was calculated analytically in [Sal97]. When a bunch of electrons enters a bending magnet a longitudinal force starts to build up due to the generation of the longitudinal CSR fields. The force changes the energy of the electrons depending on the position of the bunch inside the magnet and at the longitudinal position s of the electrons inside the bunch.

The energy change per distance travelled inside a bending magnet of finite length can be expressed as [Sal97]

$$\begin{aligned} \frac{dE(s,\rho)}{cdt} &= -\frac{2e^2}{\sqrt[3]{3R^2}} \left(\sqrt[3]{\frac{24}{R\alpha^3}} \left[\lambda\left(s - \frac{R\alpha^3}{24}\right) - \lambda\left(s - \frac{R\alpha^3}{6}\right) \right] + \right. \\ &\quad \left. + \int_{s-R\alpha^3/24}^{s} \frac{ds'}{\sqrt[3]{s-s'}} \frac{d\lambda(s')}{ds'} \right) \end{aligned} \tag{3.38}$$

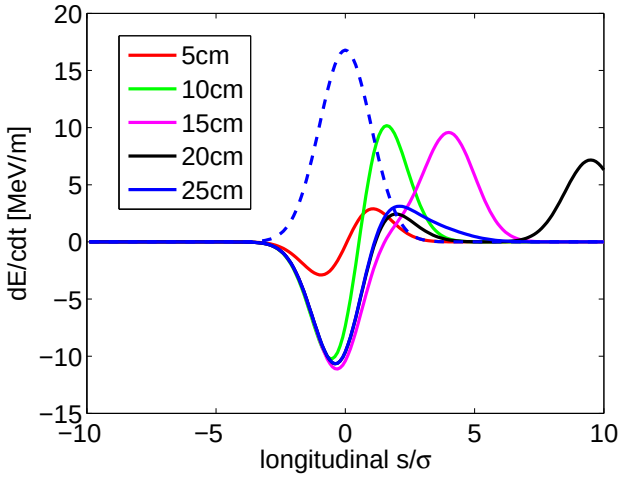

Figure 3.9: The rate of the energy change along the bunch is plotted at various positions along the orbit in a bending magnet. A Gaussian bunch of charge $q = Ne = 0.5$ nC and a RMS length of $\sigma = 5$ μm (dashed line) enters a dipole with a bending radius of $R = 5.3$ m, represent the situation at the end of BC3. The energy change increases to about a distance of 15 cm inside the bending magnet. After 20 cm the entrance transient has moved in front of the bunch and the shape of the energy change converges to the steady state result (compare Fig. 3.8).

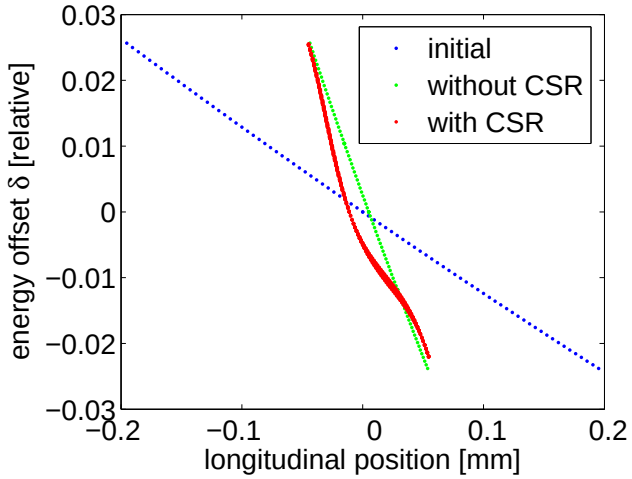

Figure 3.10: An electron bunch with a linear energy chirp (blue) is send through a magnetic chicane with $R = 8.4$ m. The final bunch (red and green) has a reduced bunch length. The centre part of the bunch has a deformed energy profile (red). In addition the total energy spread is decreased.

with the bending radius R, the bending angle α, and the charge density λ. It reduces to

$$\frac{dE(s,\rho)}{cdt} = -\frac{2Ne^2}{4\pi\varepsilon_0\sqrt{2\pi}\sqrt[3]{3R^2\sigma^4}}F_0(\frac{s}{\sigma},\rho) \tag{3.39}$$

for a Gaussian charge profile with the form factor

$$F_0(x,\rho) = \rho^{-1/3}\left(e^{-(x-\rho)^2/2} - e^{-(x-4\rho)^2/2}\right) + \int_{x-\rho}^{x}\frac{-x'e^{-x'^2/2}}{\sqrt[3]{x-x'}}dx' \tag{3.40}$$

and $\rho = \frac{R\alpha^3}{24\sigma}$. $R\alpha$ is the distance travelled inside the bending magnet. In Fig. 3.9 the rate of energy change along a bending magnet of BC3 at FLASH is plotted for a Gaussian bunch.

In Fig. 3.10 an example illustrates the effects of CSR forces on an electron beam. A Gaussian bunch with a linear energy chirp is send through a four-bend bunch compressor chicane. The final compressed bunch develops a nonlinearity in longitudinal phase space caused by CSR effects. The total RMS energy spread is reduced as well as the total beam energy.

3.3 Emittance Growth

Transverse emittance is a measure of the phase space area occupied by the bulk of the particles, projected onto one transverse plane:

$$\varepsilon = \sqrt{\langle x^2\rangle\langle x'^2\rangle - \langle xx'\rangle^2}. \tag{3.41}$$

For a particle distribution which is centred on the longitudinal axis, as for instance in a storage ring, this quantity is a good measure for the beam quality.

In a linac, however, wake fields and CSR fields tend to produce varying transverse offsets along the bunch, and 'banana' shaped bunches with long transverse tails may be the result (see section 3.4.1). To characterise the ability of such a bunch to drive a SASE FEL, the transverse emittance for longitudinal slices along the bunch, the *slice* emittance, is defined. The overall bunch-length integrated emittance is important because it is the measurable quantity for many beam diagnostics systems, and is referred to as the *projected* emittance.

If the beam energy is increased, the slopes $x' = p_x/p_0$, and $y' = p_y/p_0$ decrease proportionally to $1/p_0$, where p_0 is the momentum of the beam. The decrease of the geometric (Eq. 3.41) emittance with increasing beam energy is called *adiabatic damping*. The geometric emittance is multiplied by the factor p_0/m_0c to obtain the *normalised* emittance

$$\varepsilon_N = \frac{p_0}{m_0c}\varepsilon. \tag{3.42}$$

In the absence of nonlinear effects, the normalised emittance stays constant also during acceleration of the particles.

3.3.1 Projected Emittance

A simple model for projected emittance growth assumes that the phase space of the longitudinal beam slices are unperturbed, but their centroids $x_c(s)$, $x'_c(s)$ have shifted. The second moments of the full bunch can then be expressed as superpositions of the second moments of the centroids and those of the unperturbed distribution, described by the Twiss parameters α and β and the initial emittance ε_0.

$$\langle x^2 \rangle = \langle x_c^2 \rangle + \varepsilon_0 \beta, \quad \langle x x' \rangle = \langle x_c x'_c \rangle - \varepsilon_0 \alpha, \quad \langle x'^2 \rangle = \langle x'^2_c \rangle + \varepsilon_0 (1+\alpha^2)/\beta \tag{3.43}$$

A simple estimate is given by the case where (for example) a CSR-induced bunch-length correlated energy spread ΔE_{rms} is generated over the last bending magnet of a chicane. We assume a short magnet with bending angle θ. The energy spread induces mostly an angular spread $\Delta x'_{rms} = |\theta| \Delta E_{rms}/E$ after the bend, producing a final projected emittance of

$$\varepsilon = \sqrt{{\varepsilon_0}^2 + \varepsilon_0 \beta (\theta \Delta E_{rms}/E)^2}, \tag{3.44}$$

which suggests a small (horizontal) β-function in that region of the chicane. A detailed study for realistic cases can be found in [Lim05].

We now estimate the growth of projected emittance due to CSR effects in BC3 of FLASH. The mean energy loss per particle is given by Eq. 3.34 as

$$\Delta E_{mean} = P_{csr} \cdot \frac{L_B}{cN} \approx 0.606 \text{ MeV} \tag{3.45}$$

assuming a sharp spike of $\sigma = 5$ μm and $q = 0.1$ nC in the last dipole of BC3. The RMS energy spread for a Gaussian bunch is approximately

$$\Delta E_{rms} \approx 0.7 \cdot \Delta E_{mean} \approx 0.42 \text{ MeV}. \tag{3.46}$$

The normalised emittance at the chicane entrance is $\gamma \varepsilon_0 = 2.0$ mm mrad and the beta function in the last bend magnet is about $\beta = 6$ m. With the rough estimate from Eq. 3.44 we predict a final projected emittance of $1.14\varepsilon_0$. Tracking calculations using *CSRTrack* (see section 4.2.3) yield an emittance growth of $1.2\varepsilon_0$.

3.3.2 Slice Emittance

The time-sliced emittance can be increased by two effects [Lim05]:

- Inside the compressor chicane the slice will experience the non-linearities of the longitudinal CSR field. When the bunch is deflected in a bend, a longitudinal slice of particles does not stay perpendicular to the momentum; it is yawed with respect to the momentum axis. Assuming no bend-plane focusing, and a convergent incoming beam with a waist inside the chicane, the projected length of a slice with an initial length of zero is

$$\sigma_{proj} = \sqrt{\epsilon_0 \beta_w} \sqrt{\left(\frac{R_{52} - s_w R_{51}}{\beta_w} \right)^2 + R_{51}^2}, \tag{3.47}$$

with β_w the beta-function at the waist, s_w the distance between chicane entry and waist, and R_{51} and R_{52} the transport matrix coefficients from start of chicane to any point within [Lim05]. For a four-dipole chicane, $|(R_{52} - s_w R_{51})/\beta_w|$ is much smaller than unity in the region from the end of the third to the fourth magnets, where strong CSR fields occur, if the horizontal optical waist is positioned there. Further reduction of slice emittance growth can be achieved by minimising β_w.

- The non-linear variation of the longitudinal and transverse CSR fields, as a function of transverse position, contributes to slice emittance growth, even if the projected slice length is small, such as inside and downstream of the last bending magnet.

3.4 Beam Dynamics at FLASH

The dynamics of electron beams including self-field effects are studied by numerical simulations. Such simulations include space charge interactions, wake fields of the modules, and CSR forces. In this section however we do not go into the details of the simulations techniques. Further details on the tracking studies are summarised in chapter 4 and 5.4.

3.4.1 Operation Mode of FLASH

Operation of the SASE FEL driven by the TESLA test facility (TTF) electron linac gave practical experience with the beam dynamics of high peak current beams [Doh04]. TTF was operated in a nonlinear compression mode (Sec. 3.1.5) since the RF system was not able to produce a linear energy chirp. TTF demonstrated SASE operation [And00] which allowed for studies on self-forces and their effect on the FEL process. At TTF the effects of self-forces on the beam were indirectly analysed by comparing the results of start-to-end simulations, including FEL calculations, with the measured performance of the machine.

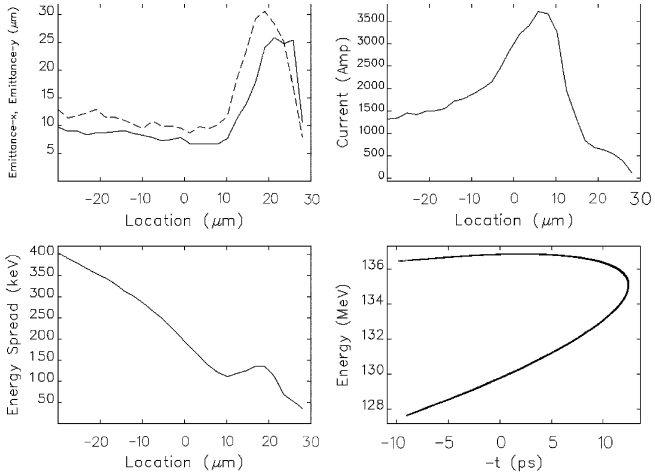

Figure 3.11: An example from TTF. Normalised slice emittance (x - line, y dash), current, RMS slice energy spread in the front part of the bunch, and longitudinal phase space distribution. The position is behind the bunch compressor. CSR is off. The bunch head is on the right. Figures are taken from [Doh04].

An important property of SASE FELs is the fact that not the global, but local parameters along the bunch are important. Therefore, the emittance, energy spread, and charge density of the total bunch are a less important measure of beam quality than the properties of longitudinal slices to analyse the beam quality. Fig. 3.11 and Fig. 3.12 show beam parameters for a TTF beam after bunch compression exclusive and inclusive CSR forces, respectively.

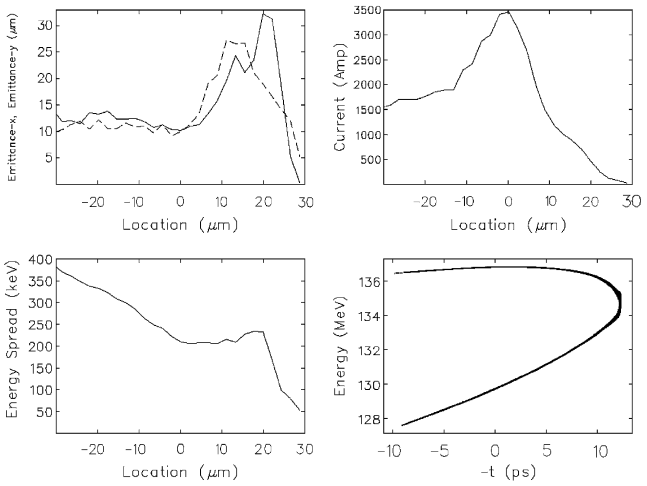

Figure 3.12: An example from TTF. Normalised slice emittance (x - line, y dash), current, RMS slice energy spread in the front part of the bunch, and longitudinal phase space distribution. The position is behind the bunch compressor. CSR is on. Bunch head is on the right. Figures are taken from [Doh04].

Since the 3rd harmonic RF system used for longitudinal linearisation is not yet (2007) installed at FLASH, the machine is still operated in nonlinear compression mode (Sec. 3.1.5) [Sal05].

In fact, self-field effects play a significant role in the bunch compression process for short pulses. At FLASH a two-stage bunch compression system using the chicanes called BC2 and BC3 is used [TTF02][Stu04] in order to reduce self-field effects. The beam is compressed in two steps at energy levels of ≈ 130 MeV and ≈ 380 MeV. Starting with a peak current of $I_{\mathrm{GUN}} \approx 30 - 50$ A in the first compression stage, a peak current of $I_{\mathrm{BC2}} \approx 200 - 400$ A is generated at $E \approx 130$ MeV. Final formation of the high current spike is then done in the second chicane reaching $I_{\mathrm{BC3}} \approx 1000 - 1500$ A at $E \approx 380$ MeV. The combination of RF phases in accelerating modules ACC1, ACC2, and ACC3 defines a slice in the initial distribution of which the spike is finally formed (Fig. 3.13 and Fig. 3.14) [Doh05][Beu06a][Dohlus].

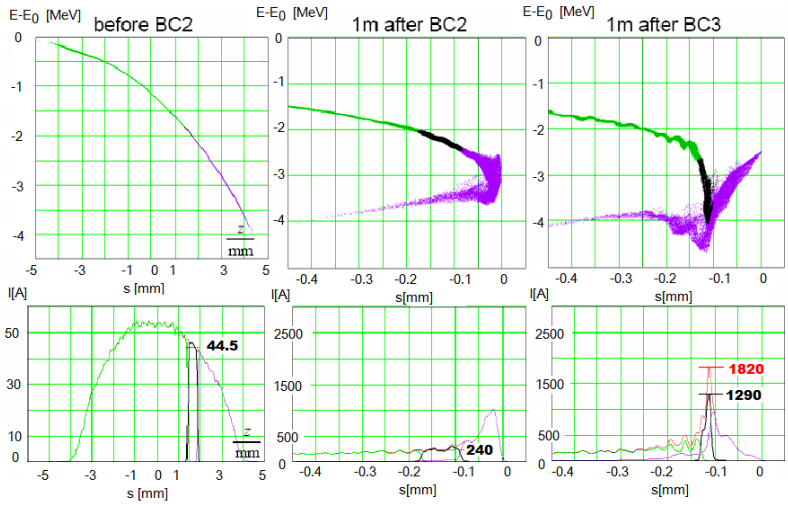

Figure 3.13: Illustration of the two-stage nonlinear bunch compression. Current distribution (bottom) and longitudinal phase space (top) along the electron bunch after acceleration module ACC1 (left), bunch compressor BC2 (middle) and BC3 (right). Coloured areas on the plot illustrate the dynamics of particular sub-sets of the electron bunch. The black part is compressed to the high current spike after BC3. Bunch head is an the right side. ACC1 phase offset is $\phi = 9°$ all other modules are on crest. The red curve gives the total current while the coloured lines represent the current of the respective particles. Figures taken from [Doh05].

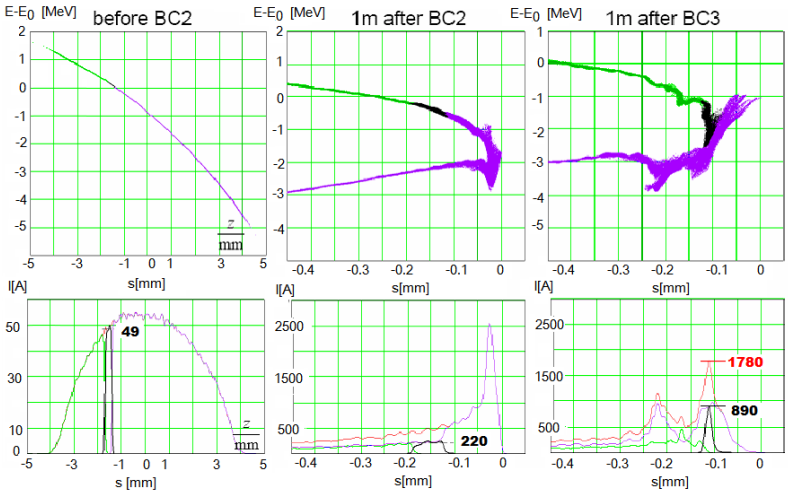

Figure 3.14: As in Fig. 3.13. ACC1 phase offset is $\phi = 14°$ all other modules are on crest. Figure taken from [Doh05].

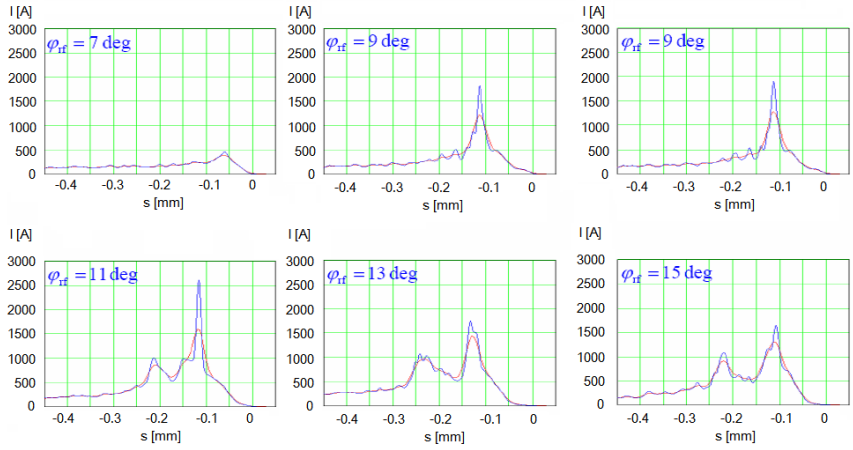

Figure 3.15: For ACC1 phase offsets larger than $\varphi = 10°$ a second current spike is generated by CSR interactions in BC2 and the longitudinal dispersion in BC3. The red curve shows the charge profile after noise reduction. Figure taken from [Doh05].

Self-interactions change the longitudinal phase space (especially during the compression process) by changing the correlated energy spread. In the example with an ACC1 phase offset of $\phi = 14°$ (Fig. 3.14), deceleration by CSR forces reduces the energy of the high charge region of the bunch such that a new negative slope is created. This slope is then compressed in BC3, resulting in a second spike in the charge profile (Fig. 3.15).

The bunch is slightly deformed by self-interactions. The result of CSR effects in BC2 is a relatively small increase of the energy spread at the spike. Particles in front of the spike are accelerated by the longitudinal space charge field (compare Fig. 3.5). These particles have a shorter path length in BC3 which moves them further forward with respect to the whole bunch. The energy spread at the high charge spike is increased more strongly then in BC2 due to the higher peak current.

Coherent synchrotron radiation and space charge effects distort the distribution in the vicinity of the head of the bunch where the peak current is high enough to expect FEL gain saturation. Since this distortion occurs mostly in dispersive sections, the transverse phase space is also perturbed. As a consequence, not all the particles within the head of the bunch have an emittance sufficiently small for lasing.

The black particles in Fig. 3.13 indicate this fraction of the particles located within an emittance smaller than the tolerable one ($\varepsilon = 3$ mm mrad). This part of the bunch achieves a peak current of 1290 A and is only approx. 60 fs (FWHM) long. According to FEL simulations, such a beam would generate a radiation pulse of about 30 fs (FWHM) length, which is in good agreement with the pulse lengths measured at FLASH. As shown in Fig. 3.16 the start-to-end simulations are also in qualitative agreement with pictures of the projection of the bunch onto the longitudinal-horizontal plane, which are taken with the help of a transverse deflecting cavity (see chapter 5.2.2).

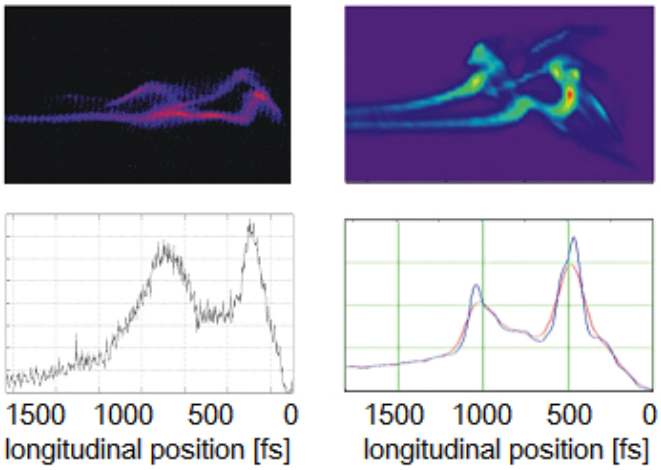

Figure 3.16: Transverse beam profiles after the second bunch compressor BC3 are shown here. On the left hand side experimental data obtained with the transverse deflecting cavity are shown. These data are compared with the results of start-to-end simulations on the right hand side with parameters consistent with the settings for the measurement. The current profiles are shown on the bottom. CSR effects and space charge fields lead to a splitting of the bunch head into two distinct spikes as well as to a transverse distortion. Figure taken from [Doh05].

The two images in Fig. 3.16 show a situation where the bunch is fully compressed in BC3. This behaviour is predicted by start-to-end simulations when CSR and space charge are included up to energies of 500 MeV.

3.4.2 CSR Induced Centroid Shifts

CSR and space charge interactions, in addition to the effect on the compression process, as described in the last section, dilute the transverse emittance. This emittance growth is important to study.

However, as shown in Sec. 3.4.1, the beam structure in the nominal FLASH operation leads to an entangled behaviour of CSR and space charge interactions which makes this operation mode not optimal for dedicated studies of CSR effects.

During nominal operation the initial longitudinal energy chirp is chosen such that the maximal peak current is reached at the end of the last dipole of a bunch compressor chicane. To prepare experiments on CSR effects at FLASH, we study a different operation mode of the bunch compression system.

The compression scenario of choice employs an energy chirp big enough to achieve the maximum peak current in the second dipole of the four-bend chicane BC2. In a symmetric case, the bunch length after the fourth magnet is the same as before the chicane, but the head and the tail of the bunch are interchanged. In the bunch compressor, a transverse displacement and an angular offset is induced to the parts of the beam with altered longitudinal momentum, because of the non-zero dispersion (see Fig. 3.18). Fig. 3.17 shows an over-compressed bunch. After the over-compression the sign of the slope of the energy chirp is changed. CSR interactions inside the chicane change the beam profile in the longitudinal-horizontal plane.

From the experimental point of view another advantage of such a set up is the low peak current after the chicane. This minimises self-interactions further downstream thereby facilitating a clear experimental study on CSR effects.

In the following analysis we will focus on these deformations of the bunch. We divide the bunch into M longitudinal slices each with N_i with $i \in (1, M)$ macro-particles while $\sum N_i$ =total particle number. The *centroid* (x_i, s_i) of slice i is defined by

$$x_i = \frac{1}{\sum_{j=1}^{N_i} q_{j,i}} \sum_{j=1}^{N_i} x_{j,i} q_{j,i} \tag{3.48}$$

$$s_i = \frac{1}{\sum_{j=1}^{N_i} q_{j,i}} \sum_{j=1}^{N_i} s_{j,i} q_{j,i} \tag{3.49}$$

while $x_{j,i}$ and $s_{j,i}$ are the horizontal and longitudinal positions of the jth particle in slice i and $q_{j,i}$ the charge of these particle. The set of the pairs (x_i, s_i) for all slices is called the *centroid curve*. We will now analyse CSR induced deformations of the centroid curve and how they develop along the accelerator.

The electron bunch enters the chicane with a low peak current around $I \approx 50$ A. As the bunch moves along the chicane with increasing longitudinal dispersion R_{56} the peak current increases up to about $I \approx 1$ kA in the second dipole (Fig. 3.19 and Fig. 3.22). At this point the maximal peak current is reached. Further downstream, the bunch is over-compressed, interchanging the head and tail of the bunch. Toward the end of the chicane the bunch length increases while the longitudinal dispersion drops again to zero in the fourth dipole magnet (Fig. 3.22).

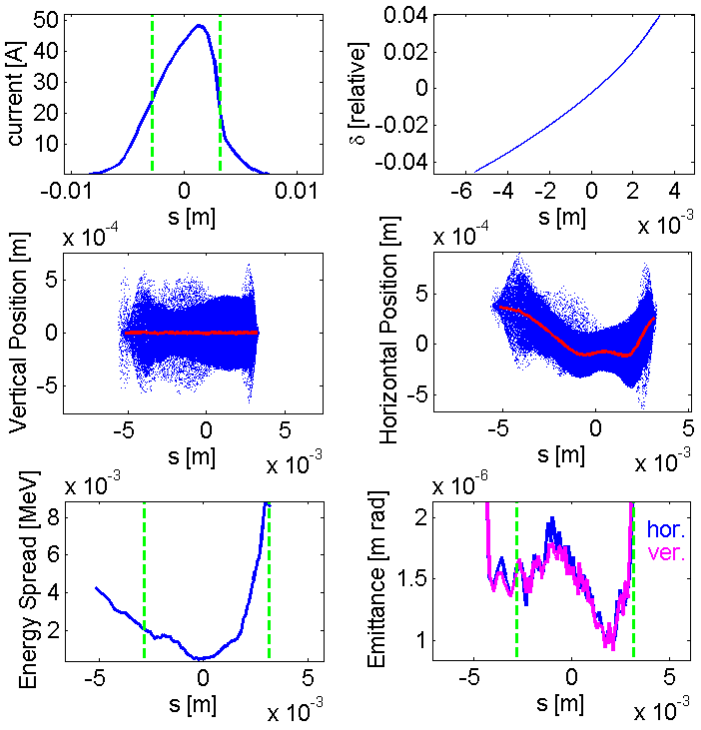

Figure 3.17: Phase space distribution after over-compression. The current profile and the longitudinal phase space are the top figures. In the middle line the side and top view are presented. A horizontal deformation of the bunch is prominent while no vertical effect is visible. The slice energy spread and slice emittance (bottom) are plotted together with FWHM lines from the current profile (green).

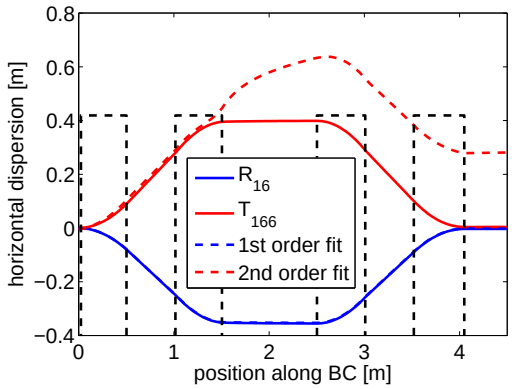

Figure 3.18: The matrix elements for horizontal dispersion in first (R_{16}) and second order (T_{166}) are shown (as defined in Eq. 3.50) as well as the results of a 2nd order polynomial fit to the x-δ plane of the electron bunch. The black boxes represent the bending magnets.

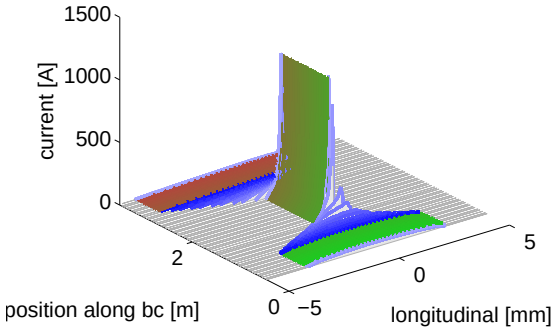

Figure 3.19: The longitudinal current profile of the bunch is shown. The colour of the lines change in the drift spaces from upstream(green) to downstream(red) while the dipoles are represented by blue lines.

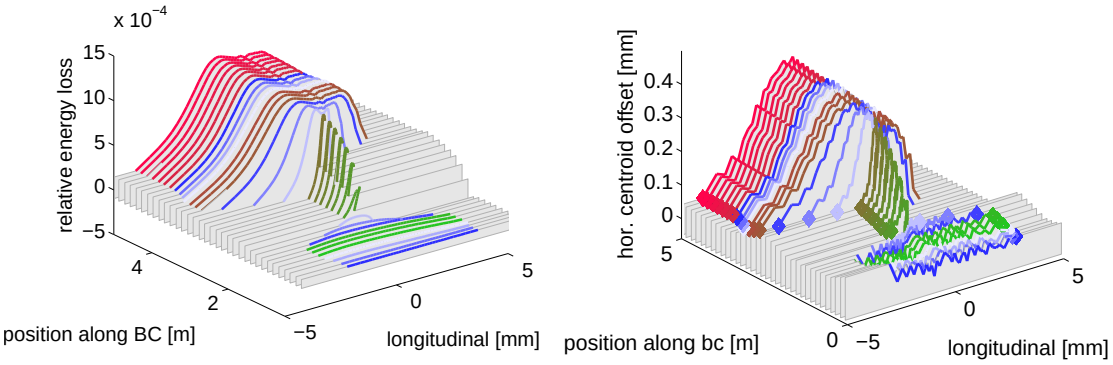

Figure 3.20: (left) The normalised beam energy loss $-\delta = -\Delta E/E_0$ with respect to the initial energy of a set of representative particles along the centroid of the beam are shown along the chicane as a function of their longitudinal position. Colours as in Fig. 3.19. (right) The horizontal dispersion $D_x = \Delta x/\Delta E$ up to second order is subtracted from the horizontal centroid positions to reveal their evolution along the chicane. A diamond denotes the head particle which move to the tail of the bunch during over-compression. The sign of the horizontal centroid shift has been reversed for better visibility.

At the end of the second dipole where the peak current is maximal, strong CSR effects change the energy profile along the bunch (Fig. 3.20). Because of dispersion, these changes in the beam energy profile result in horizontal position offsets with respect to electrons of nominal energy.

Inside the chicane, the RMS width of the centroid curve is dominated by the horizontal dispersion, which is on the order of $\sigma_{x,\mathrm{disp}} = 6$ mm, compared to the horizontal shifts induced by CSR, which are in the order of $\sigma_{x,\mathrm{CSR}} \approx 0.1$ mm. To study further the evolution of these CSR induced centroid displacements we subtract the effect of the horizontal dispersion. The first and second order horizontal dispersion R_{16}, R_{26}, T_{166} and T_{266} results in a horizontal displacement and angle of

$$x = x_0 + R_{16} \cdot \delta + T_{166} \cdot \delta^2 \tag{3.50}$$

$$x' = x'_0 + R_{26} \cdot \delta + T_{266} \cdot \delta^2. \tag{3.51}$$

The dispersion calculated using *elegant* (see Sec. 4.2.3 for more information about tracking codes) and the first and second order correlation between the horizontal displacement and the energy offset, of particles in the tracking calculations, are compared in Fig. 3.18. One observes an agreement in the first order but not in the second order dispersion. In the region with the strongest CSR contributions (the second dipole) an additional contribution is added to the x-δ correlation.

As a result of CSR interactions the energy is reduced in the central region of the bunch where most of the charge is concentrated. These particles in the centre of the bunch

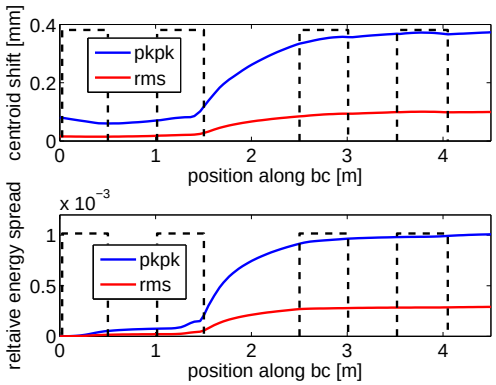

Figure 3.21: The total distance between the shifted and the unshifted particles and the relative energy spread with respect to their initial value along the dispersive beam line are shown as peak to peak and RMS values. The position of the dipole magnets are shown as dashed lines.

therefore yield the strongest position offset (Fig. 3.20). The total distance between the shifted and the unshifted particles increases along the dispersive section as shown in Fig. 3.21. The steepest increase takes place just at the end of the second dipole and the drift space toward the third magnet.

The shift of the centroid positions for different longitudinal slices increase the projected horizontal emittance of the total beam. By subtracting the first and second order dispersion contribution from the horizontal angle of the electron orbits we calculate the projected emittance (Fig. 3.23). As expected from the data on the horizontal centroid shifts we observe that the emittance increases between the second and third dipole.

These transverse displacements are observable with a transverse deflecting RF-structure which takes "top view" pictures of the bunch. We observed CSR induced centroid shifts at FLASH in April 2006 [Beu06b]. More details on these measurements are described in chapter 5.

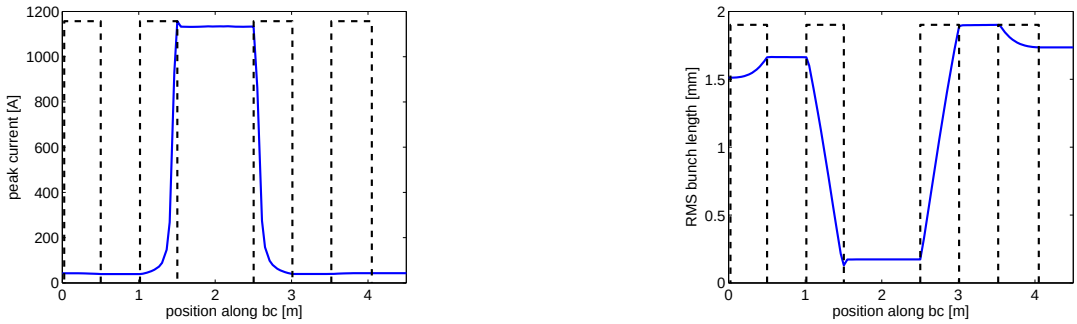

Figure 3.22: (left) The peak current along the bunch compressor reaches its maximum just at the end of the second dipole in BC2. (right) The bunch length along the bunch compressor has its minimum were the peak current reaches its maximum.

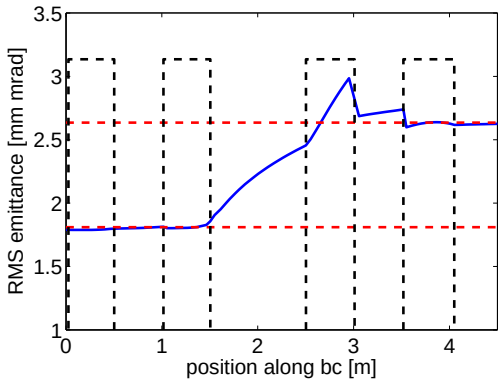

Figure 3.23: The total projected emittance is plotted as a blue line together with the dipoles (dotted black lines). Since only first and second order contributions of the dispersion are subtracted some distortions remain inside the bend sections of the electron orbit. Therefore one has to compare the initial and final value of the emittance were the dispersion is zero. Initial and final values of the emittance of the whole chicane section are presented as red dotted lines.

3.4.3 Bunch Charge Dependence of CSR Effects

FLASH can reasonably be operated with bunch charges up to 2 nC and experimental studies on the CSR induced centroid shifts are possible. To study the charge dependence of CSR effects, especially the CSR induced centroid shifts, properties of the electron bunch and their charge dependence are investigated.

Since the CSR fields are proportional to the bunch charge (compare Eq. 3.39), one would expect a linearly monotonic increase of the CSR induced centroids shifts with the total bunch charge. This would be true in a situation where, excepting the charge, all the properties of the beam remain unchanged. However, due to self-forces, especially space charge forces in the low energy part of the machine, the beam parameters change with bunch charge.

If a portion of the total bunch charge is concentrated in a very small region of the bunch, one would expect the dominant contribution to the CSR field to be there. We therefore conclude that not the total bunch charge, but the peak current determines the strength of CSR self-fields. The magnitude of this peak current, is determined by various beam parameters like the total bunch length, uncorrelated, and correlated energy spread.

First of all, the total bunch length increases due to space charge effects in the injector, thereby reducing the charge density along the bunch (compare 5.3.1). We now compare the mean current as a function of charge for a fixed bunch length with the current obtained from a measured bunch length (see Fig. 3.24). The increase of current is still linear but with a smaller slope.

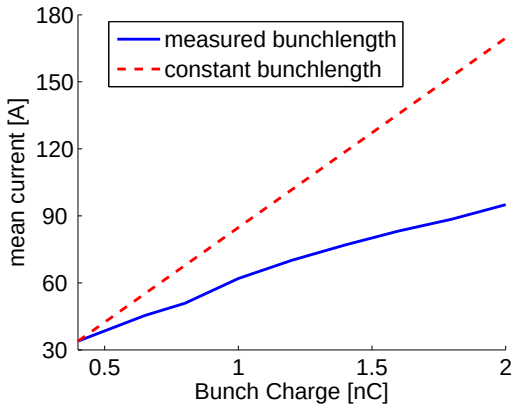

Figure 3.24: Total charge density of a bunch (bunch charge/measured FWHM bunch length) is plotted as the blue line. The dashed red line represents the charge density if the bunch length is independent of charge.

Space charge forces in the injector not only increase the bunch length but the uncorrelated energy spread as well. The uncorrelated energy spread around the charge centre of the bunch is increasing with bunch charge (Fig. 3.25). The width of the compressed

spike is determined by this property (Eq. 3.18). High bunch charges and thus higher energy spread lead to a wider current spike. Therefore, the charge density does not necessarily increase with bunch charge.

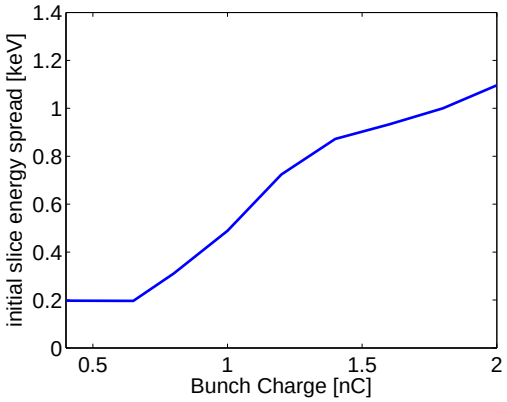

Figure 3.25: The initial RMS slice energy spread around the bunch charge centre is increasing for higher bunch charges. This increase is dominated by space charge effects in the RF gun up to the first accelerating module.

Considering the space charge effects on bunch length and uncorrelated energy spread, one can predict the behaviour of peak current with charge, using the *ASTRA* tracking code (see Sec. 4.2.3). The peak current is not increasing linearly with charge. The increase with bunch charge saturates beyond 1 nC, due to the increasing uncorrelated energy spread. For even higher total bunch charges beyond 1.6 nC, the peak current is even decreasing with bunch charge. Fig. 3.26 shows how the peak current develops along the chicane for different bunch charges. The maximum peak current reached for each charge increases up to about 1.4 nC and drops down for charges higher than 1.6 nC.

From the charge dependence of the bunch length and the uncorrelated energy spread, we would expect that the CSR effects increase with total bunch charge for low charges only. The peak current increases with bunch charges only up to approximately 1 nC. For higher charges, the peak current remains nearly constant, while towards a charge of 2 nC, a decrease of the peak current is observable. The CSR induced centroid shifts therefore increase with charge only in the range below 1 nC and drop again for high bunch charges around 2 nC (Fig. 3.27).

Despite the fact that this analysis was done for the over-compression mode, these results have some relevance for SASE-operation modes. In this over-compression scheme, we observe the maximum possible peak current within the chicane. Space charge effects in the injector prevent the unlimited increase of peak current with bunch charge. This statement is true for all compression systems relying upon longitudinal dispersion, due to the dependence of minimum bunch length on the uncorrelated energy spread (compare Eq. 3.18). This holds even if two-stage compression systems are used, although a better

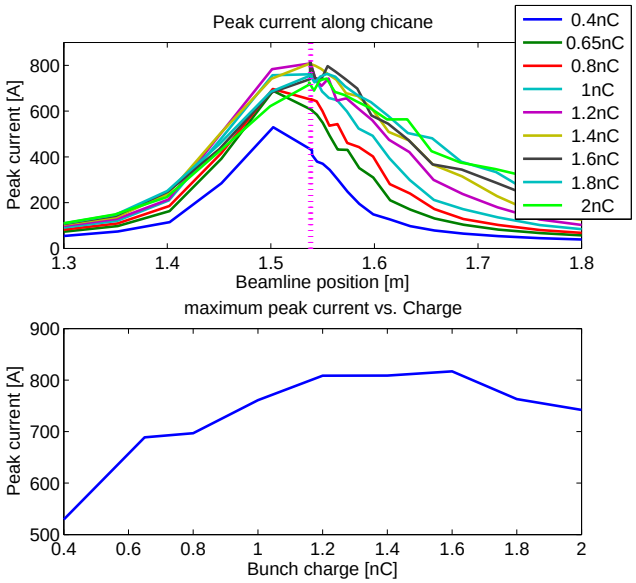

Figure 3.26: (top) The peak current of the bunch along the second and third dipole of the bunch compressor chicanes is plotted here for different bunch charges. The drift space between the two dipoles is omitted and denoted by the vertical dashed line. (bottom) The maximum peak current in the chicane is plotted as a function of bunch charge.

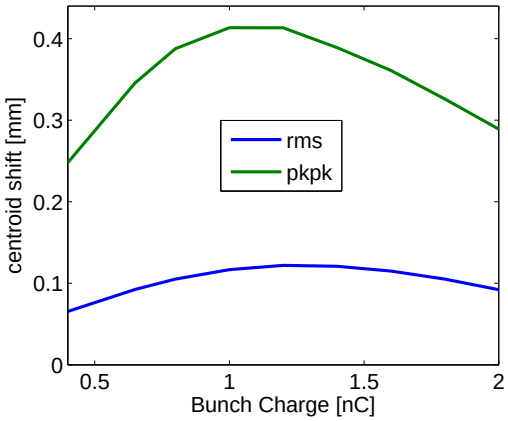

Figure 3.27: CSR induced centroid shifts as a function of bunch charge. *CSRTrack* simulation results after BC2. ACC1 phase offset is $\varphi = 24.9°$ and the bunch compressor is set up for a bending angle of $\alpha = 18.2°$ which leads to a longitudinal dispersion of $R_{56} = 18.5$ cm.

optimisation is possible. SASE operation modes employing higher bunch charges, in an attempt to compensate for increased emittance growth with even higher peak current, are, therefore, not likely at FELs with a FLASH-like compression scheme.

4 Numerical Simulations

4.1 Overview

Numerical particle tracking is an important tool for the study of beam dynamics in a particle accelerator. Tracking calculations supplement the limited diagnostics in an accelerator and provide the opportunity to optimise the design of future accelerators.

Standard beam optics codes like *MAD* [MAD] are used to calculate and optimise the linear beam optics of a particle beam. Self-fields like space charge or CSR interactions are not considered in these programs. Other codes are thereby required to handle these self-interactions. Self-interactions depend strongly on the bunch shape in phase space as it undergoes a dynamic evolution in time. For arbitrary bunch shapes such calculations are hard to handle analytically.

Numerical tracking codes are used to follow the evolution in time of each particle in a bunch. Either a semi-analytic model [Bro82] is used (that represents the beam line as a series of transfer matrices) or tracking with actual force calculations is done. In each of the finite time steps of these tracking calculations the momentum of the particle is used to extrapolate the future position. Forces are applied at each time step to modify the momentum of the particles. These forces are obtained by averaging the force over time steps using numerical integrators like Runge-Kutta or leapfrog algorithms [Knu97]. At each time step the state of the particles in the bunch is used to determine the self-forces.

The number of particles in a typical bunch is on the order of 10^{10}. Such particle numbers require an enormous computational power. The approach to treat this problem is to merge a group of particles into so-called macro-particles. Macro-particles have accordingly higher charges for field calculations but for calculation of dynamics they are considered regularly charged particles like, for instance, electrons.

The macro-particle number however cannot be chosen to be arbitrarily small since the charge distribution of the macro-particles has to represent the detailed sub-structure of the bunch, for instance the micro bunching in the undulator.

Another problem with low macro-particle numbers is numerical noise. Tracking algorithms do not distinguish between real charge density modulations on a bunch or artificial noise related to low particle numbers. Since charge density modulations can lead to beam instabilities, as in the SASE process, macro-particle numbers cannot be arbitrarily small. Noise reduction methods are used but the challenge here is to ensure that no information about the real bunch sub-structure is lost. Typical numbers of macro-particles in a simulation calculation are 10.000 to one million.

A complete treatment of self-interactions would require to take into account that every particle interacts with every other particle, leading to a quadratic dependence of the numerical effort on the macro-particle number. In most cases, the numerical effort

can be reduced by the usage of approximations and semi analytic models in the self-field calculation, such as using a charge density function for the field calculations.

4.2 Simulation Methods

4.2.1 Field Calculation Approximations

For CSR or space charge forces analytic formulae are available for specific bunch shapes like a 1D Gaussian charge distribution (compare Sec. 3.2). The actual bunch shape is represented as a convolution of different smaller Gaussian shaped bunches, so called sub-bunches. The total charge distribution of a bunch approximated by Gaussian sub-bunches is

$$q_\sigma(s) = \int_{-\infty}^{\infty} dx \tilde{q}(x) \frac{1}{\sqrt{2\pi}\sigma} e^{-\frac{(s-x)^2}{2\sigma^2}} \tag{4.1}$$

with $\tilde{q}(x)$ being the one-dimensional charge profile of the bunch and $q_\sigma(s)$ the charge profile represented by sub-bunches of width σ. If σ approaches zero $\int_{-\infty}^{\infty} dx \frac{1}{\sqrt{2\pi}\sigma} e^{-\frac{(s-x)^2}{2\sigma^2}}$ converges to $\int_{-\infty}^{\infty} dx \delta(s-x)$ and therefore $q_\sigma(s)$ to $\tilde{q}(x)$. $\tilde{q}(x)$ might be a step function obtained by binning of the macro-particle distribution which reduces the convolution to a sum. In this case the usage of Gaussian sub-bunches leads to a smoothing of the charge profile.

The total field $\vec{F}(s)$ can then be expressed as the convolution of the field of the sub-bunch $\vec{F}_\sigma(s)$

$$\vec{F}(s) = \int_{-\infty}^{\infty} dx \tilde{q}(x) \vec{F}_\sigma(s-x). \tag{4.2}$$

In a more general approach the field of a sub-bunch is not only a function of the dimension of the sub-bunch but of averaged beam parameters in the corresponding bin like the slice emittance or energy.

Similar techniques can be used for 3D charge distributions. In such a case a representation of the self-field $\vec{F}(\vec{x})$ as a function of a 3D sub-bunch is convoluted with a 3D charge density function.

Another approach is a representation of a 3D bunch by building blocks such as cubes. The number of macro-particles in each of these blocks is counted and this determines the charge. One assumes that the block is homogeneously charged to calculate the generated fields. *ASTRA* for instance uses a set of concentric cylindrical rings for the calculation of space charge forces. The fields of each building block are summed up to obtain the total space charge field.

4.2.2 Current Smoothing

In the standard approach, the longitudinal charge density is represented as a convolution of the corresponding longitudinal particle coordinates μ_i with a normalised Gaussian of a certain width σ

$$G(x,\sigma) = \frac{1}{\sqrt{2\pi}\sigma} e^{-\frac{(x-\mu_i)^2}{2\sigma^2}}. \tag{4.3}$$

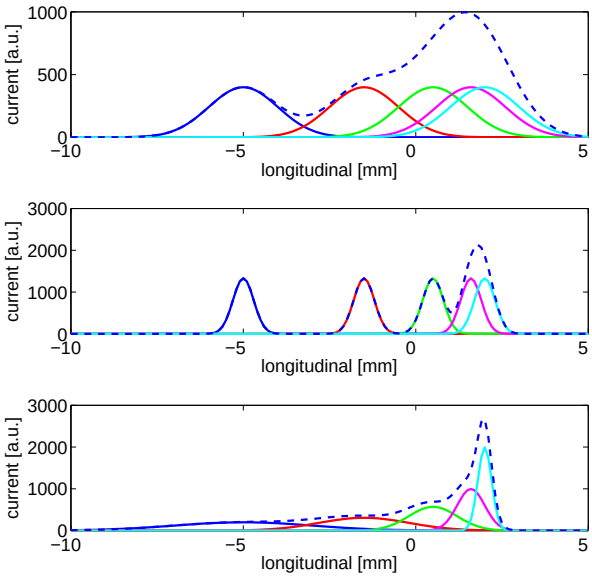

Figure 4.1: Five "particles" are represented by normalised Gaussians (straight lines) to obtain a smooth current profile (dotted line). The total integral over the whole length is constant (total bunch charge). (top) A constant and long smoothing width σ yield a relatively smooth distribution with a low peak current. (middle) A constant but small smoothing width σ gives a good representation of the high charged spike but a spiky tail. (bottom) Choosing a different width for each particle one obtains a smooth distribution and a sharp spike.

As described earlier, the artificial noise from the quasi-random particle distribution is smeared out only if σ is chosen big enough. In this case, however, the charge density may be underestimated especially if the electron bunch has a narrow, high-charge spike which is smaller than the chosen σ. The situation is even more complicated in the case of a macro-particle distribution with a big variance in the charge density. This is the case for the FLASH bunches in the nonlinear compression scheme with a high-charge leading spike and a long low charge tail.

Our approach to this problem relies on an adaptive variation of σ along the bunch [Dohlus], depending on the local macro-particle density. A small σ should be chosen to respect the steep slopes and the high peak current of a narrow spike, and a high value for σ would smooth out the long tail with a low particle density (Fig. 4.1). The particle distribution is separated into N slices along the longitudinal axis while the particle number in each slice is constant. The width of a slice determines the local σ of the smoothing algorithm.

This adaptive Gaussian smoothing is effective but not sufficient to reduce the noise for relatively low particle numbers. Another method called position averaging is applied to reduce the noise even further. The longitudinal particle positions are altered before the Gaussian smoothing is applied. One replaces the longitudinal position μ_i of particle i by

$$\hat{\mu}_i = \frac{1}{q_{\text{total}}} \sum_{j=i-M}^{i+M} \mu_j q_j, \tag{4.4}$$

with the charge of each particle q_i, the total charge $q_{\text{total}} = \sum_i q_i$, and a fixed integer M. This position averaging algorithm can be optimised by tuning M and the number of iterations of the whole averaging process.

4.2.3 Simulation Codes

The following numerical tracking codes are used in this thesis for simulations of FLASH:

elegant

elegant by M. Borland is based on beam transport theory using matrices for linear and non-linear interactions [Bor00]. Models for non-linear self-interactions like space charge wake fields and CSR forces are included as well. These models, however, require large particle numbers for proper noise reduction even for simplified field calculations [Bow04]. *elegant* is used for beam transport calculations were relatively low self-interactions are expected as in the sections downstream of the injector or the first bunch compressor.

ASTRA

ASTRA - A space charge tracking algorithm - developed by K. Flöttmann et al. [ASTRA] was originally designed for space charge tracking calculations during the photo emission processes in RF-guns. *ASTRA* uses both a 3D or a 2D space charge field calculation algorithm. In the 2D case a cylindrical grid is set around the bunch. The charge in each of these cylinder ring cells is used to calculate the fields of each cell in their centre-of-mass frame. This method is quite efficient but is restricted to nearly rotationally symmetric bunches. The 3D field calculation uses box shape cells of an fully Cartesian grid. Large particle numbers are required for noise reduction since the number of cells is much higher than in the 2D cylindrical case. The results of different space charge tracking codes are compared in [Lim03].

The original *ASTRA* code is furthermore restricted to straight beam trajectories due to the absence of dipole fields. As part of this thesis dipole fields and therefore more general beam trajectories are included into the *ASTRA* code as well as a 1D CSR field treatment (see Sec. 4.3). Another recent development of *ASTRA* is a version for parallel CPU computer systems by L. Fröhlich [pASTRA].

CSRTrack

M. Dohlus' code *CSRTrack* focuses on the treatment of CSR fields [Doh00b][Doh04b] [CSRTrack]. *CSRTrack* uses various models for field calculations. A fast and efficient 1D method uses the line charge profile, obtained by a projection of each particle on the trajectory, for CSR wake calculations according to analytical formulae [Sal97][Doh03]. Transverse properties of these fields and effects of the transverse beam shape are neglected.

A more general approach relies on full field calculations on a 3D spatial grid either by direct field calculations or Greens function methods [Doh00b][Doh04b]. Of course, space charge forces are included in these full fields. However more numerical effort is needed for this 3D method than for the space charge algorithms in *ASTRA*. The results of these different methods are compared for instance by F. Stulle [Stu04].

CSRTrack is available as a single CPU version and for parallel computing.

4.3 Modifications to ASTRA

During the work on this thesis, the *ASTRA* code has been modified to treat dipole fields and 1D CSR calculations.

4.3.1 Dipoles

ASTRA internally calculates the electromagnetic field at any required point in space. While fields of quadrupoles and solenoids are constant in time, the fields of accelerating RF-cavities or self-fields are time dependent. All the contributions are summed up to obtain the total force at a given macro-particle position.

Dipole fields in *ASTRA* are introduced by two lines in the bending plane representing the boundaries of the bending magnet field. Each dipole is represented by three regions (see Fig. 4.2). In the region around the magnet edge, the magnetic field perpendicular to the bending plane is of the form

$$B_{\perp}(d) = \left(\frac{B_0}{1 + e^{-8d/D}} \right) \tag{4.5}$$

where d is the distance to the magnet boundary in the bending plane, D the characteristic width of the fringe area, and B_0 the maximum field of the dipole. With $\mathrm{rot}\vec{B} = 0$ the perpendicular field component is given by

$$B_{\parallel}(d,h) = B_0 \frac{8\frac{h}{D}}{\left(1 + e^{-8d/D}\right)^2} e^{-8d/D} \tag{4.6}$$

with h being the height above the bending plane. This transition of the field is considered for d between $-2 \cdot D$ and $2 \cdot D$. Inside the magnet, $d > 2 \cdot D$, the field is assumed to be of the constant value B_0. For $d < 2 \cdot D$ the field is set to zero (Fig. 4.3).

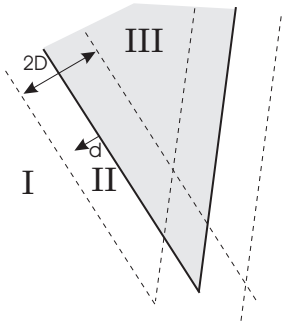

Figure 4.2: The physical edges of the dipoles are represented by two lines (solid). The space around the dipole is separated into three regions. Outside the dipole (I), inside the dipole (III), and in the transition region (II). Fields inside (III) are at the nominal value B_0 and are zero outside (I). In the transition region (II) the field depends on the normal distance to the edge of the dipole d. The transition region is bounded by two parallel lines (dashed), each at a distance D.

Magnetic fields in the region where the transition regions of both magnet edges overlap are treated as

$$B_{\perp}(d_1, d_2) = B_0 \left(\frac{1}{1 + e^{-8d_1/D_1}} \right) \cdot \left(\frac{1}{1 + e^{-8d_2/D_2}} \right), \tag{4.7}$$

with d_1, D_1, and d_2, D_2 being the dimensions with respect to the first and second field boundary respectively. The perpendicular field components of each field boundaries are added.

4.3.2 Comparison with elegant

A comparison of tracking calculations with dipole fields in *ASTRA* and *elegant* was done for rectangular and sector magnets [Gerth].

The particle *generator* of *ASTRA* (see [ASTRA]) was used to generate a particle distribution with a beam energy of 10.5 MeV, a RMS bunch length of 1.2 mm, RMS transverse beam size of 2 mm, and a normalised transverse emittance of 3 mm mrad. The distributions for all parameters were chosen to be *uniform*.

Sector Magnet

The first test case comprises a drift, a sector magnet and a drift. The beam directions at the entrance and exit of the magnet are perpendicular to the pole ends, i.e., the pole face rotations are $\beta_1 = \beta_2 = 0$. The magnet parameters were chosen to be $L = 0.2$ m and $\alpha = 30°$, giving a bend radius of $R = 0.381972$ m. These values, together with the drift space $z_D = 0.1$ m to the dipole entrance plane, determine the input parameters for *ASTRA*.

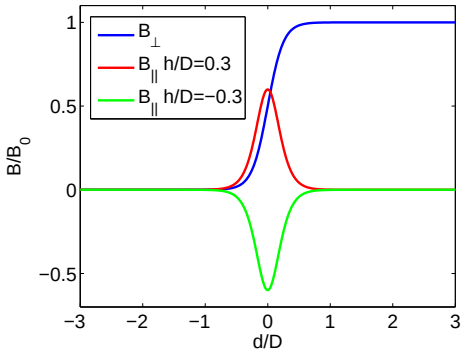

Figure 4.3: The fringe fields in *ASTRA* are shown as in Eq. 4.5 and Eq. 4.6 normalised to B_0 (compare Fig. 4.2).

Results of the tracking (without space charge and CSR effects) are shown in Fig. 4.4. *ASTRA* results are shown in red and the results obtained with the code *elegant* are shown in blue. In addition, a particle distribution was generated that was composed of particles with all combinations of the nominal, minimum and maximum values in 6D phase space. This distribution was transported (in *MATLAB*) by applying first order transport matrices [MAD]. These results are shown as colour-coded triangles and diamonds to visualise the effect of the energy spread on the transport. As seen from Fig. 4.4, the results of all 3 methods agree well.

Rectangular Magnet

Tests similar to those performed with the sector magnet have been carried out for a rectangular magnet. In this case, the beam enters and exits the dipole magnet with half the bend angle, corresponding to pole face rotations of $\beta_1 = \beta_2 = \alpha/2$. From the magnet parameters $L = 0.2$ m, $\alpha = 30°$, and a drift space $z_D = 0.12$ m. The end of the tracking was set to $z_{stop} = 0.5$ m. The particle distributions used for the sector magnet were used here, as well.

In Fig. 4.5 the corresponding tracking results are shown. In contrast to the sector magnet, which is defocussing in the horizontal direction, the rectangular magnet focuses the beam in the y-direction due to the pole face rotation. As in the case of the sector magnet, the results of all 3 methods agree well.

4.3.3 CSR

Longitudinal CSR forces obtained from a semi-analytic formula (compare Eq. 3.39) for Gaussian sub-bunches are used to calculate the CSR fields in *ASTRA*.

To calculate the CSR-fields, the position and geometry of the bending magnets must be known. The required information is included in the orbit of the electron bunch. The trajectory of a reference particle, starting at position $\vec{x}_0$ with velocity $\vec{x}_0'$, is used as an

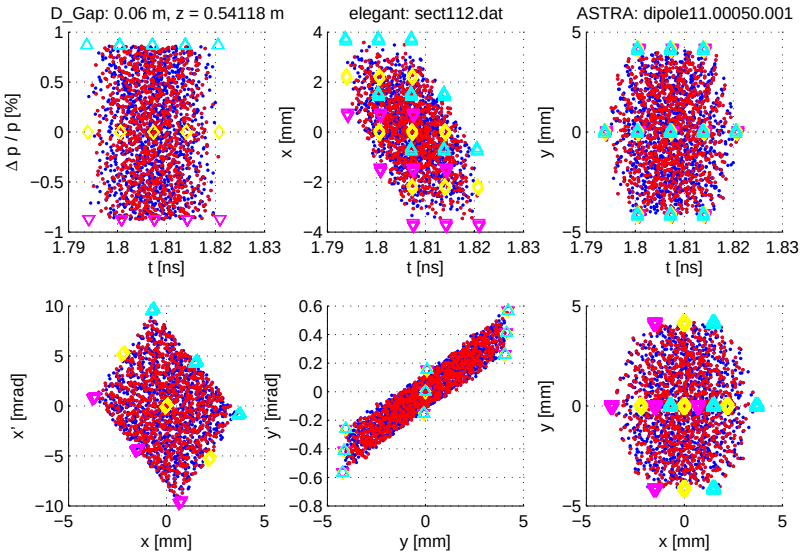

Figure 4.4: Phase space distribution at the end of tracking through a sector magnet ($L = 0.2\ m, \alpha = 30°$); The *elegant* distribution is shown in blue (2k particles) and the *ASTRA* distribution in red (1k particles); results from first order matrix transportation are shown as dots.

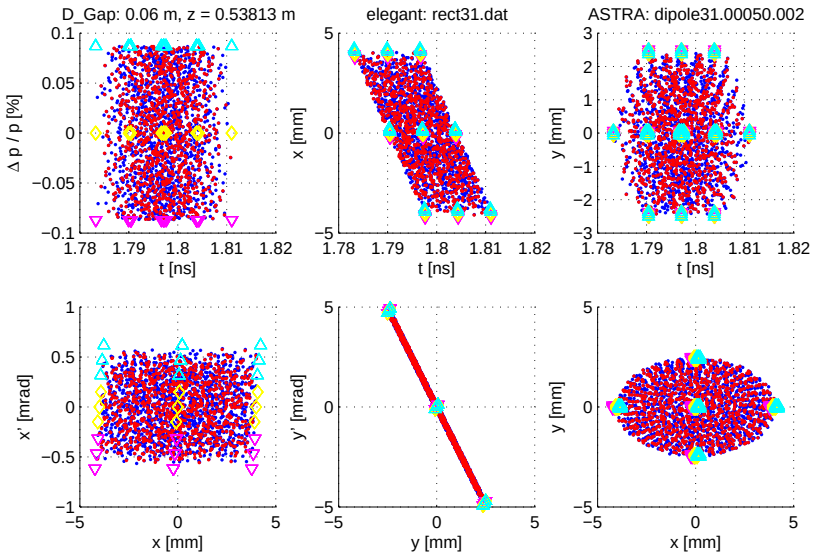

Figure 4.5: Phase space distribution at the end of tracking through a rectangular magnet ($L = 0.2\ m, \alpha = 30°, \beta_1 = \beta_2 = 15°$); The *elegant* distribution is shown in blue (2k particles) and the *ASTRA* distribution in red (1k particles); results from first order matrix transportation are shown as dots.

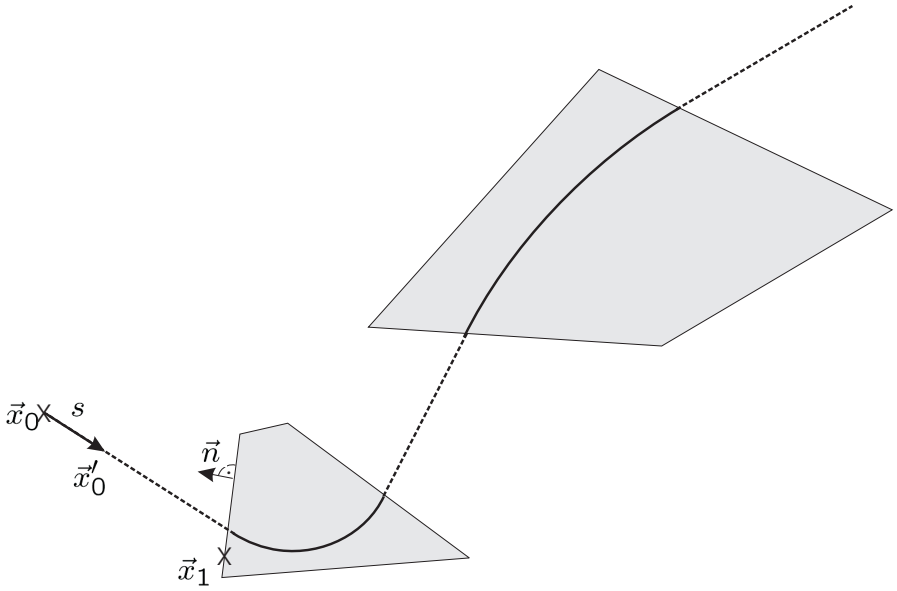

Figure 4.6: An ideal reference orbit can be given as a set of straight lines (dashed) and arcs of a circle (solid), corresponding to trajectories outside or within an dipole, respectively. Horizontal deflecting dipoles are indicated by the grey boxes.

reference orbit to determine the CSR fields. The 1D CSR model given in [Sal97] assumes either linear or circular motion of the electron bunch. In order to obtain those forces, the electron orbit along the chicane has to be decomposed into straight and circular orbit sections (see Fig. 4.6). For this purpose, hard edges of the dipole fields are assumed, using the field boundary lines of the dipoles (compare Sec. 4.3.1). These intersections between the reference orbit, represented by straight lines and arcs of a circle, and the dipole edges are calculated analytically. The derivation of the following formulae is given in Appendix D.

The beamline is separated into a set of segments with length s and a bending radius R. Starting from the initial centre-of-mass of the beam, one follows a straight line until a magnet boundary is crossed. The length s_l of a straight section is given by

$$s_l = \frac{(x_1 - x_0)n_x + (y_1 - y_0)n_y}{\frac{x'_0}{\sqrt{x'^2_0+y'^2_0}}n_x + \frac{y'_0}{\sqrt{x'^2_0+y'^2_0}}n_y} \tag{4.8}$$

with $\vec{x}_0 = (x_0, y_0)$ being the starting point of the section, $\vec{x}'_0$ the mean velocity at the starting point, $\vec{x}_1 = (x_1, y_1)$ a point on the magnet edge, and $\vec{n} = (n_x, n_y)$ the normal vector perpendicular to the magnet boundary (see Fig. D.1). The starting point $\vec{x}$ for the following bending section is given by

$$\vec{x} = \frac{s}{\|\vec{x}'_0\|}\vec{x}'_0 + \vec{x}_0 \tag{4.9}$$

In a bending section, the path length is given as $s_c = R\alpha$, here

$$\alpha = \arcsin\left(\frac{\frac{\vec{x}_0'}{\|\vec{x}_0'\|} \cdot (\vec{x} - \vec{x}_0)}{R}\right), \tag{4.10}$$

$\vec{x}_0$ is the starting point of the bend section, R is the bending radius, and $\vec{x}$ is the point where the circular orbit crosses the field boundary at the exit of the dipole (compare Fig. D.2) ($\vec{x}$ is calculated in Appendix D). With the decomposed orbit, the wake at each point of the trajectory can be calculated for a Gaussian sub-bunch [Sal97]. Convolution of this sub-bunch wake with the current profile along the bunch gives an approximation for the wake of the whole bunch (see Sec. 4.2.1).

The positions of each macro-particle are projected onto the tangent at the reference orbit, giving a set of longitudinal positions for the whole electron bunch. From these longitudinal positions the line charge density or current is calculated.

4.3.4 Space Charge and CSR in ASTRA

In *ASTRA* all forces, from quadrupoles, space charge, or CSR fields, are added to give the total field. The 1D CSR model does not contain Coulomb forces, since they are explicitly subtracted [Sal97], and one would expect no problem from adding the CSR and space charge forces.

On the other hand, the space charge model used in *ASTRA* is not suitable for dispersive sections. The space charge routine assumes a bunch moving on the axis perpendicular to the photo-cathode. In bend sections, one has to set up a rotated grid for the force calculation. The assumption of the 2D cylindrical space charge model, a rotationally symmetric bunch, is not fulfilled because the beam is spread out, due to transverse dispersion in bend sections. One, therefore, has to use the 3D spatial grid space charge algorithm.

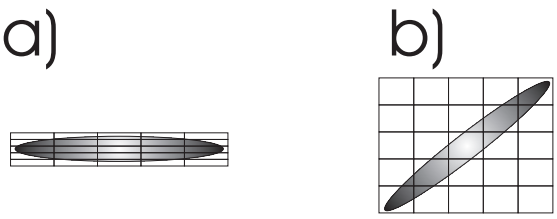

Figure 4.7: If a bunch is not concentrated along the grid dimensions (b) a grid which covers more volume than a bunch lined up (a) is required. Here both bunches are covered with a grid of 5 times 5 cells.

Since the transverse bunch shape is a map of the energy correlation, the head and tail of a bunch are on different sides of the reference orbit. The resulting bunch shape is not concentrated inside a cuboid anymore (compare Fig. 4.7). As a result, more grid cells

are required to obtain a good representation of the bunch's fine structure. An increase of grid cells requires a higher macro-particle number for accurate space charge calculations. Many cells are sparsely populated which makes the whole algorithm inefficient.

As discussed before (compare sections 3.2 and 3.4) space charge contributions are much weaker compared to CSR self-forces in short sections. Our approach to deal with the inaccuracies in the space charge models is to neglect space charge contributions inside the bunch compressor chicanes, since the total space charge contributions are an integrated effect over the whole linac. The CSR model in *ASTRA* allows the user to set up sections in the beamline in which CSR forces are enabled. This saves a lot of computational time and is justified, since CSR forces decay with one over the distance to the last dipole magnet. In each of those sections, space charge calculations can be deactivated.

With these modifications *ASTRA* can be used to perform start-to-end simulations of a machine in a single run. For high precision studies, however, one has to switch between different codes to cover all effects e.g. a full 3D CSR field calculation in *CSRTrack*, or wake fields of the accelerating modules.

More informations about the interplay of space charge- and CSR-interactions in bunch compressor chicanes are given in Appendix E.

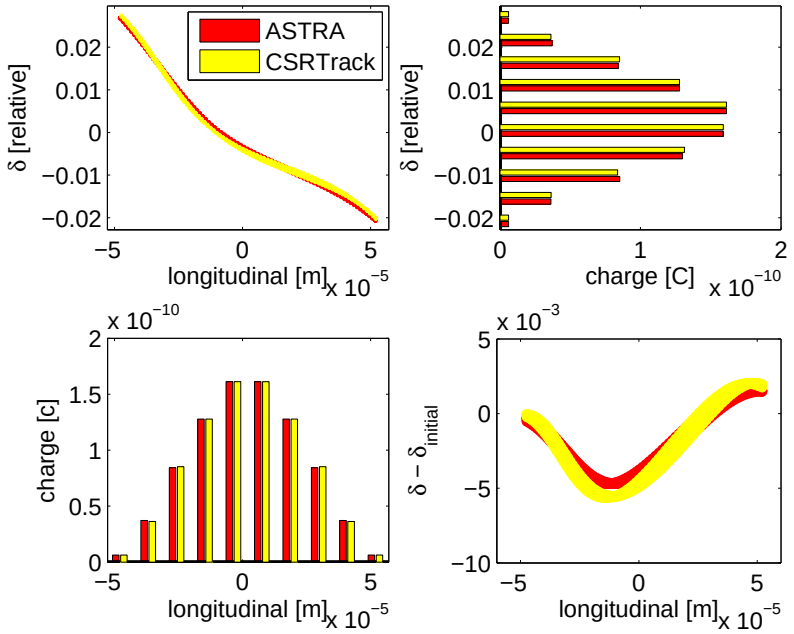

Figure 4.8: The longitudinal phase space is compared between *CSRTrack*(yellow) and *ASTRA*(red) (top left). Projections of the longitudinal phase space distributions are shown right and below. CSR induced δ change is given right bottom.

4.3.5 Comparison with CSRTrack

In this example, CSR fields in *ASTRA* and *CSRTrack* use the longitudinal field of a 1D Gaussian sub-bunch of constant width σ along the bunch. This width σ varies with bunch length along the chicane. For a comparison, we have chosen a bunch with no complicated sub-structure. 1000 macro-particles are distributed in phase space on a regular grid to achieve a constant slice and projected emittance of $\varepsilon_x = 1$ mm mrad. Since the longitudinal structure is set up on a regular grid, no sophisticated smoothing is needed in this example. A linearly correlated energy spread of $\sigma_E = 4.68$ MeV is induced along the $\sigma_s = 72.4$ μm long bunch with a total charge of $q = 0.833$ nC and an initial peak current of $I = 800$ A. Final peak current is $I = 5$ kA. The uncorrelated energy spread is zero. A 4 bend chicane, comparable to BC2 of FLASH, is used for the calculations (see Appendix E.1 for details). After the chicane, the bunch length is $\sigma_s = 19.2$ μm with a peak current of $I = 3$ kA. The longitudinal phase space after the chicane is shown in Fig. 4.8. The agreement downstream of the chicane is reasonable good (Fig. 4.8 (bottom right)).

In the horizontal plane, the phase space is more complicated. The initial bunch is set

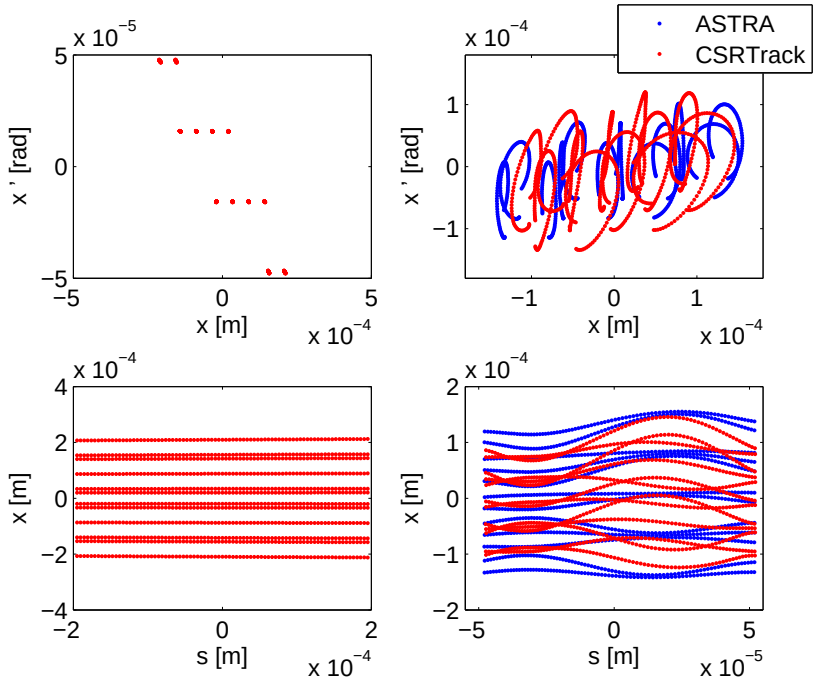

Figure 4.9: Initial horizontal phase space (left top) and initial "top view" (left bottom). Final horizontal phase space (right top) and final "top view" (right bottom).

up along a regular grid in a horizontal phase space which is unchanged along the bunch (Fig. 4.9 (left column)). After CSR interactions, the energy profile along the bunch is changed, leading, due to dispersion, to different horizontal phase space distributions for each slice. As a result, the horizontal positions, as well as the transverse momenta, are not constant along the bunch (Fig. 4.9 (right column)).

The emittance increased to a value of $\varepsilon_x = 2.5$ mm mrad in *ASTRA* and *CSRTrack*. The disagreement in the phase space distribution is related to the fact that *ASTRA* is including the fringe fields of the dipoles. In *CSRTrack*, however, the dipole fields have sharp field transitions and fringe field effects are neglected. A direct comparison is not possible since the dipole fringe fields in *ASTRA* can not be switched off because a sharp field boundary would lead to discontinuities in the Runge-Kutta integrator. Even a smooth, but very steep increase of the fringe fields is not satisfactory, since the $B_{\parallel}(d, h)$ component increases to very high values, forming a δ-peak like force profile (compare Eq. 4.6).

5 Measurements on CSR Induced Centroid Shifts at FLASH

5.1 Introduction

Measurements of the CSR induced horizontal shifts of the centroid positions along the bunch were done at FLASH in 2006. A transverse deflecting RF-structure [Emm01] [Bol05] is used to take "top view" pictures of the bunch - the projection into the longitudinal-horizontal plane. Thus, horizontal centroid shifts along the bunch can be observed.

As described in 3.4.2 other forces, like space charge or wake fields, may cause transverse shifts of beam centroids as well. For an undisturbed measurement of CSR effects, other self-field effects have to be reduced. As a consequence, we over-compress the bunch. The longitudinal energy correlation (chirp) introduced in the accelerating module upstream of the first bunch compressor chicane is chosen to reach minimum bunch length and a peak current beyond 1.2 kA toward the end of the second magnet in the BC2 chicane. The bunch will exit the chicane with its incoming length of about 2 mm RMS, corresponding to about 50 A peak current. The integrated effect of space charge from the exit of BC2 to the transverse deflecting cavity is then small compared to the distortions caused by CSR. In this compression scheme we expect an quantitative experimental confirmation of the simulation results in the regime up to $q = 1$ nC. For higher bunch charges, stronger self-interactions, even for the over-compressed beam, may complicate the analysis. In these cases, stronger wake field contributions are expected due to higher bunch length and bunch charge.

In April 2006 first measurements of the CSR induced centroid shifts were successful [Beu06a][Beu06b]. Fig. 5.1 shows measured longitudinal-horizontal projections of the bunch for different compression scenarios. If not stated otherwise the bunch head is assumed to be left in all the following images. In the uppermost picture, the ACC1 phase is on crest, no compression occurs and the horizontal centroid positions line up straight. Close to full compression (middle picture), the beam is heavily distorted by CSR and space charge effects (see Sec. 3.4). This is understood and simulated [Doh05], but would be very challenging as a starting point for quantitative CSR studies. The bottom picture shows the over-compressed case, where the space charge effects are negligible and strong CSR occurs only in BC2. The beam centroids are on a smooth line. The middle part of the bunch developed a horizontal offset of about a millimetre.

Fig. 5.2 shows measured bunch length at the transverse deflecting cavity as a function of the ACC1 phase as well as simulation results[1]. The measured bunch length agrees

[1] Longitudinal simulations were done with the *LITrack* [Ban05] assuming an initial FWHM bunch length

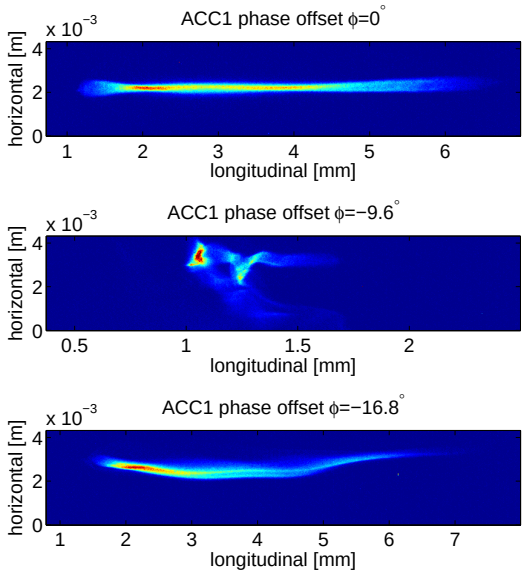

Figure 5.1: Measured top view for different ACC1 phase offsets. No compression (top). Near full compression (middle). Over-compression (bottom). Bunch head is to the left.

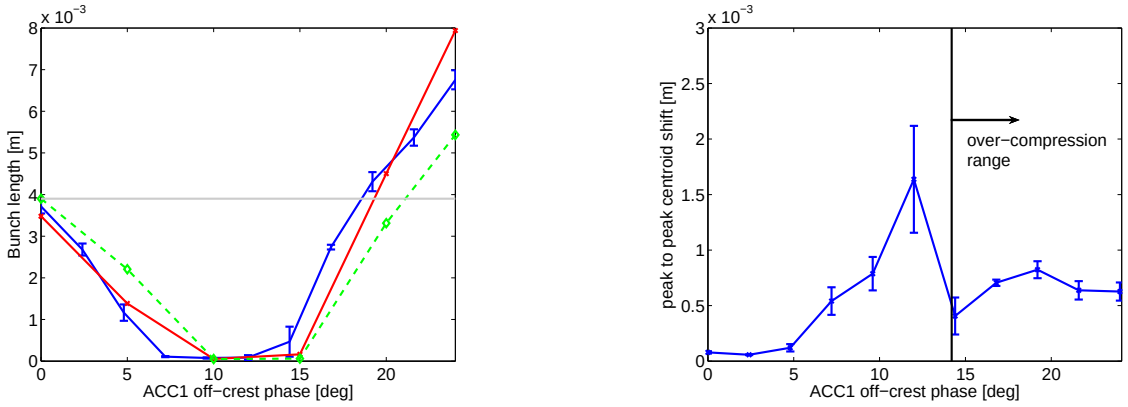

Figure 5.2: (left) Measured FWHM bunch length at the transverse deflecting cavity (blue line) are compared with simulations. Red line: calculated bunch length at the transverse deflecting structure. Green line: calculated bunch length after BC2. (right)The horizontal peak to peak centroid shift along the bunch is plotted against the phase offset in ACC1. Phase range used for the over-compression experiment is in this case 14 to 24 degrees. In the phase range between 5 and 14 degrees strong self-forces widen the horizontal profile.

well with the simulation downstream of BC3. Below $\approx 10°$, the calculated bunch length downstream of BC2 (green line) is bigger, since the bunch is further compressed in BC3. At about 12 degrees, the bunch is fully compressed in BC2. Above 12 degrees, the bunch is over-compressed, the chirp changes its sign and the bunch length at the exit of BC2 is smaller.

An example for centroid shifts for different phase offsets is shown in Fig. 5.2. From the difference between the on-crest and over-compression cases one clearly sees the CSR effects. The actual numbers of the phase offsets depend on the experimental set up like the bending strength of the dipoles in the chicane.

A next step is not only the qualitative demonstration of the predicted CSR induced centroid shifts (compare Sec. 3.4.2), but the quantitative verification of the expected charge dependence (compare Sec. 3.4.3). More detailed simulations of the CSR induced centroid shifts are required than simplified longitudinal calculations of the bunch length (Fig. 5.2), to study these effects in detail. A careful and well defined set-up of the beam optics and the bunch compression system is required for a reliable comparison with the simulations.

In this chapter the quantitative measurements of CSR induced centroid shifts and their charge dependence, including the image and data analysis, and comparison with simulations are presented.

of $\sigma_z = 3.3$ mm, uncorrelated energy spread $\sigma_\delta = 0.1$ % and 100.000 macro-particles. Energy gain was set to 108.5 MeV in ACC1 and 240 MeV in ACC2 and ACC3, using measured machine parameters. From the magnet currents the R_{56} of BC2 and BC3 were determined to be -185 mm and -240 mm, respectively. All acceleration modules except for ACC1 were set on-crest.

5.2 Experiment

5.2.1 Experimental Outline

For the experiments, we vary the ACC1 phase and keep ACC2/3 and ACC4/5 on crest. The expected CSR effects are created during over-compression in BC2. Downstream, the transverse deflecting RF structure (TDS) is used to analyse the longitudinal-horizontal beam profile.

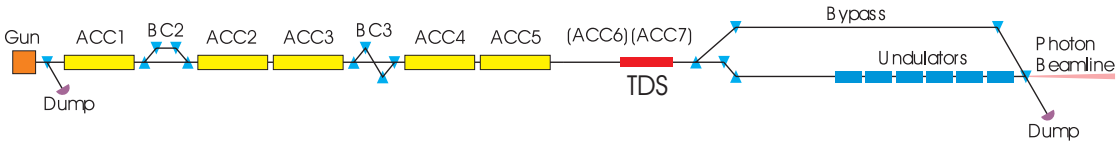

Figure 5.3: Sketch of FLASH. The blue triangles indicate dipole magnets, the yellow boxes symbolise TESLA accelerator modules.

Starting from a stable SASE working point, we achieved good transmission of the beam in the over-compression range from $\varphi_{ACC1} = 23°$ to $\varphi_{ACC1} = 26°$. For these phases, the energy gain in ACC1 differs notably from the on-crest energy gain by a factor of $\frac{\Delta E}{\Delta E_0} \approx \cos(26°) = 0.899$. These energy differences would lead to orbit errors through dispersion, and an optics mismatch with respect to the nominal beam optics. These effects are compensated through a higher accelerating gradient in ACC1.

In nominal beam operation, the energy gain in ACC1 is near the hardware limit, and this making significantly higher gradients impossible. To compensate for this, the energy of the beam line has to be reduced by scaling the dipole and quadrupole magnet currents down as well as the accelerating gradients. The energy gain of the first accelerating module ACC1 is reduced from $\Delta E_{\mathrm{ACC1}} \approx 120$ MV/m to $\cos(\varphi_{\mathrm{ACC1,max}})\Delta E_{\mathrm{ACC1}}$ to allow for off-crest gradient compensation up to phase $\varphi_{\mathrm{ACC1,max}}$. A typical maximal off-crest phase of 26° corresponds to a reduced ACC1 energy gain of $\Delta E_{\mathrm{ACC1}} \approx 107.9$ MV/m.

The scaling factor S after the modules ACC1 is calculated by the ratio of beam energies on- and off-crest. Thus S is

$$S_{\mathrm{ACC1}}(\varphi_{\mathrm{ACC1,max}}) = \frac{E_{\mathrm{ACC1}}(\varphi_{\mathrm{ACC1,max}})}{E_{\mathrm{ACC1}}(0°)} = \frac{\Delta E_{\mathrm{Gun}} + \Delta E_{\mathrm{ACC1}} \cos(\varphi_{\mathrm{ACC1,max}})}{\Delta E_{\mathrm{Gun}} + \Delta E_{\mathrm{ACC1}}} \tag{5.1}$$

while $\Delta E_{\mathrm{Gun}}, \Delta E_{\mathrm{ACC1}}$ are the energy gains of the RF Gun and the accelerating module ACC1. The scaling downstream of ACC1 is done similarly. Generally, the scaling factor, S_N, downstream of acceleration module ACC N is given by

$$S_N = \frac{\sum_{i=0}^{N} \Delta E_{\mathrm{ACC}\ N} \cos\left(\varphi_{\mathrm{ACC}\ N,\mathrm{max}}\right)}{\sum_{i=0}^{N} \Delta E_{\mathrm{ACC}\ N}}, \tag{5.2}$$

with $\Delta E_{\mathrm{ACC}\ 0} = \Delta E_{\mathrm{GUN}}$ and $\varphi_{\mathrm{ACC}\ N,\mathrm{max}}$ being zero except for ACC1.

The magnitude of the CSR induced centroid shifts on the screen at the transverse deflecting cavity depends not only on the self-interactions in BC2, but also on the beam

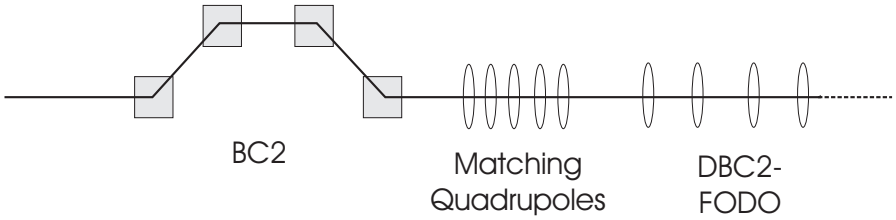

Figure 5.4: Sketch of the quadrupole system downstream of BC2. The first five quadrupoles are used for optics matching. Beam optics measurements take place in the FODO section downstream.

transport downstream of BC2. An induced centroid shift is subject to betatron oscillations. The amplitude and the sign of the centroid sag depend on the phase advance between the chicane and the screen and the beta-functions at the screen. To optimise the resolution of the measurements, a specific ratio of beta-function between the transverse deflecting cavity and the screen is set.

This is done by setting up dedicated optics between BC3 and the transverse deflecting cavity. A set of precalculated magnet settings downstream of BC3 that keeps the screen resolution constant while changing the phase advance is used. During the experiment, the phase advance was chosen to maximise the centroid shift on the screen.

To ensure a proper optics set-up, the emittance and Twiss parameters of the beam were measured in the DBC2 diagnostic section downstream the first bunch compressor using the four screen method [Loe05]. The measured Twiss parameters are used to determine corrections to the five quadrupoles upstream of this diagnostic section, after BC2, to achieve a matched beam optics in the DBC2 FODO lattice (see Fig. 5.4). A matched beam in the DBC2 FODO section ensures a well-defined optics downstream. The bunch charge is varied to measure the dependence of the centroid shifts on the charge. Due to space charge effects in the injector, the beam optics depends on the bunch charge. To ensure a good transmission up to the transverse deflecting cavity, the matching in the DBC2 section was redone for every bunch charge.

This procedure, however, complicates the data analysis because the quadrupoles used for the optics matching are located downstream of the chicane. Therefore, the beam transport from there to the TDS changes with bunch charge. Hence the transport of the centroid curve to the TDS is charge dependent. Therefore bunch charge dependent transfer matrices have to be determined for the later analysis.

5.2.2 The Transverse Deflecting RF-Structure

The projection into the horizontal-longitudinal plane of the electron bunches can be studied with a vertically deflecting travelling-wave RF-structure (TDS). The device was originally designed (by G. Loew, R. Larsen, and O. Altenmueller) at SLAC in 1968 as an RF separator for secondary particles [Alt64]. This transverse deflecting RF-structure (see Fig. 5.5) was already used for beam diagnostics at SLAC in the SPPS accelerator.

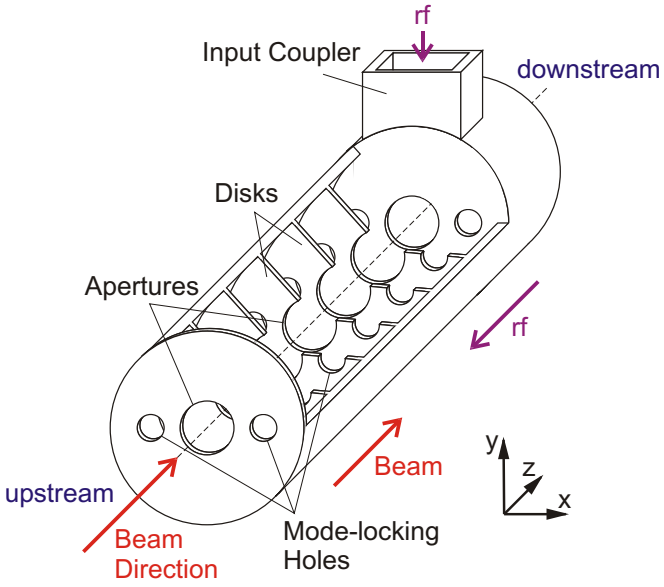

Figure 5.5: Cut-away view of the transverse deflecting cavity. The RF is feed into the cavity via an input coupler at the downstream end. The RF travels against the beam direction. The relatively big apertures in the disks cause a strong coupling of the fields. Possible rotations of the TM_{11}-mode are suppressed by the mode-locking holes in the disks (image taken from [Bol05]).

Installation at DESY was done in 2003 in cooperation with SLAC. It has been in operation since 2005 [Emm01][Bol05][Nag04]. Some Parameters are summarised in Tab. 5.1.

An electron bunch enters the transverse deflecting RF-structure at the zero-crossing phase of the deflecting RF field. The particles are kicked transversely with a strength proportional to their longitudinal offset to the bunch centre. The bunch is therefore tilted and its longitudinal-transverse projection is observed on a screen (Fig. 5.6).

From the Lorentz force $\vec{F} = e(\vec{E}+\vec{v}\times\vec{B})$ on a particle of charge e one gets a transverse momentum change on the bunch, which varies in time during the passage of the bunch. Although the force in the TDS arises from magnetic and electric fields it can be given using an equivalent electric voltage V_0 [Bol05][Nag04]. For the small kick angle $\Delta y'$ as a function of the longitudinal coordinate z along the bunch one finds

$$\Delta y' = \frac{eV_0}{pc}\sin\left(\frac{2\pi}{\lambda_L}z+\varphi\right) \approx \frac{eV_0}{p_z c}\left[\frac{2\pi}{\lambda_L}z\cos\varphi+\sin\varphi\right] \tag{5.3}$$

were V_0 is the vertical peak voltage, $p \approx p_z$ the longitudinal momentum, φ the RF phase compared to zero crossing of the field, λ_L the wavelength in the structure, and $\frac{2\pi}{\lambda_L}z \ll 1$. For the transverse position of each ultra-relativistic electron on a screen one finds

$$\Delta y \approx \frac{eV_0}{E_0}\sqrt{\beta_{y,L}\beta_{y,s}}\sin\Delta\psi_y \cdot \left(\frac{2\pi}{\lambda_L}z\cos\varphi+\sin\varphi\right), \tag{5.4}$$

Parameter	Value
Length	3.66 m
Nominal operating frequency:	2856 MHz
Filling Time	0.645 μs
Nominal deflecting voltage	25 MV
RF power	18 MW
Mode Type	TM 11 (Hybrid Mode)

Table 5.1: Summary of some parameters of the transverse deflecting RF-structure.

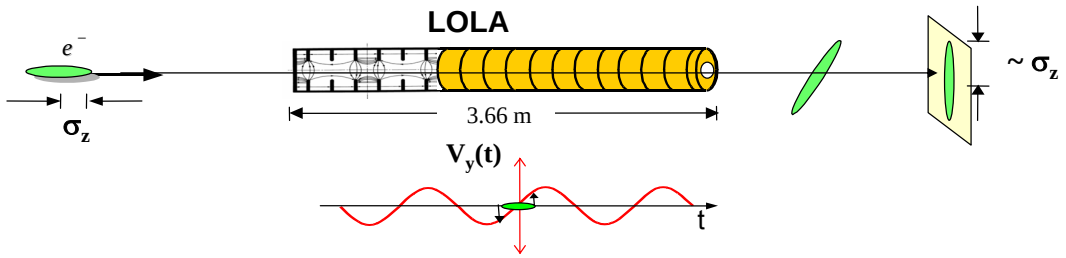

Figure 5.6: The bunch is travelling through a vertical deflecting cavity at the zero crossing resulting in vertical offset of the particles correlated to the longitudinal position. These offsets are imaged on a screen [Emm01].

with the vertical beta function at the TDS $\beta_{y,L}$ and at the screen $\beta_{y,s}$, respectively. $\Delta\psi_y$ is the betatron phase advance between the TDS and the screen. The transverse centroid offset, calculated as the mean with $\langle z \rangle = 0$, at the screen is

$$\langle \Delta y \rangle = \frac{eV_0}{E_0} \sqrt{\beta_{y,L}\beta_{y,s}} \sin \Delta\psi_y \cdot \sin \varphi. \tag{5.5}$$

Due to a deflecting voltage one gets a RMS beam size at the screen of

$$\sqrt{\left\langle (y - \langle y \rangle)^2 \right\rangle} \equiv \sigma_y = \sqrt{\sigma_{y_0}^2 + \sigma_z^2 \cdot \beta_{y,L}\beta_{y,s} \left(\frac{\frac{2\pi}{\lambda_L} eV_0}{E_0} \sin \Delta\psi_y \cdot \cos \varphi \right)^2} \tag{5.6}$$

were $\sigma_{y_0} = \sqrt{\beta_s \varepsilon_y}$ is the nominal beam size on the screen, and σ_z the RMS bunch length.

The RF voltage should be large enough that the streaked beam size on the screen dominates the nominal beam size. The peak voltage of the TDS can be estimated as $V_0 \approx 1.6 \text{ MV} L/\text{m} \sqrt{P_0/\text{MW}}$ (compare Tab. 5.1). One gets with typical FLASH parameters $\sigma_z \approx 25$ μm, $\sqrt{\beta_{y,L}\beta_{y,s}} \approx 51$ m, $\varepsilon_y = 5$ mm mrad, $\Delta\psi_y \approx 15.8°$, $\varphi = 0°$, $\lambda_L \approx 105$ mm, and a beam energy $E_0 = 600$ MeV a streaked beam size $\sigma_y \approx 925$ μm, which exceeds the nominal beam size of 317 μm by a factor of three.

5.2.3 Resolution of TDS measurements

In general the resolution of a TDS measurement is given by the spot size of a single slice on the screen. The horizontal spot size of a slice i is given by $\sigma_x^i = \sqrt{\beta_x^i \varepsilon_x}$. The longitudinal resolution depends on the streak induced by the transverse deflecting RF-structure. The streak factor $S = \frac{\Delta y}{\Delta t}$ can be measured (compare Sec. 5.2.4). If we write the vertical beam size of a single slice on the screen as $\sigma_y^s = \sqrt{\varepsilon_y \beta_{y,s}^s}$, the time resolution is

$$\sigma_t^s = \frac{\sqrt{\varepsilon_y \beta_{y,s}^s}}{S}. \tag{5.7}$$

During the measurements the typical values for the beta-functions at the screen were $\beta_{x,s} = 10.0$ m/rad and $\beta_{y,s} = 1.5$ m/rad (see Fig. 5.7). Assuming a normalised slice emittance of $\varepsilon_N = 2$ mm mrad and a beam energy of $E_0 = 620$ MeV one gets for the beam sizes $\sigma_x = 0.128$ mm and $\sigma_y = 49.7$ μm. The horizontal beam size is an upper bound for the horizontal resolution. A typical resolution in the longitudinal direction is given by the vertical spot width of a slice and a typical streak of $\frac{1}{S} = \frac{50\text{fs}}{\text{px}}$ (compare Sec. 5.2.4). With a pixel size on the camera, taking into account the optical system, of 26.96 μm we get $S = 0.539 \frac{\mu\text{m}}{\text{fs}}$ and therefore $\sigma_t = 92.2$ fs.

5.2.4 Longitudinal Calibration

While the horizontal scale of the beam images are given by the camera and the imaging optics toward the screen as $\Delta x = \frac{26.96 \mu\text{m}}{\text{px}}$, the longitudinal calibration is determined by different machine parameters like the power in the transverse deflecting RF-structure

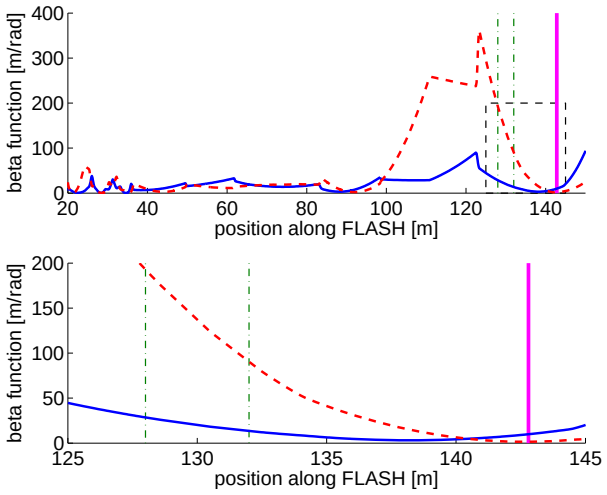

Figure 5.7: The transverse beta functions along FLASH (blue - horizontal, red dashed - vertical). In the lower figure a zoom to the dashed box from the upper figure is given. The TDS is represented as a green dashed dotted box while the screen is given by a magenta line.

or the beam optics. Therefore additional beam based calibration measurements are required to calibrate the longitudinal scale.

To calibrate the correlation between the vertical position on the screen and the longitudinal position along the bunch, the vertical deflection of the bunch is measured against the TDS phase. Phase differences of the RF-structure corresponds to a time delay according to

$$\Delta t = \frac{\varphi_{\mathrm{TDS}}[^\circ]}{360^\circ \cdot 2.856\ \mathrm{GHz}}. \tag{5.8}$$

Data was taken for different time delays or TDS phases relative to the beam. The RF power was chosen to have a picture of the beam in the strong over compression regime covering the whole screen. Afterwards the ACC1 phase offset was set to a value which leads to a longitudinally compressed beam on the TDS screen. The longitudinal profile of a compressed beam is sharp enough to determine a unique position along the bunch from which the vertical deflection is determined.

Since the beam was compressed, a clear centre position of the beam was defined by the peak maximum. The mean centre positions of all taken pictures were used to determine the linear correlation between time delay Δt and the vertical offset on the screen. An example of this measurement is shown in Fig. 5.8. The slope between the vertical offset on the screen and the time delay is the longitudinal calibration.

The longitudinal calibrations obtained depend on the power in the TDS and the beam optics in the machine. Since the TDS power was adjusted to cover the whole screen with the beam, and since the optics depend on the bunch charge, this calibration procedure

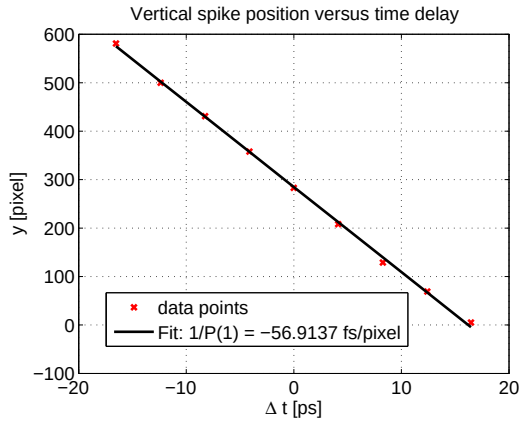

Figure 5.8: An example of the longitudinal calibration

was repeated for every measurement. A summary of these measurements for different bunch charges is shown in Table 5.2.

Bunch Charge [nC]	Calibration [fs/px]
0.4	46.6 ± 0.3
0.65	46.6 ± 0.3
0.8	46.6 ± 0.3
1.0	46.6 ± 0.3
1.2	56.9 ± 0.4
1.4	56.9 ± 0.4
1.6	61.1 ± 0.2
1.8	59.0 ± 1.0
2.0	59.0 ± 1.0

Table 5.2: Longitudinal calibrations for the TDS screen for different bunch charges.

5.2.5 Summary of Centroid Shift Data

The starting point of our measurements was a machine working under SASE conditions with a bunch charge of $q = 0.65$ nC. As a first step in our experiment we reduced the energy gain of ACC1. The energy gain of ACC1 was changed from $\Delta E = 120$ MV to $\Delta E = 104$ MV allowing off crest phases up to $\varphi = 30°$. The energy profile

$$E = E_{\mathrm{Gun}} + E_{\mathrm{ACC1}} + E_{\mathrm{ACC23}} + E_{\mathrm{ACC45}} \tag{5.9}$$
$$= (4.5 + 104 + 209 + 303)\ \mathrm{MeV} \tag{5.10}$$
$$= 620.5\ \mathrm{MeV} \tag{5.11}$$

was kept constant during our measurement by compensating for the energy loss caused by off-crest acceleration in ACC1 with higher accelerating gradients (compare Eq. 5.2).

As a second step, the optics between the exit of BC3 and the TDS screen were changed to ensure the correct ratio of beta functions at the transverse deflecting RF-structure and the screen. This required a matching of the beam in the DBC2 diagnostic FODO section. We then changed the phase advance between BC3 and the screen while keeping the ratio of beta functions constant, thereby maximising the observed CSR induced centroid shifts.

Data were taken for ACC1 on crest and at $\varphi = -22.7°, -23.8°, -24.9°, -26.0°$. Higher off-crest phases lead to beam losses. The power in the RF-structure was set to image the whole beam at $\varphi = -26°$ on the screen. This power was not changed during the ACC1 phase scan. After the images were stored, we changed the bunch charge, and repeated the matching in the DBC2 section.

A summary of the images is shown in Fig. 5.9, Fig. 5.10, Fig. 5.11,Fig. 5.12, and Fig. 5.13. The horizontal axis is the longitudinal dimension while the vertical axis represents the horizontal axis of the beam. The horizontal conversion of pixel to meter is constant while the longitudinal one depends on the TDS RF power and the beam optics (see Sec. 5.2.4). Each figure shows different bunch charges at a given phase offset in ACC1. The gain of the camera system was dynamically changed to prevent saturation effects in the images while keeping the signal to noise ratio as high as possible. The red lines represent the projection of the picture intensity onto the horizontal axis - if we assume a linear intensity response of the imaging system of the screen, they represent the charge distribution along the bunch. Each picture represents twenty pictures taken under the same machine conditions. The background was determined by taking ten images while the photo injector laser was blocked. An average of each set of background images is subtracted from the beam images.

On crest acceleration which induces no correlated energy spread suitable for compression results in a beam lined up straight. At higher bunch charges however the beam is tilted - this tilt is discussed further in Appendix B.

In the over-compression cases (i.e. $\varphi > 20°$) a banana shape is visible for all bunch charges. As in the on-crest case the high charge pictures have an additional slope. Another interesting feature are the spikes in the charge profiles of the 1.8 nC and 1.9 nC cases especially in the $\varphi = 22.7°$ images (Fig. 5.10 (bottom middle and right)). This behaviour is related to a partial over compression for long bunches and is discussed later.

The width of the bunch is increased in the region of maximum transverse centroid offset. This feature is more prominent at high bunch charges.

5.3 Data Analysis

The measured beam profiles have to be analysed to obtain informations about the general beam dynamics and CSR effects. This is particularly important in BC2. The CSR effects are easily identified if we compare the un-compressed beam (on-crest acceleration Fig. 5.9) with the over-compressed beam (acceleration in ACC1 with $\varphi > 20°$ Fig. 5.10 -

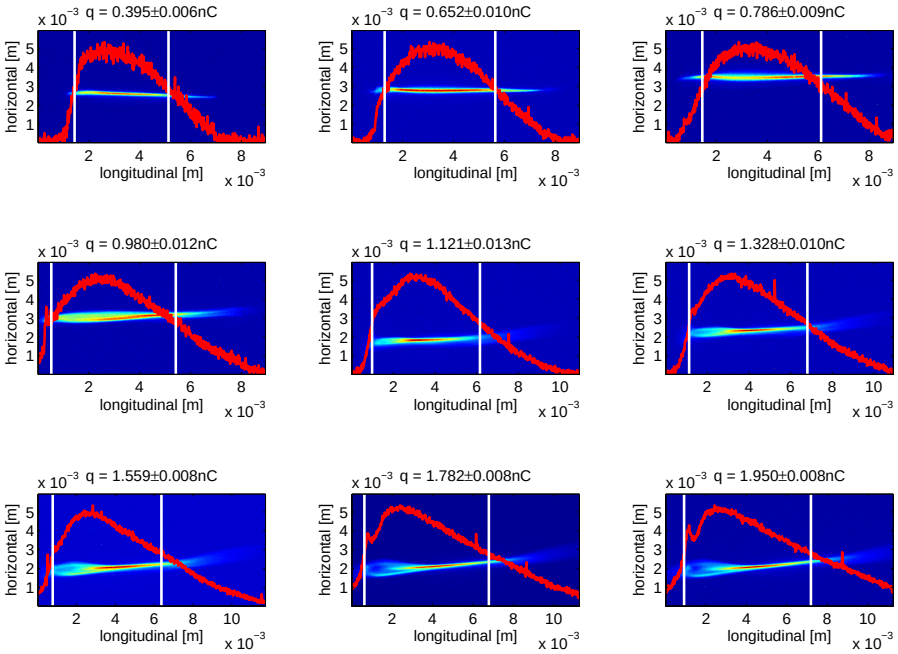

Figure 5.9: TDS images for ACC1 on crest.

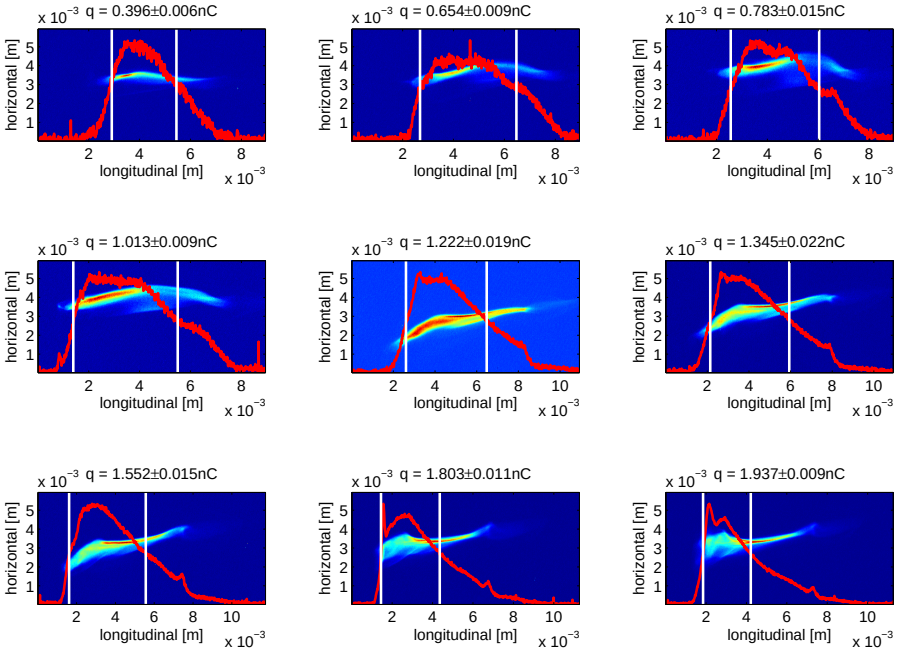

Figure 5.10: TDS images for ACC1 with a phase offset of $-22.7°$.

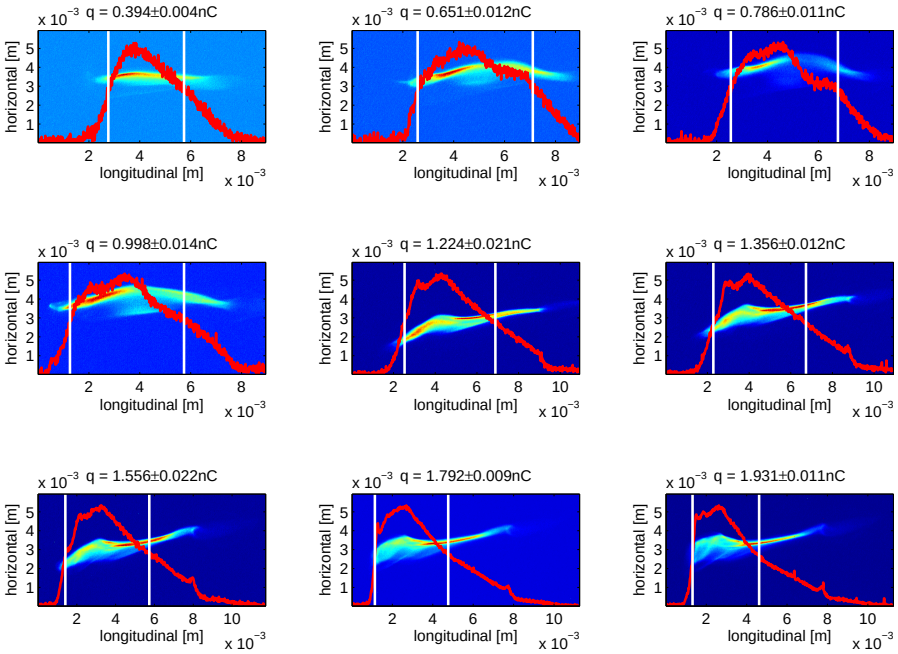

Figure 5.11: TDS images for ACC1 with a phase offset of $-23.8°$.

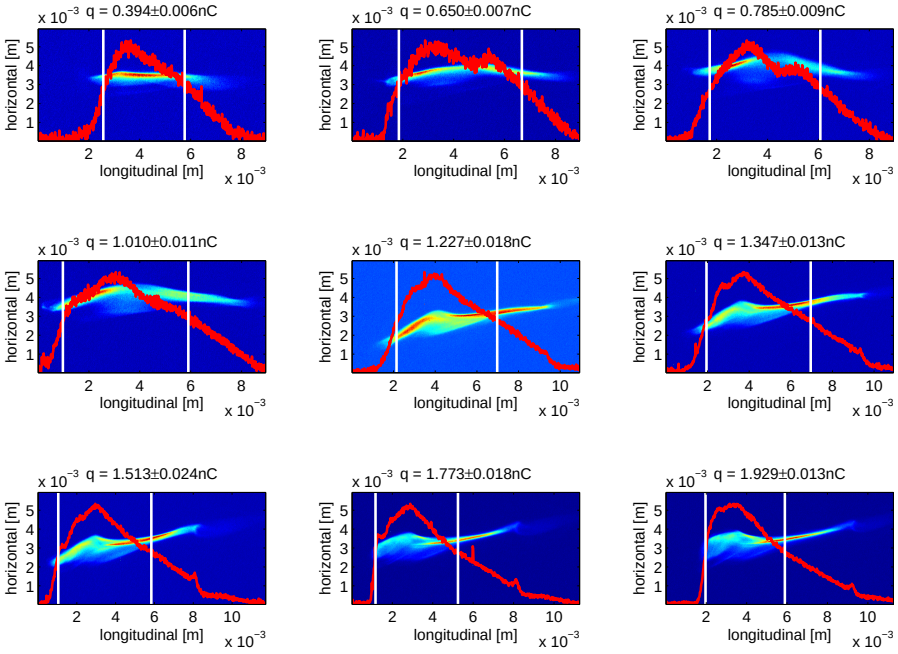

Figure 5.12: TDS images for ACC1 with a phase offset of $-24.9°$.

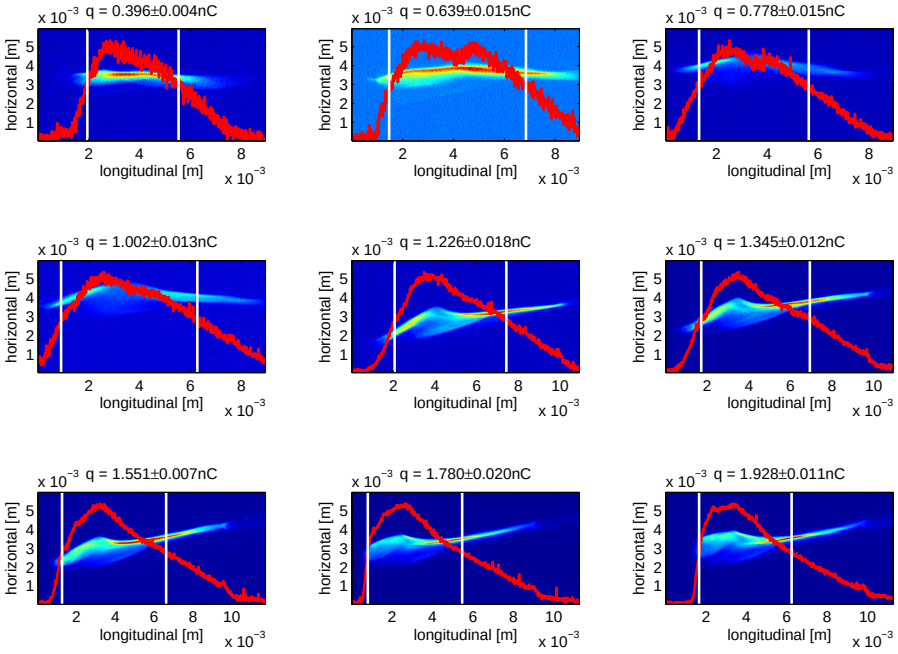

Figure 5.13: TDS images for ACC1 with a phase offset of $-26.0°$.

Fig. 5.13). In the over-compression range, we observe a horizontal deformation of the centroid curve.

In the first step of the following analysis, we determine the maximal horizontal displacement of the centroid curve along the bunch and use it as a measure for the strength of the CSR interactions. This maximal displacement compared to the straight (uncompressed) beam is related to the maximal energy loss per longitudinal bunch slice due to CSR in BC2. Other self-interactions downstream of BC2 are not likely to produce similar transverse deformations of the beam profile since the beam is not developing any high-charge spikes anymore. Therefore, the main contribution to the maximal displacement, referred to as maximal *centroid shift*, is assumed to be CSR effects in BC2 while other contributions are negligible.

While the maximal centroid shift is an important property to identify the strength of the CSR effects, it is not sufficient for the analysis of the beam dynamics. Hence, in the second step of this analysis the whole centroid curves are compared with simulated data (compare Sec. 5.4.2).

The following data analysis is done in different steps. After the bunch length as a function of the ACC1 phase offset and the bunch charge is determined, the centroid curves are determined by a detailed image analysis.

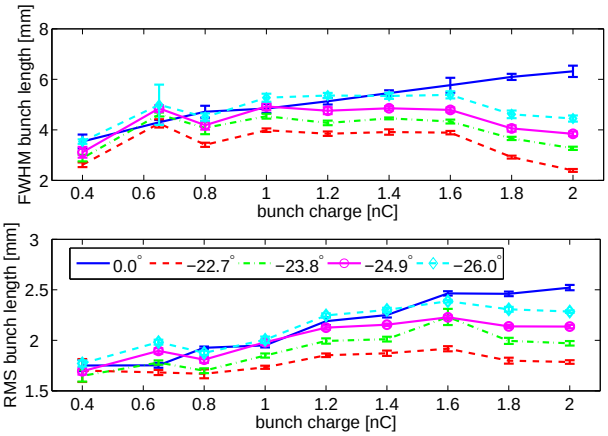

Figure 5.14: FWHM and RMS bunch length for different phases of ACC1 and bunch charges.

5.3.1 Bunch Length

The projection of the image intensity onto the longitudinal axis is calculated. Together with the longitudinal calibration, the width of this longitudinal charge profile can be translated into the bunch length. Bunch length is measured for different bunch charges and ACC1 phases. Data are shown in Fig. 5.14

We assume the longitudinal charge density ρ downstream of the bunch compressors to be an asymmetric Gaussian with widths σ_+ and σ_-

$$\rho(x) = \begin{cases} Ae^{\frac{-x^2}{2\sigma_-^2}} & \text{if } x < 0 \\ Ae^{\frac{-x^2}{2\sigma_+^2}} & \text{if } x \geq 0 \end{cases}$$

for on-crest acceleration in all modules. The normalisation factor A is determined from the total bunch charge

$$\int_{-\infty}^{\infty} \rho(x)dx = \frac{A\sqrt{2\pi}(\sigma_+ + \sigma_-)}{2} = q \Rightarrow A = \frac{2q}{\sqrt{2\pi}(\sigma_+ + \sigma_-)} \tag{5.12}$$

or

$$A = \frac{q}{\sqrt{2\pi}\hat{\sigma}} \tag{5.13}$$

with $\hat{\sigma} = \frac{(\sigma_+ + \sigma_-)}{2}$.

During our experiment we changed the bunch charge by changing the intensity of the photo injector laser while keeping the laser pulse length constant. As we have seen in section 3.4.3, due to space charge forces in the injector the bunch length increases with bunch charge.

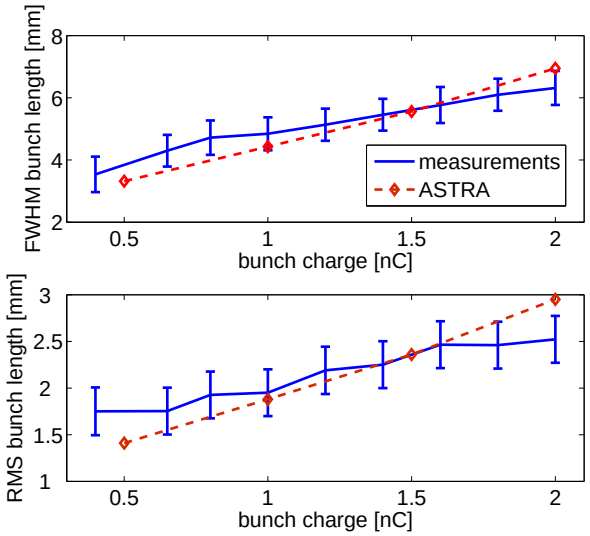

Figure 5.15: FWHM and RMS bunch length for on crest operation in ACC1 and different bunch charges compared with *ASTRA* simulations. Error bars of the measurements contain the statistical error and a systematic contribution from the vertical beam size at the TDS (compare Sec. 5.2.3). *ASTRA* simulations are at the exit of ACC1 while the measurements are about 60 m downstream at the TDS. Since the beam is not monoenergetic even in on crest operation the bunch length changes slightly.

	$\sigma = 1.5$ mm	$\sigma = 2.5$ mm
ACC1 Phase [°]	σ_E/E[%]	σ_E/E[%]
0	0.11	0.31
5	0.36	0.65
10	0.70	1.19
15	1.06	1.78
20	1.43	2.40
25	1.83	3.06

Table 5.3: The relative correlated RMS energy spread $\sigma_E/E = \sqrt{\left\langle (\delta - \langle\delta\rangle)^2 \right\rangle}$, generated by the first accelerating module ACC1 as a function of the phase, is calculated for initial RMS bunch lengths of $\sigma = 1.5$ mm and $\sigma = 2.5$ mm. Beam energy is $E = 108$ MeV.

With increasing bunch charge the space charge forces stretch the beam to higher bunch length. The FWHM bunch length on crest varies roughly linearly from $\sigma_{0°}^{\mathrm{FWHM}} = 3.5 \pm 0.3$ mm for $q_{0°} = 0.4$ nC to $\sigma_{0°}^{\mathrm{FWHM}} = 6.3 \pm 0.2$ mm with $q_{0°} = 2.0$ nC (Fig. 5.14). This behaviour agrees qualitatively with the *ASTRA* simulations. The deviation between the measured and the simulated data is caused on one hand by the fact that the simulated bunch length at the exit of ACC1 is compared with measured values at the TDS further downstream. On the other hand, there is a dependency of the bunch length on different RF-gun parameters like the RF-phase or the duration of the laser pulse [Lip04] which are not known precisely enough for perfect simulations. A fine tuning of these simulation parameters is not done here. If the accelerating modules are on-crest, bunch length changes in the chicanes BC2 and BC3 are negligible. Therefore the measured bunch length at the TDS is compared with the results of tracking calculations from the cathode downstream to the exit of ACC1 (Fig. 5.15).

The correlated RMS energy spread (Tab. 5.3) induced by the accelerating module ACC1 in off-crest operation leads to compression of the beam. In this calculations we assumed a linear equidistant particle distribution along the longitudinal axis with a Gaussian charge profile of different widths σ. Values of the RMS bunch length were chosen as $\sigma = 1.5$ mm and $\sigma = 2.5$ mm which covers the range shown in Fig. 5.15.

Off-crest phases around $\varphi_{\mathrm{ACC1}} \approx -8°$ to $-16°$ lead to short bunch lengths after the chicanes. Our experiment uses off-crest phases in the range higher than $\varphi_{\mathrm{ACC1}} < -20°$, the over-compression regime. The bunch is compressed within the first part of BC2. The correlated energy spread is large enough that the tail of the bunch overtakes the head within the chicane, leading to an elongation of the bunch in the second part of the chicane. Head and tail of the bunch are exchanged after BC2 in this over compression scenario. Thus the sign of the correlated energy spread is flipped, leading to further stretching of the beam in the second chicane BC3.

Fig. 5.14 shows the bunch length on-crest and in the over-compression regime. In the over-compression range the bunch length increases with higher off-crest phases. The

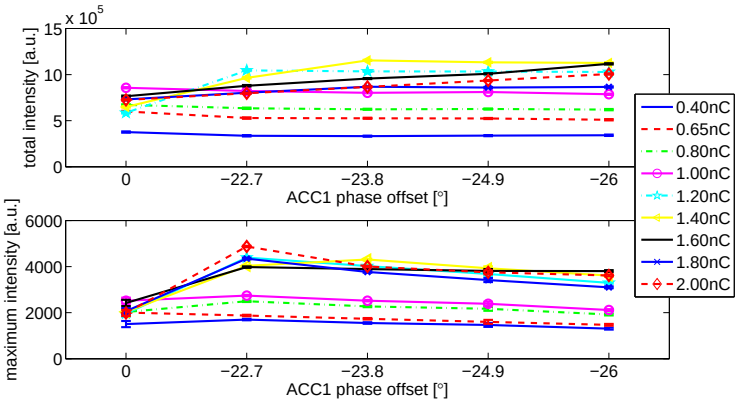

Figure 5.16: (top) By summing the signal of all pixels the total image intensity is calculated. It is shown here for different bunch charges as a function of the phase. (bottom) The maximum intensity of the longitudinal image profile for the same charges as in the upper plot.

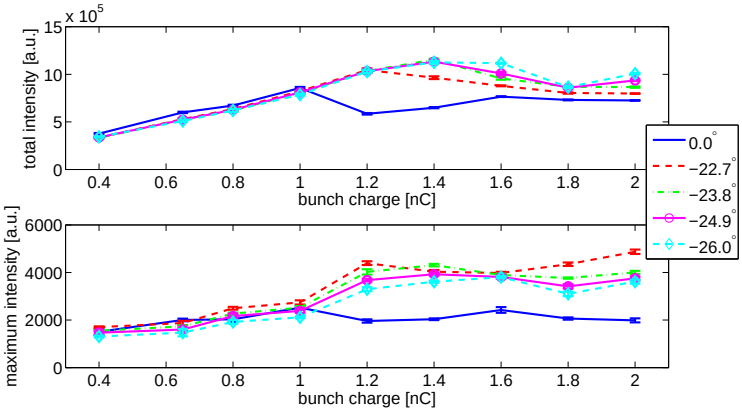

Figure 5.17: (top)As in Fig. 5.16 but the intensity is shown for different ACC1 phase offsets as a function of bunch charge. (bottom) Maximum intensity of the longitudinal image profile for the same phase offsets as in the upper plot.

behaviour of bunch length in this range is, however, more complicated compared with the on-crest situation. First of all the FWHM curve is flat between $q = 1$ nC and $q = 1.6$ nC. The measured FWHM bunch length goes down for higher bunch charges $q > 1.6$ nC. In addition the measured value for the $q = 0.65$ nC case seem to be too high compared to the neighbouring data.

Since the energy changes caused by self-field effects are small compared to the correlated energy spread generated by the acceleration modules, one might expect the curve bunch length versus charge to have a similar shape like the on-crest curve. Especially for the FWHM curves in over-compression this is not the case. Decreasing bunch length at bunch charges higher than 1.6 nC is in disagreement with the bunch length simulations in the injector (compare Fig. 5.15).

In Fig. 5.16 and Fig. 5.17 the total intensity and the maximum intensity of the images are compared for different bunch charges and ACC1 phase offsets. Total intensity increases nonlinearly with total bunch charge above $q = 1.0$ nC. A nonlinear behaviour of the picture intensity, however, leads to image intensity profiles which are not identical to the beam charge profiles. Furthermore, the intensity is not even independent of the phase offset in the first accelerating module in the high charge cases.

The reason for the nonlinear behaviour is the gain adaptation used during the experiment. The gain of the camera was adapted to cover the whole intensity range of the camera while avoiding saturation in the high intensity regions of the beam profile. As a result the total image intensity would drop down for images with a narrow transverse structure with high intensity peaks. Narrow transverse profiles accumulate more intensity in less pixels which leads to a total gain reduction to avoid saturation. A reduction of the gain, however, cause the tails of the beam profile to be lost in the noise of the image, thereby reducing the calculated bunch length.

Using camera gain adaption for beam images with a varying transverse profile leads to systematic errors in the bunch length measurements. Since the bunch length measurement was not the focus of the measurement we did not optimise the setup for this.

5.3.2 Image Analysis

Beam images taken with the TDS in the over-compression mode have a 'banana' shape. Without strong CSR effects the beam is lined up straight. We choose the maximum transverse displacement of the slice centroids with respect to a straight beam as a measure for the strength of the CSR effects. Our next task is to extract information about the centroid positions from the images.

A standard procedure in the beginning of image analysis is the subtraction of background images. Under all conditions images are taken twice with beam and without by blocking the laser of the photo injector. The mean of all background profiles is subtracted from each beam image to get rid of beam independent features like dark current.

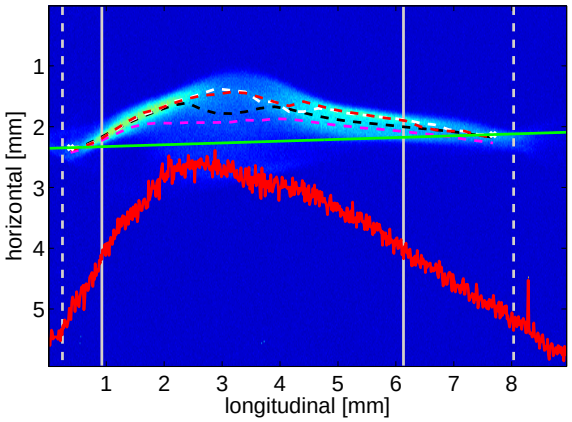

Figure 5.18: An example of a TDS measurement. Longitudinal charge profile (red line), FWHM lines (white solid) and the lines corresponding to "full width of 1/6 maximum" (white dashed) are shown. Different centroid curves (black - Gaussian fit/white - maximum value/magenta - mean value/red - double Gaussian fit) are plotted as dashed lines. The green line represent an overall linear slope determined from the edge points of the centroid curves (compare Sec. 5.3.3). Bunch head is to the left.

5.3.3 Transverse Slice Profiles

In a first step after background subtraction, each picture is divided into slices along the longitudinal axis. Only the central part of the pictures is analysed. The head and tail sections are omitted because of the noise in these low charge regions. This region is defined by the points corresponding to the 1/6 maximum value of the charge profile.

Next, the horizontal charge profiles of these slices are calculated. Within these horizontal charge profiles the centre position has to be determined. The maximum or the centre of mass can be used for such a definition. The centre of mass within such a slice is strongly influenced by noise in the empty regions of the picture, drawing this value to the geometrical centre of the slice. Therefore, a Gaussian fit to the charge profile is a better choice, but is not completely appropriate to our situation. The horizontal charge profiles are not Gaussian but asymmetric in the regions of the picture with strong centroid shifts which lead to an underestimation of the centre. The maximum of such a profile does not underestimate the centroid shifts but is unstable due to noise in the charge profiles.

A double Gaussian

$$f(x) = a_1 e^{-\left(\frac{x-a_2}{2a_3}\right)^2} + a_4 + a_5 e^{-\left(\frac{x-a_6}{2a_7}\right)^2} \tag{5.14}$$

is used to fit the data. As initial values for the fit of a_2 and a_6 we use the maximum and the mean of the transverse charge profile. a_2 is then a good choice for the centre

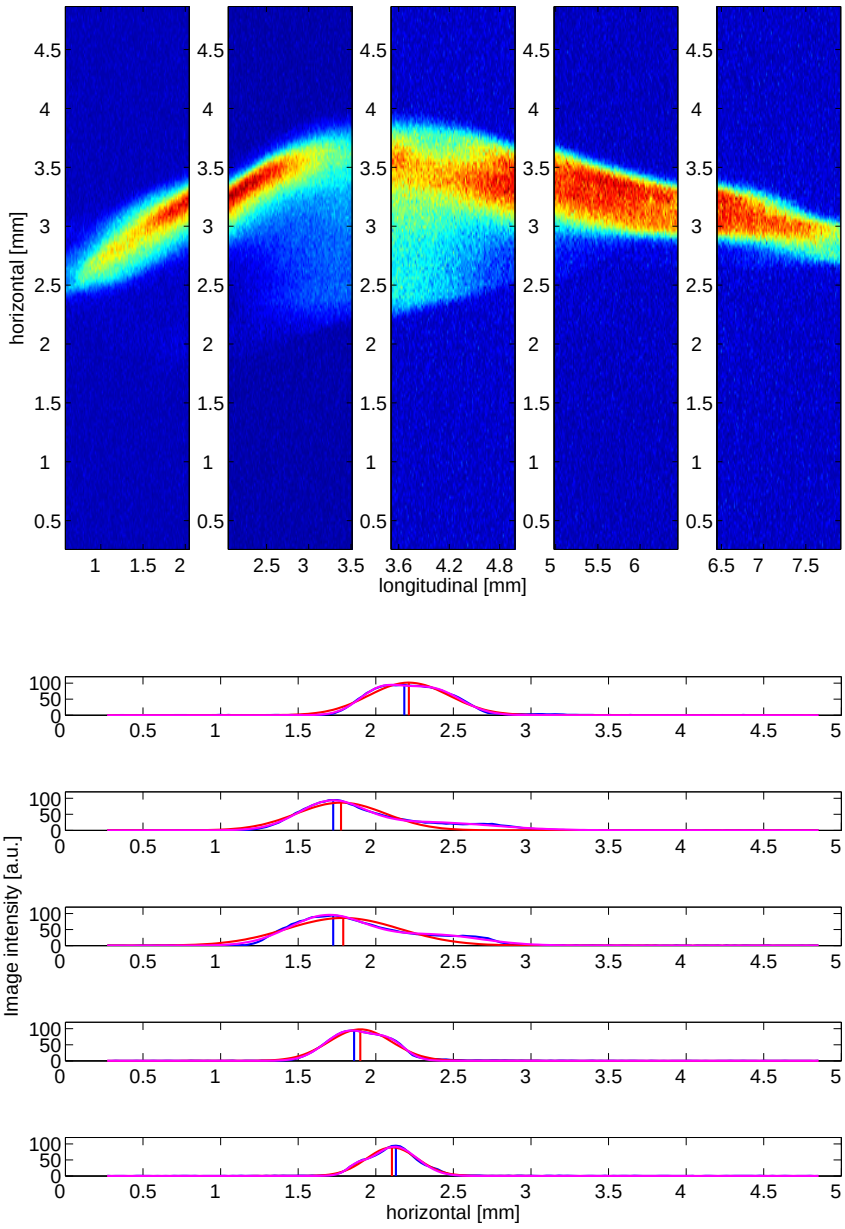

Figure 5.19: Examples of different horizontal slice charge profiles along a bunch. The blue curve is the projection from the pictures, the red shows the Gaussian fit and the magenta line gives the result of a double Gaussian fit. The maxima of the projection and the centres of the Gaussian fits are shown as vertical lines.

position. It is close to the maximum but more stable than the position of the maximum value (Fig. 5.19).

The centre position of each slice together with the mean of its longitudinal position defines the centroid curve. The centroid curves corresponding to different fit methods are shown in Fig. 5.18.

In general, the bunch does not line up exactly parallel to the screen axis. A discussion of this tilt is given in Appendix B. We assume that the tilt is independent of the CSR effects. Therefore, the linear correlation of the different centroid curves, as indicated by the coloured lines in Fig. 5.18, is subtracted.

Let us again take a look at the projections (see Sec. 5.2.5). The "banana" shape of the bunch is clearly visible on the images for charges lower than 1 nC. At higher bunch charges the profiles are more distorted. One observes a stronger beam tilt, and that the longitudinal position of the shifted centroids along the bunch moves toward the head. Finally the beam profiles are "blown up", especially at the longitudinal positions where the centroids are shifted. The image analysis procedure has to be modified to handle the beam images for high bunch charges.

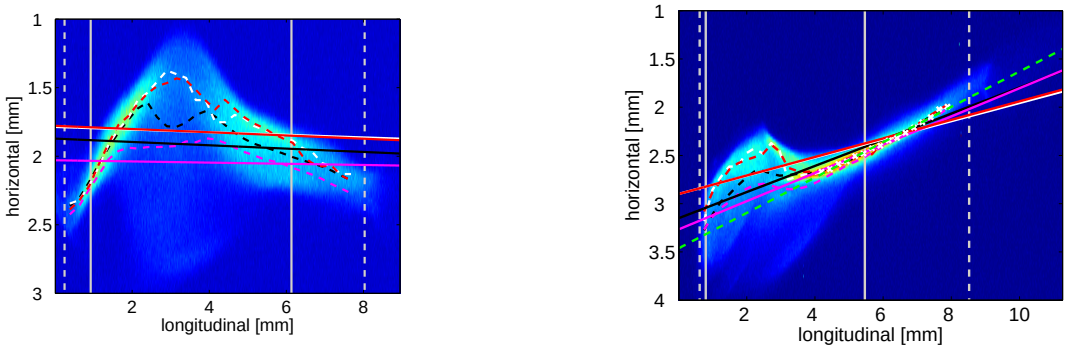

Figure 5.20: (left) Linear correlations, calculated from the centroid curves determined with different methods (red - double Gaussian, white - maximum, black - Gaussian, and magenta - mean) are almost parallel in this low charge $q = 1.0$ nC image. (right) Linear correlations, calculated from the centroid curves determined with different methods are not parallel in this high charge $q = 1.8$ nC image. A slope line (green dashed line) obtained by using only parts of the centroid curve (white crosses) is plotted as well. Bunch head is to the left.

In the lower charge cases with (< 1 nC) the banana shape of the beam profile is longitudinally symmetric around the point of maximum transverse offset. The slope is almost independent of the CSR induced sag. Therefore, the linear slopes of the different centroid curves are almost parallel (Fig. 5.20). This is not true in the cases with higher charges. In this cases the point of maximal transverse offset is close to the head of the bunch. Therefore the slope is dependent on the CSR induced centroid shift (see Fig. 5.20). As a result the slopes determined with different methods, are not parallel.

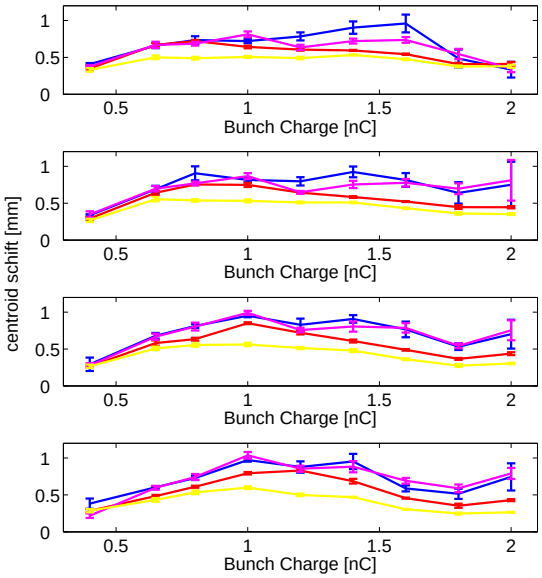

Figure 5.21: A summary of centroid shifts determined with different methods as a function of ACC1 phase and bunch charge are shown here. From top to bottom the ACC1 phase offsets are $22.7°, 23.8°, 24.9°$, and $26°$. The centroid shifts are calculated from centroid curves obtained with different methods (double Gaussian fit in blue, Gaussian fit in red, maximum in magenta, and mean in yellow).

Since the CSR effects contribute to the slope, one underestimates the centroid offset by subtraction of the linear correlation.

Assuming that the CSR perturbation of the beam profile is restricted to one part of the beam one can determine the linear correlation of the centroid curve only in the unaffected region. Subtracting this slope does not underestimate the centroid shifts.

After subtraction of the tilt the horizontal peak to peak shifts of the centroid curves are calculated. A summary of these data is shown in Fig. 5.21.

Fig. 5.22 is a summary of the image analysis. We observe a nearly linear increase of the centroid shifts with charge between 0.4 nC and 0.8 nC. In the range of 1.0 nC to 1.5 nC the centroid shifts are almost independent of the charge. For higher bunch charge we observe a decrease of the centroid shifts.

5.3.4 Image Gradient Analysis

Another problem arises with the extended diffuse beam images at high bunch charges. It is challenging to find a proper centroid position in these smeared beam profiles. The

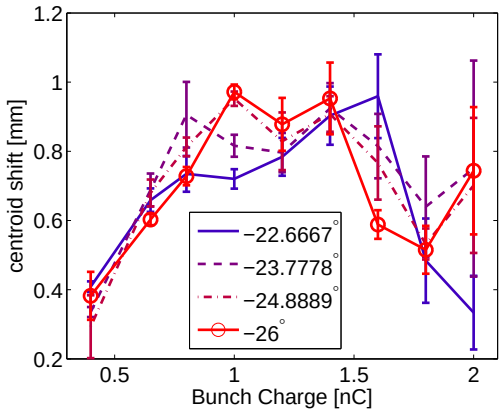

Figure 5.22: Centroid shift vs. charge is presented for different ACC1 phases using the centroid curves determined by double Gaussian fit technique.

beam profiles have a sharp edge on the top side. Our approach is now to define the centroid curve by following the sharp edge that is not disturbed by the widening of the beam. We calculate the gradient of the images to search for the steep ridges in the picture (Fig. 5.23). In a first step we divide the image in a grid. The mean horizontal and vertical component of the gradient is determined for every square in the grid. Each square in which the gradient exceeds a certain threshold is represented by a cross at the centre of mass position of this square. All these dots form the centroid curve. Again a linear correlation is determined and subtracted.

In Fig. 5.24 the centroid shifts are plotted as a function of the bunch charge. Since this gradient method follows the outer fringe of the profiles one over-estimates the centroid shifts due to the beam width. The measured centroid shift from the gradient image analysis σ_{m} is

$$\sigma_{\mathrm{m}} = \sqrt{\sigma_{\mathrm{w}}^2 + \sigma_{\mathrm{cs}}^2}, \tag{5.15}$$

with the beam width σ_{w}, and the real centroid shift σ_{cs}. The centroid shift shown in Fig. 5.24 for the on-crest case is actually dominated by the beam width. They are used as a measure for the beam width σ_{w}, and subtracted quadratically (Fig. 5.24). The high ACC1 phase offset ($24° - 26°$) behave similar. For the lower phase offsets, the decrease at higher charges is not clearly visible. This is related to current spikes which will be discussed later.

The mean centroid sag of all over-compression ACC1 phase offsets vs. bunch charge is plotted in Fig. 5.25. Data obtained using the corrected gradient (see Fig. 5.24) method as well as the slice profile method (see Fig. 5.22) are compared. For bunch charges below 1.5 nC we have a good agreement between data from the slice profile method and the corrected gradient method. For high bunch charges we observe, as expected, a higher centroid shift using the gradient method as from using the slice method. From this comparison one can estimate the systematic error of the centroid shift measurements as

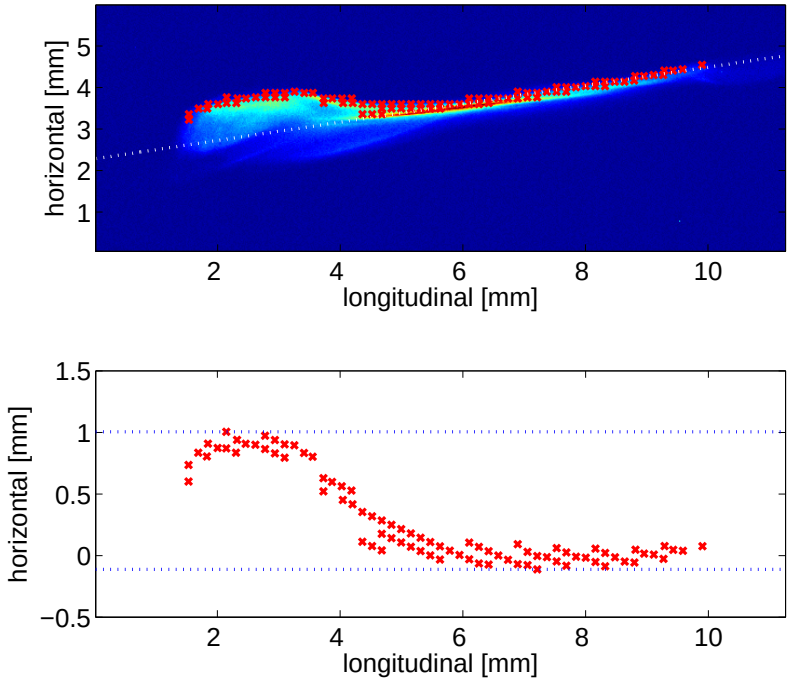

Figure 5.23: In the uppermost picture the beam image and the positions of high gradients are presented. The set of all points of high gradient after subtraction of the linear slope is shown in the lowermost picture.

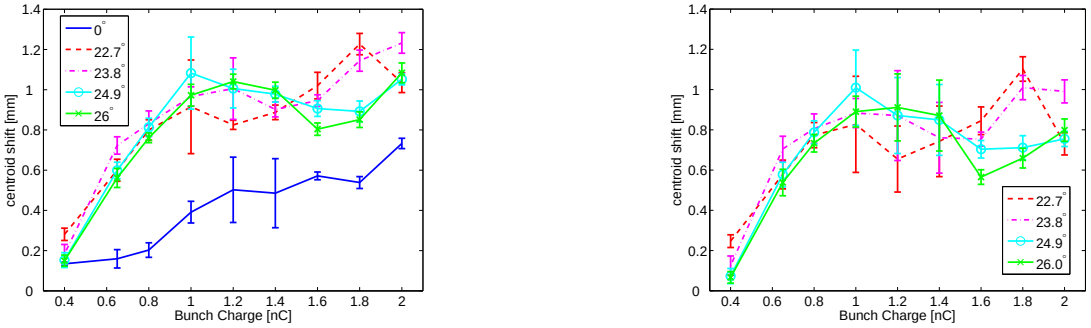

Figure 5.24: (left) Uncorrected centroid shifts as a function of the charge are determined using the gradient method. (right) Corrected centroid shifts using the gradient method. The centroid shift obtained for the on-crest situation is subtracted.

$\sigma_{\text{sys}} \approx 0.1 - 0.2$ mm.

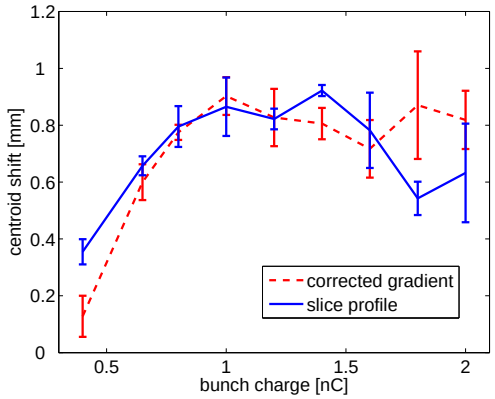

Figure 5.25: A comparison of the mean centroid sag determined with different image analysis methods.

5.3.5 Charge Spikes in Over-Compression

Another feature of the higher-charge pictures are the charge spikes at the head and the tail of the bunch. The reason for these charge spikes is the increased length of the bunch due to space charge effects (see Sec. 5.3.1). A large energy chirp is required to completely over-fold the bunch, to completely exchange the head and the tail. However it was not possible to achieve higher off-crest phases during our experiments while maintaining proper beam transport. Longer bunches will obtain more additional correlated energy spread from the modules ACC2 and ACC3 to the initial longitudinal chirp from ACC1, which is flipped after BC2. In Fig. 5.26 one sees a simulation of a long bunch that is not completely over-compressed compared to a shorter bunch.

The charge spikes indicates a high peak current. Therefore we have to be careful in the interpretation of the experimental data, since the initial assumption that the charge density is low outside the chicanes is not true. In first order, space charge forces are proportional to the derivative of the charge density along the bunch which increases their strength at sharp spikes. Therefore, one would expect a high value of the measured centroid shift for bunch charges higher than $q = 1.6$ nC due to these additional self-interactions. The space charge and wake fields created by these additional charge spikes explain the more "blown up" shape of the high charge beam images, at least qualitatively.

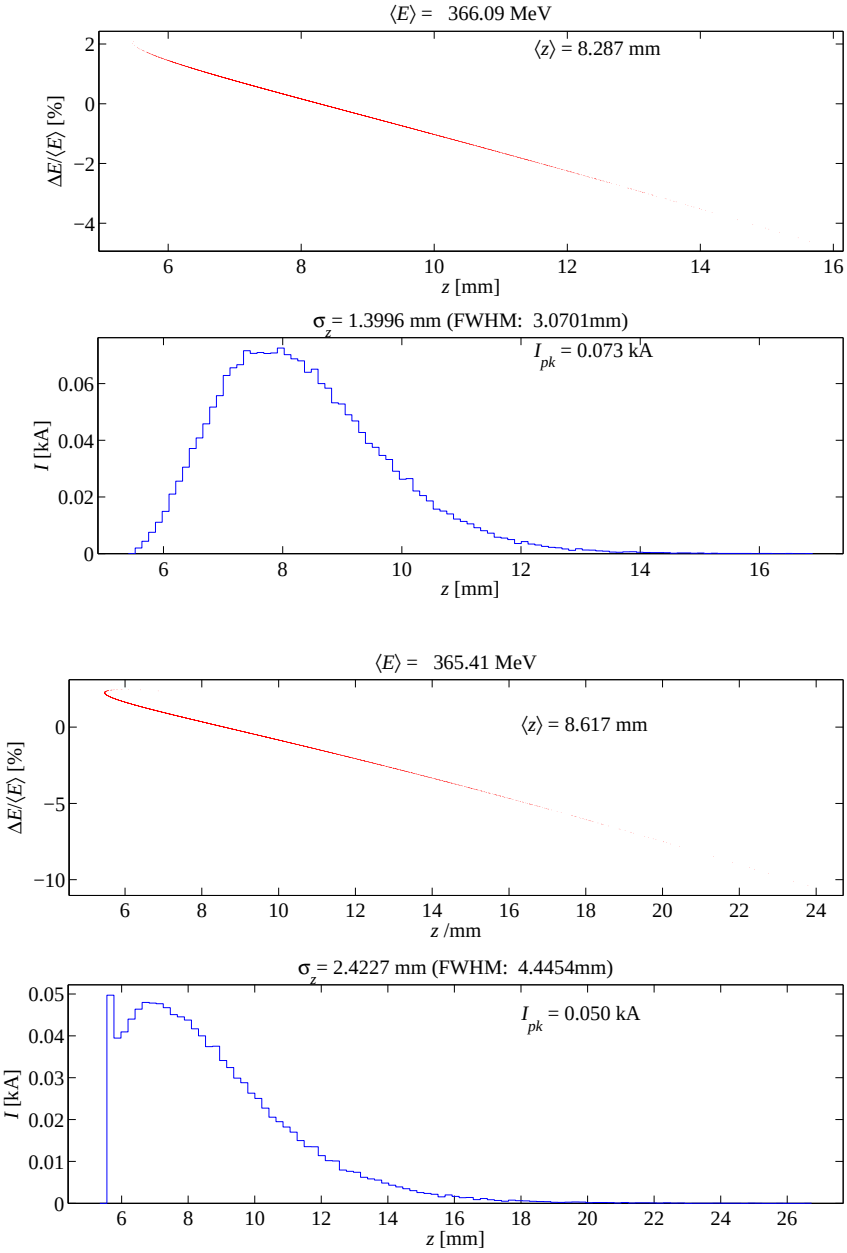

Figure 5.26: The longitudinal phase space and charge profile after BC3 is shown here for different initial bunch length. All accelerating modules are set on-crest except for ACC1 which is $\varphi_{\mathrm{ACC1}} = -20°$ off-crest. The cases of $\sigma = 1.5$ mm (top) and $\sigma = 2.5$ mm (bottom) corresponds to a low and and a high charge beam profile. A long bunch is not completely rolled over which results in a compressed spike.

5.4 Comparison with Tracking Calculations

Experimentally observed CSR induced centroid shifts are also studied with start-to-end tracking calculations. A comparison of the measurements with the results of simulations reveals information about the physical effects and provides benchmarks for the simulation codes.

In each part of the beamline, the beam properties like the Twiss parameters or the emittance are subject to self-interactions. One has to follow the evolution of all those properties from the start to the end. It is not sufficient to study one section, e.g. the bunch compressor chicanes, without knowing the upstream history of the beam. Therefore, start-to-end simulations are used. Such simulations include the photo emission process, the acceleration, the bunch compression, and the transport up to the TDS screen. Different tracking codes are used (see Fig. 5.27).

ASTRA is used for the photo emission process including the space charge fields, which are especially important in this low energy regime.

The injector system consists of the photo cathode, the gun RF-cavity, a solenoid system, and the booster accelerating module ACC1. At FLASH the injector is operated in an emittance compensation mode [Ser97]. This is achieved through finely tuned compensation of space charge with focusing forces. A correct setup of the RF-gun parameters and the solenoid system is therefore required in the gun area. This setup is charge dependent due to the space charge dependence. On the other hand, such a set of carefully tuned machine parameters in the simulations is not necessarily a representation of the actual machine state. The gun parameters are not optimised in the simulations for each charge. We started from an optimised gun set-up in the simulations for the initial bunch charge $q = 0.65$ nC. While the charge was changed, like in the experiment, the optics changed. Because of the uncertainties of the real gun state, the optics changes with charge do not exactly match the changes in the simulation. To fix the simulated beam optics to the measured situation of the machine the simulated Twiss parameters $(\alpha_\mathrm{i}, \beta_\mathrm{i})$ downstream of the gun area were matched to the measured values $(\alpha_\mathrm{f}, \beta_\mathrm{f})$ with the linear transformation

$$\begin{pmatrix} x_\mathrm{f} \\ x'_\mathrm{f} \end{pmatrix} = \begin{pmatrix} \sqrt{\frac{\beta_\mathrm{f}}{\beta_\mathrm{i}}}\,(\cos\varphi + \alpha_\mathrm{i}\sin\varphi) & \sqrt{\beta_\mathrm{f}\beta_\mathrm{i}}\sin\varphi \\ \frac{\alpha_\mathrm{i}-\alpha_\mathrm{f}}{\sqrt{\beta_\mathrm{f}\beta_\mathrm{i}}}\cos\varphi - \frac{1+\alpha_\mathrm{i}\alpha_\mathrm{f}}{\sqrt{\beta_\mathrm{f}\beta_\mathrm{i}}}\sin\varphi & \sqrt{\frac{\beta_\mathrm{i}}{\beta_\mathrm{f}}}\,(\cos\varphi + \alpha_\mathrm{f}\sin\varphi) \end{pmatrix} \begin{pmatrix} x_\mathrm{i} \\ x'_\mathrm{i} \end{pmatrix}. \tag{5.16}$$

Twiss parameters are measured in a FODO section downstream of the chicane and transported back to the chicane entrance.

The results of these calculations are used as input for tracking calculations in the first bunch compressor. The code of choice is *CSRTrack*, and the modified *ASTRA* version is used to check the consistency of the results. In order to include the transient CSR field after the exit of the last dipole, the tracking calculations using *CSRTrack* and *ASTRA* are done up to 1 m downstream of the last dipole of BC2. An example of a *CSRTrack* result after BC2 is shown in Fig. 3.17.

Due to the low peak current downstream of BC2 in the the un-compressed (ACC1 on-crest) and the strongly over-compressed ($\phi_\mathrm{ACC1} < -20°$) regime, self-fields are negligible

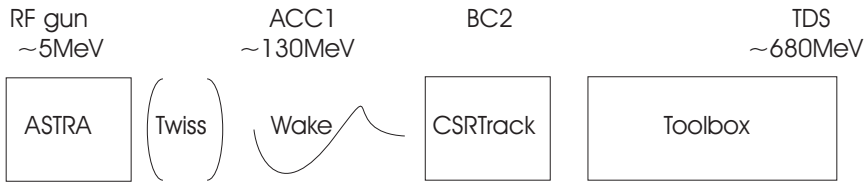

Figure 5.27: Overview of the start-to-end simulations.

Parameters	Value
ASTRA	
macro-particle number	100.000
bunch charge	$0.2 - 2$ nC
RMS emission time	4.0 ps
horizontal spot size σ_x	0.75 mm
vertical spot size σ_y	0.75 mm
Gun peak field	40.0 MV/m
Gun RF off-crest phase offset (rel. to max. energy gain)	$-2.8°$
ACC1 peak field	28.0 MV/m
ACC1 off-crest phase offset	$0 - 26°$
Solenoid peak field	0.163 T
number of radial grid cells	10
number of longitudinal grid cells	15
ratio of the innermost and outermost radial cell height	2.0
mean number of particles emitted per time step	100
CSRTrack	
number M of particles in the position averaging(see Sec. 4.2.2)	5000
sub-bunch length width	$0.5 \cdot$ (RMS bunch length)
beam energy	108.5 MeV
bending radius in BC2	1.601 m

Table 5.4: Parameters of the *ASTRA*(up to exit ACC1) and *CSRTrack*(BC2) runs.

to first order. We, therefore, rely on a linear matrix approach. For these calculations we use the FLASH optics model [Balandin].

Wake fields are added as an additional force as discrete kicks in the middle of each acceleration module. The longitudinal wake at the longitudinal position $s > 0$ behind a short bunch [Wei03][Dohlus]

$$w_{\parallel}(s) = 344 \cdot 10^{12} e^{-\sqrt{\frac{s}{1.74 \cdot 10^{-3}\mathrm{m}}}} \left[\frac{\mathrm{V}}{\mathrm{C} \cdot \mathrm{module}}\right], \tag{5.17}$$

which is convoluted with the charge profile of the bunch. We used the particle distribution at the exit of an acceleration module to determine this charge profile. This procedure is justified by the fact that this longitudinal profile is stable in the accelerating modules. Space charge forces do not disturb the beam because the energy is increasing rapidly and the longitudinal dispersion is negligible. The transverse wake field of a short bunch is obtained from

$$w_{\perp}(s) = 10^{15} \left(1 - \left(1 + \sqrt{\frac{s}{0.92 \cdot 10^{-3}\mathrm{m}}}\right) e^{-\sqrt{\frac{s}{0.92 \cdot 10^{-3}\mathrm{m}}}}\right) \left[\frac{V}{C \cdot m \cdot \mathrm{module}}\right], \tag{5.18}$$

which is convoluted with the charge profile of the bunch and multiplied with a horizontal beam offset [Wei03]. In this model, the transverse wake field is thus proportional to the transverse position offset in the accelerating module (see Appendix C).

Since the beam orbit in the real accelerator is more complicated than in the idealised simulations one has to incorporate spurious dispersion and the orbit offsets into the tracking model. No reliable data on the orbit and the dispersion are available for the situation during the TDS-CSR experiments. Therefore, one has to assume reasonable transverse beam position offsets to model the transverse wake fields and the dispersion. The quadrupole changes made in order to match the beam optics in DBC2 lead to orbit changes which were not systematically corrected during the measurements. One expects a non-ideal situation of beam orbit offsets and spurious dispersion. Other studies on orbit errors and spurious dispersion [Pra06] give a reasonable upper limit estimate of these effects (details on the estimated values are given in Sec. 5.4.2). Orbit errors up to ≈ 10 mm and spurious dispersion up to ≈ 200 mm have been measured in 2006 [Pra06].

Cavity misalignment and cavity tilts inside an acceleration module yield a similar strength in transverse wake fields with a lower beam offset. On the other hand, the effect of the transverse wake fields and of horizontal dispersion is similar. After overcompression, the bunch tail has a lower energy than the head. The highly correlated energy spread along the bunch thereby leads to a horizontal shift of the bunch tail. Effects of transverse wake fields therefore include contributions from horizontal dispersion. Images from the TDS can not distinguish between these contributions.

Vertical dispersion leads to changes in the longitudinal profile observed at the screen after the TDS because the TDS streaks the longitudinal beam axis in vertical direction. Therefore, one can not distinguish between vertical dispersion at the TDS and errors in the longitudinal dispersion of the transport matrices or phase errors in ACC2-ACC5. The assumed vertical dispersion is a combined property of all these effects.

In this sense, the vertical dispersion and the horizontal beam position offset assumed in these simulations are effective parameters, which can not be directly identified with the real properties of the beam orbit during the measurements.

From transverse space charge forces, we expect only effects on the local slice emittance around the bunch head, as the distorted beam images in these cases indicate, but not on the global centroid curve of the beam. Longitudinal space charge forces combined with dispersion can led to transverse effects on the beam. Estimations of these forces (see Appendix C) give an upper bound of ≈ 20 keV/m for the space charge accelerating field, in most cases the field is much weaker. This is, in general, small compared to an energy change induced by CSR in BC2 of ≈ 120 keV (see Fig. 3.20) even if integrated along the accelerator. In our study on centroid shifts, space charge interactions are, therefore, not included in the simulations downstream of BC2.

The tracking calculations for different charges are the basis for a comparison with the measurements (Tab. 5.4). Centroid curves are extracted from the simulated macro-particle distributions. This is done by sorting the particles along the longitudinal axis and dividing them into slices of constant particle number. From each slice the longitudinal and horizontal mean position is calculated. Together they define the centroid curve. The peak-to-peak width of the centroid curve is used to determine the centroid shift. In order to confirm the validity of the image analysis used to analyse the experimental data, images are created from the simulated macro-particle distribution and treated with the same image analysis algorithms (see Sec. 5.4.1). The last step of the analysis is a comparison of the centroid curves obtained from measurements with simulations (see Sec. 5.4.2).

5.4.1 Comparison with Simulated Images

To compare the simulated centroid curves with the measurements, we have to check whether the methods used to determine the centroid curves from the images are valid or not. We calculate beam images from the particle distributions obtained in simulations by a convolution of the particle positions in the longitudinal-horizontal plane with two dimensional Gaussians. The total image intensity is normalised to the bunch charge.

To simulate the minimum intensity observable with the camera system, a lower threshold of charge density is used in the image calculation. An image intensity threshold is chosen as a charge density $\rho(T)$ for a given charge T. The intensity of each pixel is reduced by $\rho(T) = T/(\text{total number of pixels})$, while negative values are set to zero. Therefore, T represents the maximum total bunch charge that is not visible in the camera system, if it is uniformly distributed on the whole screen.

These simulated pictures are analysed with the same image analysis routines that are used for the measured pictures. Since the simulated beam images are smooth and not heavily distorted at the high charge heads, we do not use the gradient image analysis method here.

Simulated beam images are summarised in Fig. 5.28 for charges from $q = 0.4$ nC to $q = 2.0$ nC. For large bunch charges, one observes a concentration of beam intensity in the head of the bunch. The measured charge profiles disagree in the cases from

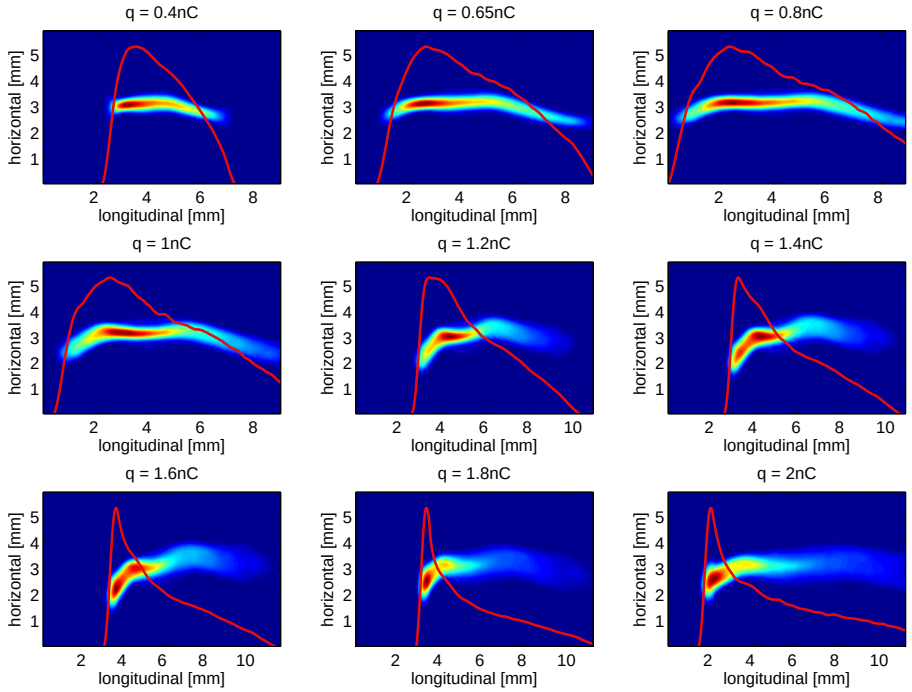

Figure 5.28: Beam images at the TDS obtained by simulations. ACC1 phase offset is $\phi = 24.9°$. Bunch charge is 0.4 nC, 0.65 nC, 0.8 nC, 1.0 nC, 1.2 nC, 1.4 nC, 1.6 nC, 1.8 nC and 2.0 nC from top left to bottom right. Charge profile is indicated by the red line. Intensity threshold $T = 2.0$ nC. Bunch heads are to the left (compare with Fig. 5.12).

$q = 1.6$ nC to $q = 2.0$ nC with the measured ones (compare Fig. 5.12). Self-field effects after BC2, which are not included in the simulations, lead to an increase of beam width in the head region of the bunch (compare Sec. 5.3.5). Since the image intensity is low in the fringes of the "blown up" regions, one expects an underestimation of the measured charge by cut-off effects in the camera system.

A comparison of the total centroid shift determined using the image analysis tools and the centre of mass method is done for different values of the artificial threshold introduced in the image calculation (Fig. 5.29). The qualitative behaviour of the centroid shifts determined from the images and from the macro-particle distribution agree. Since some tails of the beam profiles are cut at the image boundaries one gets lower values than given by the full macro-particle distribution. A higher image intensity threshold leads to a reduction of the centroid shifts because of the reduction of the low charge tails. A threshold charge of $T = 2.0$ nC for the whole screen is chosen as a maximum limit, higher cutoffs are assumed to be not reasonable. This corresponds to a camera setup which is

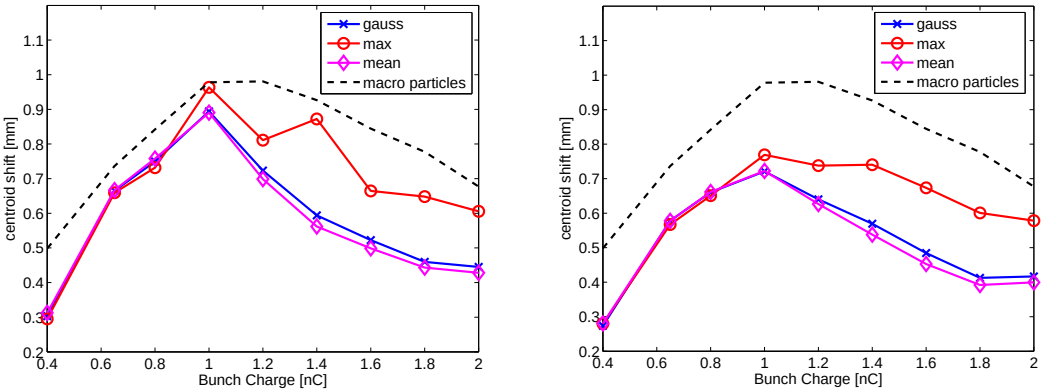

Figure 5.29: The maximal centroid shift determined with the image analysis of simulated images is compared with data obtained from the macro-particle distribution. The centroid curves from the macro-particle distributions are determined by calculating the centre-of-mass in a set of slices along the bunch. Each slice in this calculation was set up to contain a constant number of particles. Image intensity threshold $T = 1.0$ nC (left) and $T = 2.0$ nC (right).

not sensitive to a 2.0 nC beam defocused on the whole screen. From the comparison of both methods we conclude the validity of the image analysis process.

The centroid shifts obtained by an image analysis of the measured data (see Fig. 5.25) are compared with the results from simulated images and with data obtained directly from the macro-particle distribution (compare Fig. 5.29). Due to the uncertainty of the image intensity cutoff threshold T a range between $T = 0.0$ nC and $T = 2.0$ nC is considered. As pointed out earlier the maximal slice centroid offset is used as a measure for the strength of the CSR effects on the beam. As shown in Fig. 5.30 the simulations and the measurements agree qualitatively.

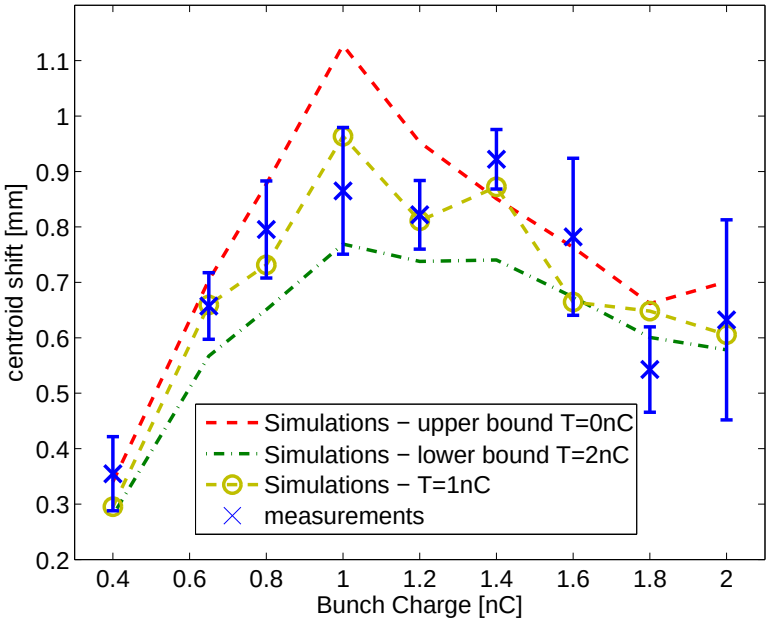

Figure 5.30: CSR induced centroid shifts as a function of bunch charge. The measured centroid shift is plotted and compared with the simulated one obtained from the image analysis for three different image intensity cutoffs. The maximum method in image analysis is used here. Because there is no noise in the simulated images we do not need to use the double Gaussian fit.

5.4.2 Comparison of Centroid Curves

As a final step not only the maximal centroid shift but the shape of the centroid curve itself is compared with simulations. Centroid curves obtained by simulations are compared with data taken with the transverse deflecting cavity (Fig. 5.31).

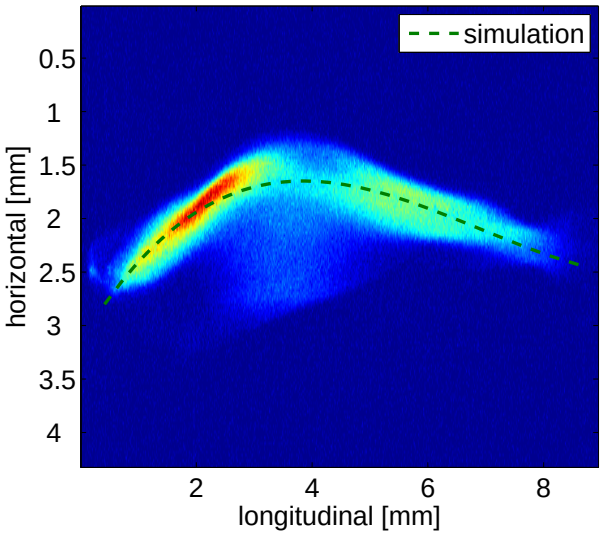

Figure 5.31: Measured beam image of a bunch with 0.65 nC charge running 24.9° off-crest in ACC1. The simulated curve is obtained by fitting a polynomial of 3rd order to the simulated particle distribution. Bunch head is to the left.

Since the shape of the centroid curves does not strongly depend on the off-crest phase, we restrict the analysis on the $\phi = 24.9°$ case (compare Sec. 5.2.5). From the particle distributions obtained by start-to-end simulations, one determines the centroid curves before BC2, after BC2, and at the TDS (Fig. 5.32).

A comparison of the measured and simulated centroid curves is summarised in Fig. 5.33. The measured curves are determined, using the Gaussian method described earlier. Error bars are determined as the standard deviation using the set of 20 pictures taken at each machine setting and a systematic error of the image analysis algorithm. This systematic error is estimated by a comparison of the centroid curves from the transverse slice profile method and the image gradient method (see Sec. 5.3.4).

Different self-field effects act on the beam and cause additional distortions downstream of BC2. A model of transverse wake fields in the acceleration modules ACC2 and ACC3 is included to simulate the observed beam tilt (compare Eq. 5.18 and Appendix B).

In the low charge cases ($q \leq 1.0$ nC) the centroid curves compare well with the simulated data. We have already seen that the over-compression which should lead to low peak currents after the chicanes is not completely achieved in the high charge ($q > 1.4$ nC) cases.

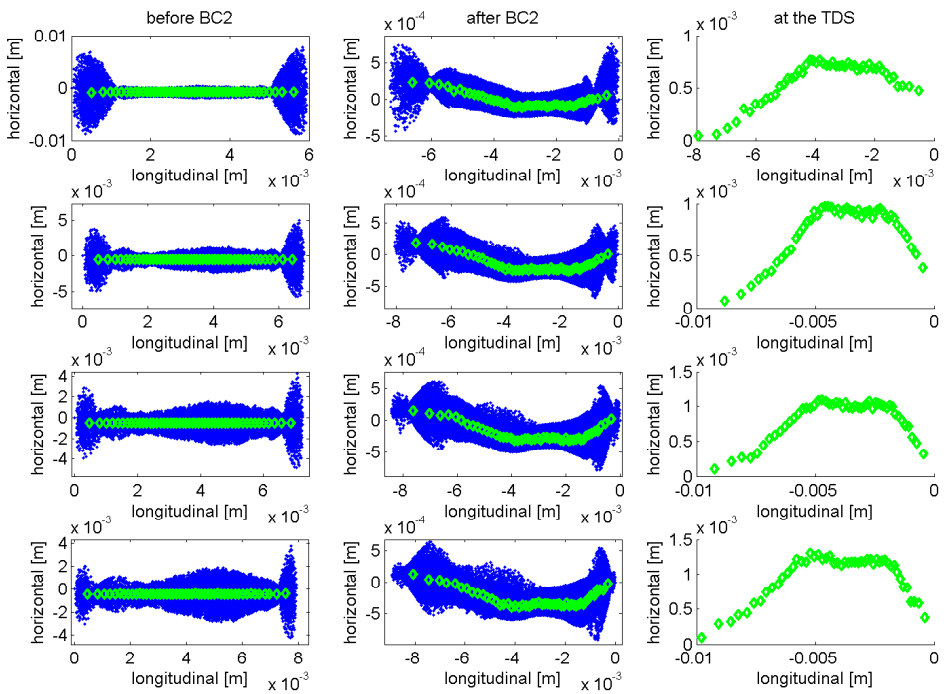

Figure 5.32: Left column : Particle distribution obtained from *ASTRA* simulations at the end of the first accelerating module ACC1. Representative particles along the centroid positions are selected (green diamonds). The same particles are shown at the end of the first bunch compressor chicane BC2 (middle column) obtained by *CSRTrack* calculations. On the right hand side are the same particles transported to the TDS using a linear transfer matrix approach. The bunch charges are 0.4 nC, 0.65 nC, 0.8 nC, and 1.0 nC from the first to the last line. Wake fields and transverse dispersion is not included in this calculations. Bunch heads are to the right.

As discussed in Sec. 5.4.1, by analysing the simulated beam images, the low intensity tails of the beam images do not contribute to the measured centroid curve. These tails are omitted in this comparison of simulated and measured centroid curves.

With the assumptions in Tab. 5.5 the simulated centroid curves can be matched to the measured ones (Fig. 5.33).

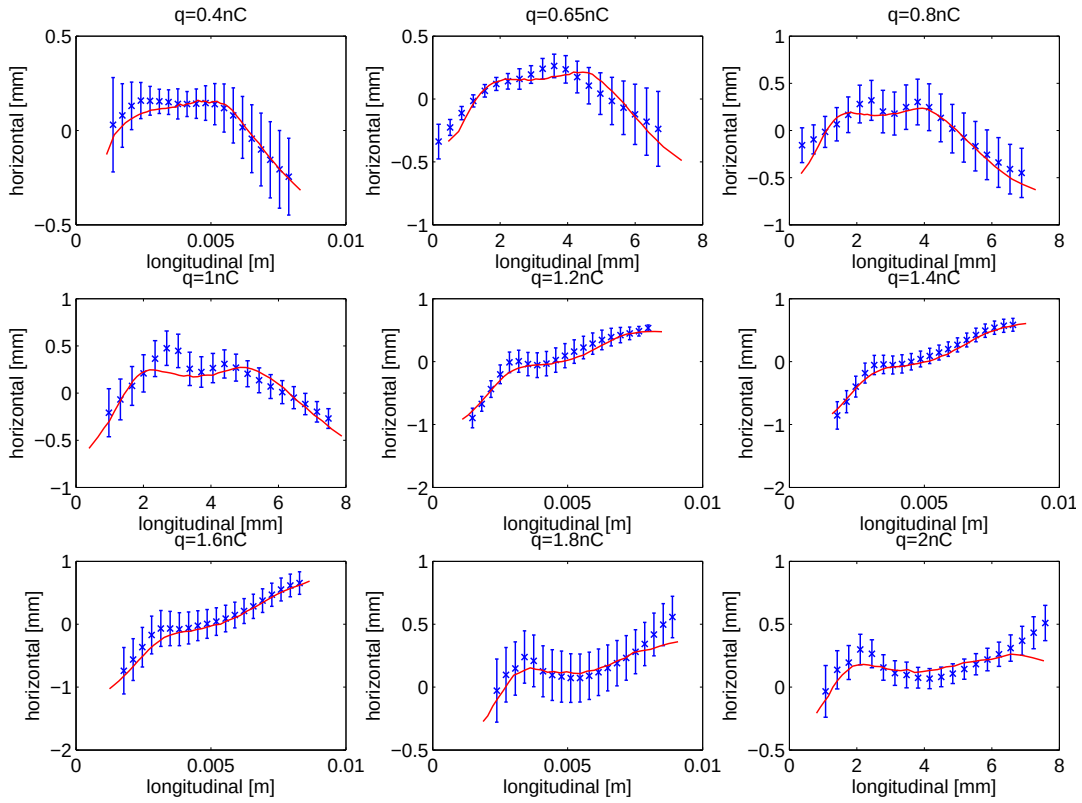

Figure 5.33: Comparison of centroid curves obtained from measurements (blue) and simulations (red). ACC1 phase offset is $\phi = 24.9°$. The centroid curves obtained by the image analysis of measured profiles are shown (compare Sec. 5.4.1). Bunch heads are to the left.

Bunch charge	hor. offset [mm]	η_y [mm]
0.4	0	-200
0.65	0	0
0.8	0	100
1.0	0	0
1.2	-20	-200
1.4	-20	-200
1.6	-20	-200
1.8	-5	-200
2.0	-2	0

Table 5.5: Assumed values of the horizontal beam offset at ACC2/ACC3, and the vertical dispersion $\eta_y = \frac{\Delta y}{\delta}$ used to match the measured centroid curves in Fig. 5.33.

6 Summary and Outlook

SASE FELs, like FLASH, rely on high quality electron beams with a small transverse emittance, small energy spread, and high current. Low emittance bunches are produced at FLASH in an RF gun. The peak current produced by the gun is limited due to space charge forces. Bunches are therefore compressed longitudinally before they pass through the FEL undulators. Dispersive beam lines with an energy dependent path length are one possibility to reduce the length of ultra-relativistic electron bunches. Two magnetic chicanes at FLASH, BC2 and BC3, are used to compress the electron beam in two stages.

A big concern in bunch compressor chicanes is the coherent synchrotron radiation (CSR) which is generated by the electrons in the bending magnets. The longitudinal CSR field redistributes the energy non-uniformly along the bunch. Due to the resulting chromatic effects the transverse projected and slice emittance grow in the chicanes. For the understanding and optimisation of the electron beam, reliable data on the effects of such self-interactions are important. The impact of CSR forces was investigated through numerical simulations and experiments. A first direct observation of CSR effects on electron beams was done at FLASH.

In this thesis, the particle tracking code *ASTRA* was extended to allow for studies of bunch compressor chicanes. As a first step, dipole fields were included in the field calculations. Since the most important effects of CSR interactions are the longitudinal forces and since the numerical effort required for CSR calculations is rather high, we included a 1D CSR field model into *ASTRA*. With this modification *ASTRA* is able to treat the FLASH linac with reasonable accuracy. Only more detailed studies require the use of other codes like *CSRTrack*.

We did extensive studies on the beam dynamics of FLASH using both numerical simulations and experiments. The transverse deflecting RF-structure was used to obtain time-domain images of the bunch. Distortions of the bunch are observed with this transverse deflecting cavity. Start-to-end simulations of the beam dynamics provided data which qualitatively agree with the measured transverse-longitudinal profiles of the bunch. The overall effects on the beam are complicated due to a commingling of different self-field effects, like space charge, CSR, and wake fields.

A quantitative comparison of CSR simulations and measurements was done with a dedicated experiment. In this experiment the bunch was over-compressed in the first bunch compression chicane (BC2), leading to strong CSR effects only in the 2nd dipole, where the peak current reaches its maximum of about 1 kA. The bunch is decompressed afterwards, mitigating further self-field effects downstream in the beam line. The energy loss throughout the bunch can be observed as a horizontal sag on the TDS screen. The measurement was performed for different bunch charges to compare parameter dependencies with those predicted by theory and simulations. The magnitude of the effect is

expected to be up to 130 keV, leading to a trajectory offset of up to 1 mm after the bunch compressor chicane. With proper settings of the optics between the chicane and the TDS (involving 4 more accelerating modules, the 2nd bunch compressor, diagnostic and matching sections) the sag in the longitudinal-horizontal beam profile is of the same order. The sag (i.e. the largest offset of the slices from the nominal position) is derived for different bunch charges. The sag gets smaller for large bunch charges because the bunch length and the uncorrelated energy spread at the entrance of the bunch compressor increases, resulting in a smaller maximal peak current inside the chicane.

A numerical model of the FLASH linac with the same conditions as the real machine was constructed. Despite the limited knowledge of all machine parameters, a satisfactory agreement between numerical results and experimental data was achieved. We demonstrated that the numerical tools as well as the beam diagnostics at FLASH are suitable for quantitative studies on CSR. Techniques to overcome difficulties like the complicated beam transport from the chicanes to the TDS are available.

The layout for the European XFEL contains transverse deflecting structures downstream of each bunch compressor. The difficulties with a long transport between the bunch compressors and the transverse deflecting structure do not appear. Problems, like the integrated space charge distortions of the beam or general uncertainties of the transfer functions are negligible. Therefore, more detailed and precise measurements on CSR effects will be possible. The proposal to have a transverse deflecting structure after each chicane allows for detailed and comparable studies with different beam energies and uncorrelated energy spreads of the bunch.

The centroid shift measurement method developed in this thesis proved a valuable tool in the analysis of CSR effects. More studies of CSR effects are possible using this method. The agreement with simulations provides a valuable benchmark of the available tracking codes on CSR forces. Such a test is important since these codes are used for the design of future free electron lasers and electron linacs such as the European XFEL, or the International Linear Collider. The measurements and simulation results obtained allow for a better understanding of beam dynamics and can be a good basis for the further investigation of CSR interactions and beam dynamics.

A FLASH Parameters

Parameters	30 nm option	6 nm option	Unit
beam energy	450	1000	MeV
bunch charge	$0.5 - 1$		nC
peak current	$1.3 - 2.2$		kA
RMS normalised emittance (slice)	$1.5 - 3.5$		mm mrad
bunch spacing	$1.6 - 3.5$		μs
number of bunches in a train	up to 1800		#
repetition rate	up to 10Hz		#
undulator period	2.73		cm
undulator peak field	0.47		T
averaged beta-function	4.5		m
effective undulator length	27		m
radiation wavelength	30	6	nm
Power gain length	0.7-0.9	1.1-1.6	m
Saturation length	18-22	22-32	m
energy per radiation pulse	50-150		μJ
radiation pulse duration	15-50		fs
radiation peak power	2-4		GW
radiation average power	up to 2		W
spectrum width (FWHM)	0.8	0.4-0.6	%
radiation spot size	180-270	120-180	μm
radiation angular divergence (FWHM)	70-80	25-35	μrad

Table A.1: Parameters of the FLASH SASE FEL [Sal04].

Parameters	Value	Unit
RMS bunch length after the Gun	1.4	mm
RMS bunch length after BC2	0.58	mm
RMS bunch length after BC3	0.43	mm
peak current after the Gun	35	A
peak current after BC2	330	A
peak current after BC3	900	A
ACC1 compression phase	-8.5	deg
ACC2 and ACC3 compression phase	0.0	deg

Table A.2: Nominal parameters of bunch compression in the case of $q = 0.5$ nC bunch charge.

Parameters	Symbol	Value	Unit
Bend magnet length (projected)	L_B	0.5	m
Drift length B1-B2 and B3-B4 (projected)	ΔL	0.5	m
Drift length B2-B3	ΔL_c	0.963	m
Bend radius of each dipole magnet	R	1.65	m
Bending Angle	θ_0	17.64	deg
Momentum compaction	R_{56}	-172.9	mm
2nd order momentum compaction	T_{566}	+259.35	mm
Total projected length of chicane	L_{tot}	3.963	m

Table A.3: Parameters for the first bunch compressor chicane at FLASH BC2, a four bend chicane.

Parameters	Symbol	Value	Unit
Bend magnet length (projected)	L_B	0.5	m
Drift length B1-B2 and B5-B6 (projected)	ΔL	2.38	m
Drift length B2-B3 and B4-B5 (projected)	ΔL	0.5	m
Drift length B3-B4	ΔL_c	5.26	m
Bend radius of each dipole magnet	R	5.3	m
Bending Angle	θ_0	5.45	deg
Momentum compaction	R_{56}	-99.369	mm
2nd order momentum compaction	T_{566}	+149.05	mm
Total projected length of chicane	L_{tot}	14.02	m

Table A.4: Parameters for the second bunch compressor chicane at FLASH BC3, a six bend S-shape chicane.

B Beam Tilt

B.1 Measurements

Even in the on-crest case, one observes a beam which is not lined up horizontally. The strength of the beam tilts can be determined by analysing the linear slope of the centroid curves, as done in Sec. 5.3.2.

Fig. B.1 shows the dependence of the observed linear slope as a function of the ACC1 phase offset for different bunch charges in the over compression regime. One observes a dependence of the slope on the ACC1 phase offset.

The linear slope is plotted for varying bunch charge in Fig. B.2 for different ACC1 phase offsets. In the on-crest case the slope increases slightly with bunch charge. The effect is, however, stronger in the off-crest case. This points to dispersion as a contribution to the total beam tilt. From the correlated energy spread of $\delta \approx 3\%$ and a total projected tilt of $\Delta x \approx 2$ mm we estimate the transverse dispersion required as $\eta = \frac{\Delta x}{\delta} \approx 7$ cm. This a a possible value, but no dispersion measurements were done during the experiments. The fact that a beam tilt is observed even on-crest requires additional effects to explain the tilts.

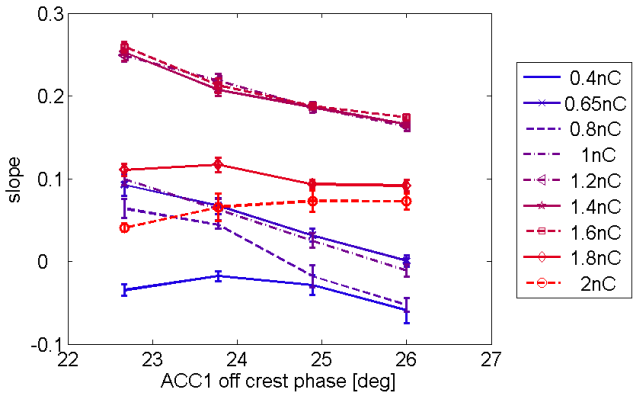

Figure B.1: Beam tilt slopes vs. ACC1 compression phase for different bunch charges.

Further possible reasons are electromagnetic kicks induced by the RF-couplers, wake fields within the module, and a superposition of these effects.

M. Röhrs observed beam tilts as well and is further investigating them (downstream of BC2) [Roehrs].

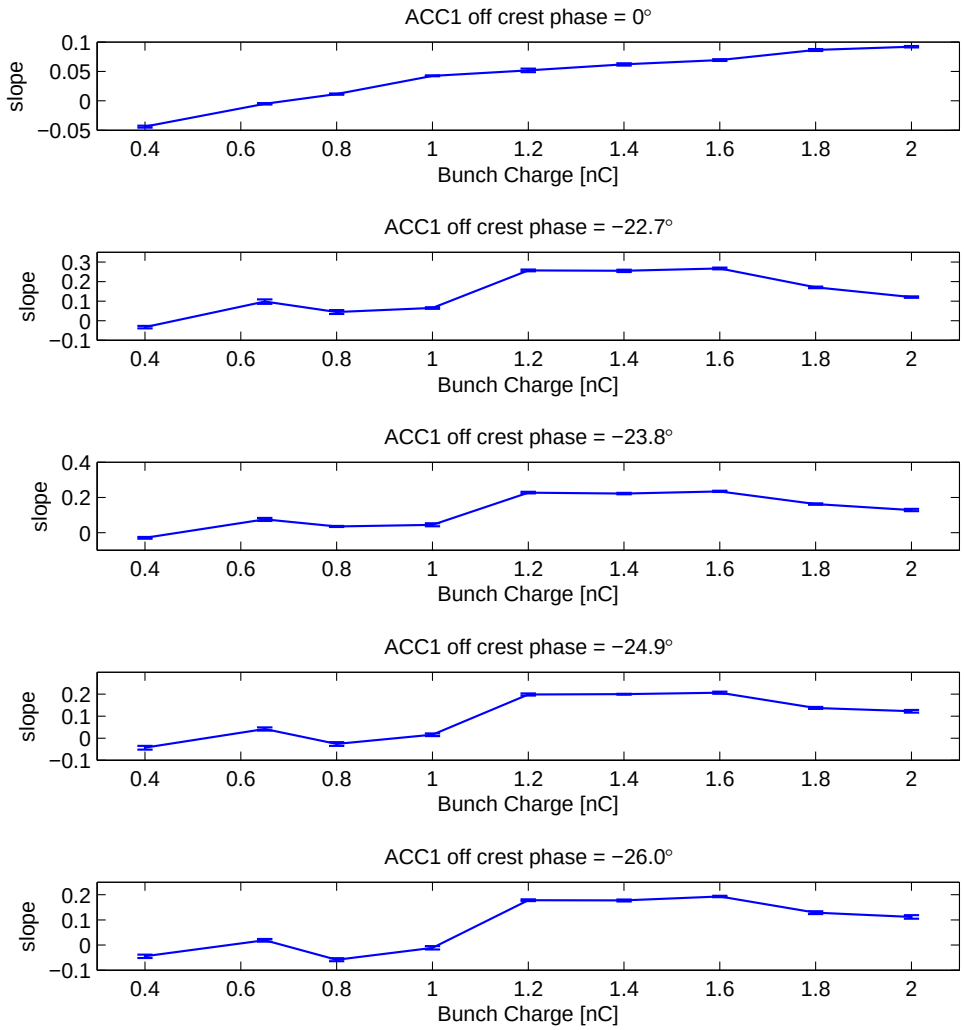

Figure B.2: A summary of beam tilts determined with the Gaussian method as a function of ACC1 phase and bunch charge. From top to bottom the ACC1 phase offsets are $0°, 22.7°, 23.8°, 24.9°$, and $26°$.

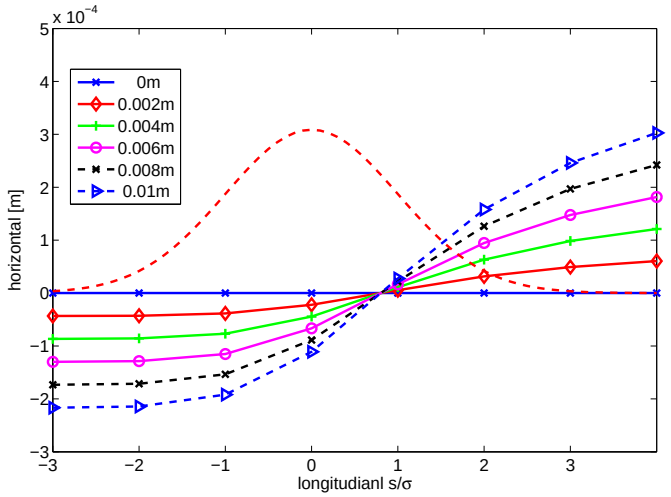

Figure B.3: Centroid curve for different horizontal beam offsets at ACC2 at the TDS screen. Bunch charge is $q = 0.5$ nC with a bunch length $\sigma = 1.5$ mm and a Gaussian longitudinal bunch profile (red dashed line). Bunch head is to the left.

B.2 Transverse Wake Fields

Transverse wake fields can also explain the beam tilt. Horizontal wake fields (Eq. 5.18) of a Gaussian bunch are applied as the bunch is tracked through the FLASH model (Sec. 5.4). Different horizontal beam position offsets in ACC2 and ACC3 and bunch charges are used for this calculations.

The tail of the bunch receives a horizontal displacement as the horizontal beam offset in the acceleration modules increases (Fig. B.3).

To this centroid curves a linear function is fitted. This linear slope is evaluated as a function of the beam offset in the modules. In Fig. B.4 the linear slope as a function of beam offset and bunch charge is compared. The values estimated from this simple model have a reasonable order of magnitude. Since the orbit during the measurement is not well known one can not finally state wether the transverse wake fields are the reason for the observed beam tilt or not. But since the strength of these effects has the right order of magnitude we consider the transverse wake fields to have an important contribution to the beam tilt.

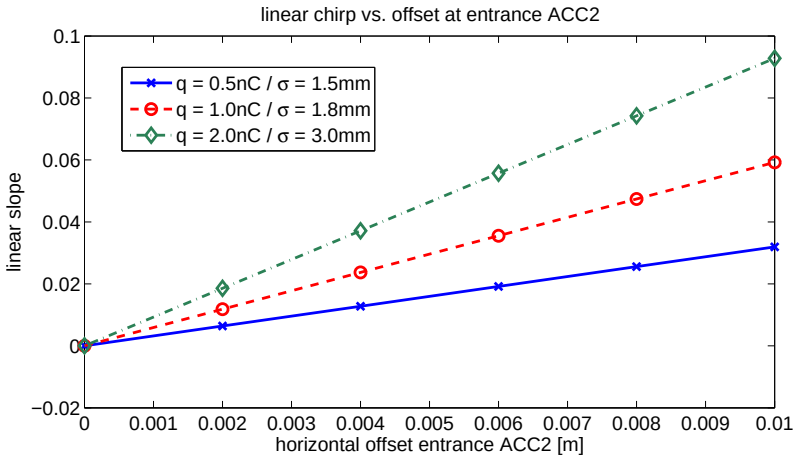

Figure B.4: Simulated beam tilt slopes vs. horizontal beam offsets at ACC2 determined by a linear fit to the curves in Fig. B.3. Different bunch charges, resulting in different bunch lengths, are compared.

C Wake Field and Space Charge Effects

Beam self-interactions of the beam downstream of BC2 are considered as a perturbation to the beam optics calculations (compare Sec. 5.4). Wake fields of the acceleration modules downstream BC2 are calculated with Eq. 5.18 and Eq. 5.17 using the bunch charge profile from the unperturbed beam transport simulations. The results are summarised in Fig. C.1 for different bunch charges downstream of BC2 and BC3.

While the transverse wake fields have an direct effect on the horizontal centroid curve (compare Sec. B) the effects of the longitudinal wakes are negligible. The total energy change induced by longitudinal wake fields on the order of $\approx$ 100 keV per module is comparable to the energy change induced by CSR in BC2 of $\approx$ 120 keV (see Fig. 3.20) but the transverse dispersion in the bunch compressor is by orders of magnitude higher than in the acceleration modules.

A 1D model is used to estimate the strength of the longitudinal space charge force contributions. Longitudinal space charge forces are calculated by

$$E_{long} = \frac{1}{4\pi\varepsilon_0\sigma_r^2}\int_{-\infty}^{\infty}\lambda\left(z-vt-\xi\right)F\left(\frac{\xi\gamma}{\sigma_r}\right)d\xi, \tag{C.1}$$

with the form factor

$$F(u) = \frac{\mathrm{sign}(u)}{2} - \frac{u\sqrt{\pi}}{4}\exp\left((u/2)^2\right)\mathrm{erfc}\left(u/2\right), \tag{C.2}$$

the beam radius σ_r, and the charge profile λ [Dohlus][Gel06]. In case of a Gaussian bunch profile this is equivalent to the equation given in Sec. 3.2.1.

As done before for the determination of the wake fields, the charge profiles from the unperturbed tracking calculations are used for the space charge field calculation. The longitudinal space charge fields are weak compared to the wake fields and therefore neglected in the start-to-end simulations.

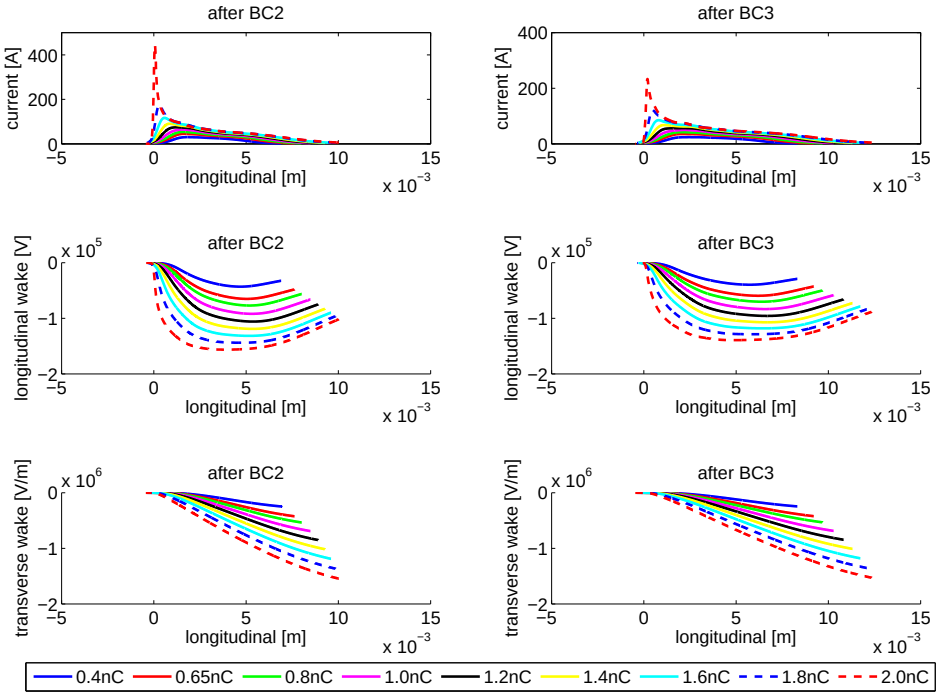

Figure C.1: Beam current profiles (top) of bunches with different charges after BC2 and BC3. The longitudinal (middle) and transverse (bottom) wake field is calculated from the bunch charge profile. Bunch head is to the left.

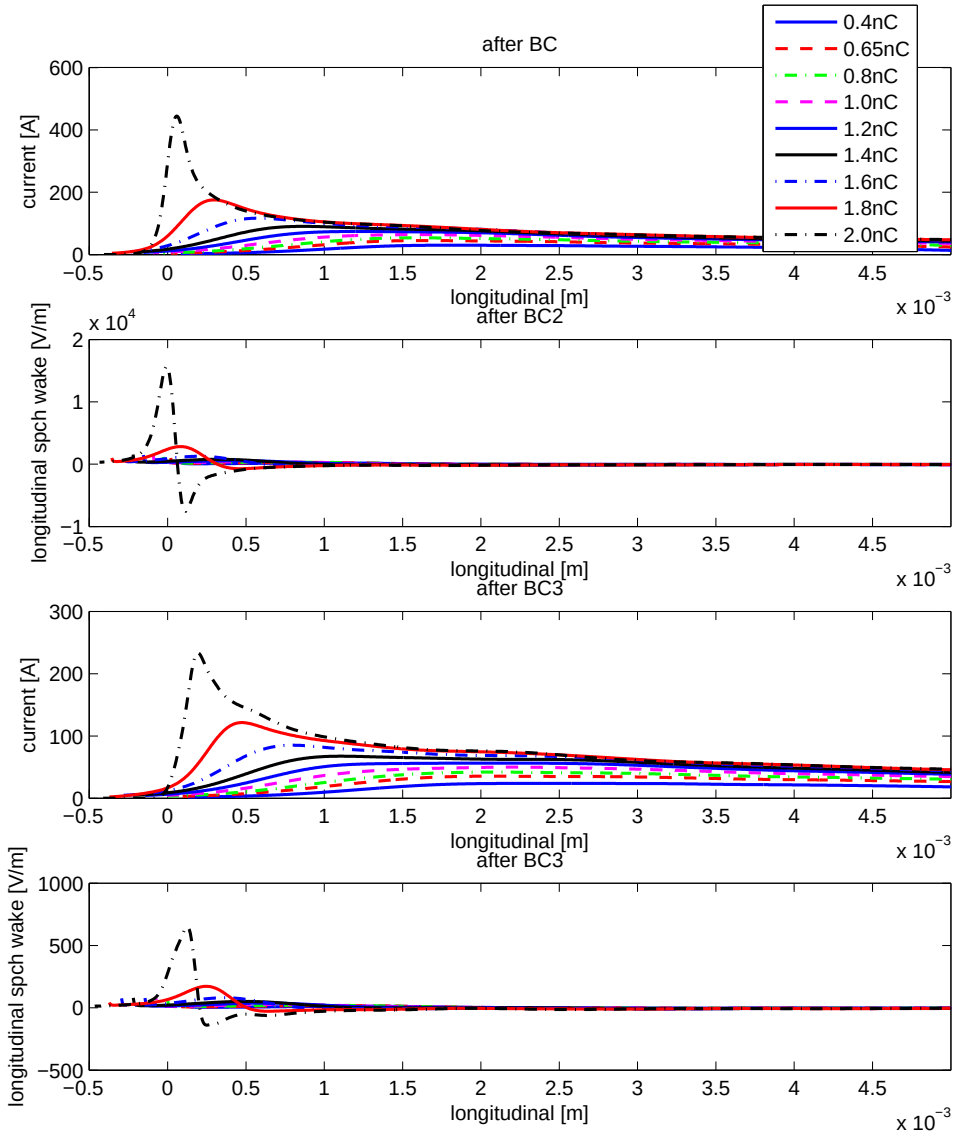

Figure C.2: Beam current profiles and longitudinal space charge fields of bunches with different charges after BC2 and BC3. Bunch head is to the left. RF is set on crest in all the modules axcept for ACC1, which is -26 ° off crest.

D Orbit Decomposition

A decomposition of an electron orbit (compare Section 4.3.3) is done by finding the intersections with the field boundaries of the dipoles and determining the arc length between the intersection points.

D.1 Straight Sections

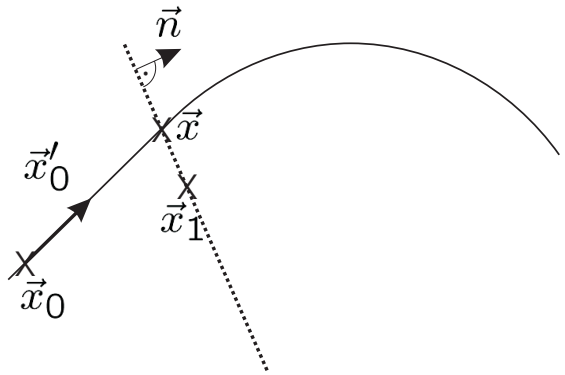

Figure D.1: An electron moving on a straight line from $\vec{x}_0$ in direction $\vec{x}'_0$ until it hits the field boundary at $\vec{x}$. $\vec{x}_1$ is a point on the field boundary and $\vec{n}$ a normal vector perpendicular to it.

A point $\vec{x}(s)$ on a line beginning at $\vec{x}_0 = (x_0, y_0)$ with a direction of $\vec{x}'_0 = (x'_0, y'_0)$ is given by

$$\vec{x}(s) = s\frac{\vec{x}'_0}{\|\vec{x}'_0\|} + \vec{x}_0 \tag{D.1}$$

at a distance s to the start.

For the intersection between $\vec{x}(s)$ and a dipole edge which is given by a point $\vec{x}_1 = (x_1, y_1)$ and a normal vector $\vec{n} = (nx, ny)$ of the edge line we use

$$\vec{\aleph} \cdot \vec{n} = 0 \tag{D.2}$$

for a vector $\vec{\aleph}$ parallel to the edge line (compare Fig. D.1). If $\vec{x}(s)$ is on the field boundary we write with $\vec{\aleph} = \vec{x}(s) - \vec{x}_1$

$$(\vec{x}(s) - \vec{x}_1) \cdot \vec{n} = 0 \tag{D.3}$$

$$\left(\left(s\frac{\vec{x}'_0}{\|\vec{x}'_0\|} + x_0\right) - \vec{x}_1\right) \cdot \vec{n} = 0 \tag{D.4}$$

or in components

$$\left(s\frac{x_0'}{\sqrt{x_0'^2+y_0'^2}}+x_0-x_1\right)n_x+ \left(s\frac{y_0'}{\sqrt{x_0'^2+y_0'^2}}+y_0-y_1\right)n_y = 0. \tag{D.5}$$

Therefore $\vec{x}(s)$ is the intersection point if

$$s=\frac{(x_1-x_0)n_x+(y_1-y_0)n_y}{\frac{x_0'}{\sqrt{x_0'^2+y_0'^2}}n_x+\frac{y_0'}{\sqrt{x_0'^2+y_0'^2}}n_y} \tag{D.6}$$

which is always existing if $x_0'n_x+y_0'n_y\neq 0$. The case $x_0'n_x+y_0'n_y=0$ represents a orbit parallel to the field boundary, therefore no intersection is found.

D.2 Arc Sections

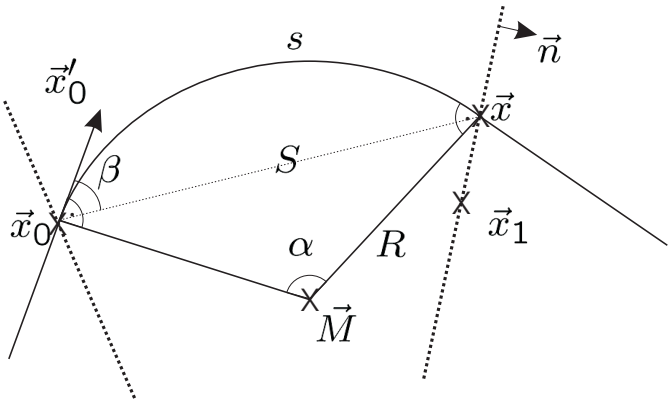

Figure D.2: An electron enters a bending magnet at $\vec{x}_0$ with an initial direction of $\vec{x}'_0$. s is the arc travelled until the electron leaves the dipole at $\vec{x}$. The bending radius R around the centre $\vec{M}$ defines the electron orbit.

Intersections of a circle with a line can by found with the conditions

$$(\vec{x}-\vec{x}_1)\cdot\vec{n} = 0 \text{ and} \tag{D.7}$$

$$\left(\vec{x}-\vec{M}\right)^2 = R^2 \tag{D.8}$$

with $\vec{x}=(x,y)$ an intersection point and $\vec{M}=(M_x,M_y)$ the centre of the circle of radius R. $\vec{n}=(n_x,n_y)$ is the normal vector of the field boundary and $\vec{x}_1=(x_1,y_1)$ a point on

the boundary (compare Fig. D.2). In components one obtains

$$(x - x_1)\, n_x + (y - y_1)\, n_y = 0 \text{ and} \tag{D.9}$$

$$(x - M_x)^2 + (y - M_y)^2 = R^2. \tag{D.10}$$

Combining these equations we get

$$(x - M_x)^2 + \left(y_1 - (x - x_1)\, \frac{n_x}{n_y} - M_y \right) = R^2. \tag{D.11}$$

As a solution set for x we get after some calculation

$$\begin{aligned} x^{1,2} &= m_x n_y^2 + n_x \left(-M_y n_y + n_y y_1 + n_x x_1\right) \pm \\ &\pm \Bigg[- n_y^2 \Big\{ M_y^2 n_y^2 - n_y^2 R^2 - 2 M_y n_y \left(-M_x n_x + n_y y_1 + n_x x_1\right) + \\ &\quad + \left(n_y y_1 - n_x \left(M_x + R - x_1\right)\right) \left(n_y y_1 + n_x \left(-M_x + R + x_1\right)\right) \Big\} \Bigg]^{1/2} \end{aligned} \tag{D.12}$$

From the x component of $\vec{x}$ we get y with

$$y^{1,2} = -(x^{1,2} - x_1) \frac{n_x}{n_y} + y_1 \tag{D.13}$$

using Eq. D.9. From these solutions $\vec{x}^{1,2}$ the one which is nearer to the starting point is selected.

To obtain the arc length s between $\vec{x}$ and the starting point $\vec{x}_0$ one uses (see Fig. D.2)

$$\frac{\sin \alpha}{\sin \left(90^\circ - \beta\right)} = \frac{S}{R} \tag{D.14}$$

$$\frac{\sin \alpha}{\cos \beta} = \frac{S}{R} \tag{D.15}$$

$$\alpha = \arcsin \left(\frac{S \cos \beta}{R} \right). \tag{D.16}$$

The vector $\vec{p} = \frac{\vec{x}_0'}{\|\vec{x}_0'\|}$ is the normalised velocity at the start point of the arc section. With the angle between $\vec{p}$ and $\vec{x} - \vec{x}_0$ is β we find

$$\vec{p} \cdot (\vec{x} - \vec{x}_0) = S \cos \beta. \tag{D.17}$$

Together with Eq. D.16 one gets

$$\alpha = \arcsin \left(\frac{\vec{p} \cdot (\vec{x} - \vec{x}_0)}{R} \right). \tag{D.18}$$

The velocity vector $\vec{x}_1'$ at the end of the bend section is calculated by application of the matrix

$$\vec{x}_1' = \begin{pmatrix} \cos \alpha & -\sin \alpha \\ \sin \alpha & \cos \alpha \end{pmatrix} \vec{x}_0', \tag{D.19}$$

and finally $s = \alpha R$.

E Comparison of 1D and 3D CSR Field Calculation Models

To reduce the numerical effort of CSR calculations one often relies on a 1D projected model for CSR field calculations [Sal97], for instance in the modified *ASTRA* code. These projected models calculate the longitudinal CSR-field from the line charge density of the bunch. Transverse forces as well as space charge contributions are neglected. These contributions are included in 3D full field models like a direct integration of the fields or a 3D greens function approach [Doh03][Doh04b]. In this section the differences of these 1D and 3D models are discussed. For this study a meshed 3D *greens* function and the 1D *projected* model of *CSRTrack* are used [CSRTrack].

E.1 Test Chicane

The magnetic chicane used for these studies consists of four bending magnets. Each magnet is 0.5 m long. The distance between the first and the second magnet is 0.5 m, 1.0 m between the second and the third dipole, and 0.5 m between the third and the fourth bend. Bending radius is $R = 8.4$ m. The resulting longitudinal dispersion is $R_{56} = 6$ mm.

The energy chirp of the electron bunch used for this study is chosen to be almost linear with a small quadratic component to compensate for effects of T_{566} to achieve linear compression. Properties of the electron bunch are given in Tab. E.1 (compare Sec. 4.3.5).

The normalised energy deviation from the reference energy, averaged over all particles, along the chicane with the projected method and the greens function method are compared in Fig. E.1. The average energy loss is underestimated by the 1D method. The energy loss deviates within the dipoles and in the drift between the third and fourth dipole (compare Fig. E.2). The effect which leads to the deviation in the drift space is called compression work, it arises from the beam size variations and the corresponding changes in the potential energies in the space charge field (see Sec. E.2). Transverse effects of the deviation in energy loss within the dipoles are discussed in Sec. E.4.

E.2 Compression Work

The difference between the average energy along the chicane in the greens function method and the projected method of the full chicane are compared with greens function calculations between the third and the fourth dipole without taking the dipoles into

Bunch	
Energy	511 MeV
correlated Energy spread	4.68 MeV
Charge	0.833 C
Bunch length (initial)	72.4 μm
Bunch length (final)	19.3 μm
Peak Current (initial)	800 A
Peak Current (final)	5 kA
normalised Emittance	1 mm mrad
alpha	2.2
beta	10 m
Particle Distribution	
Number of Particles	997
Number of Slices	83
Particles per Slice	12
sub-bunch length	5.3 μm
sub-bunch width (horizontal)	33 μm
sub-bunch width (vertical)	50 μm

Table E.1: Parameters for the comparison studies.

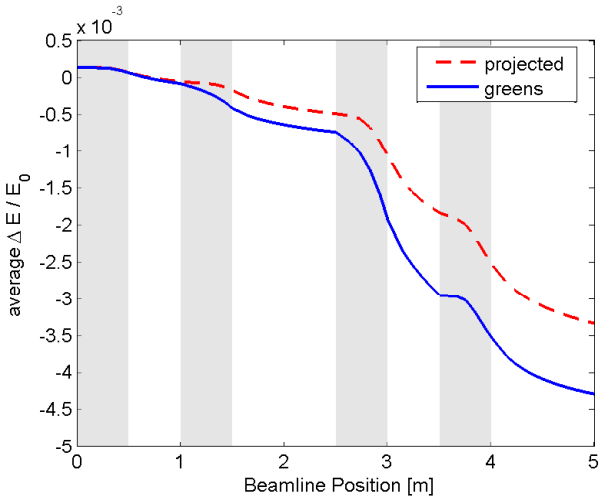

Figure E.1: Energy along the chicane calculated with the projected and the greens function model. Dipoles are indicated by grey boxes.

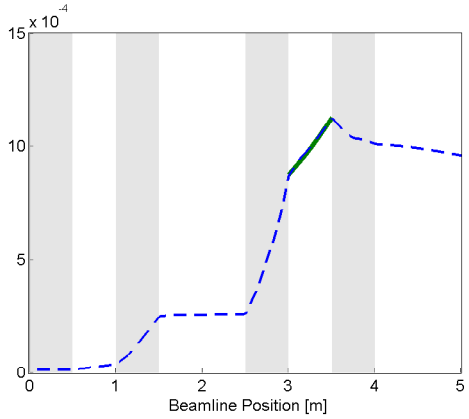

Figure E.2: Difference in energy loss between greens and projected method (blue dashed line). Average energy loss between the third and fourth dipole (green line) is calculated with the greens method without CSR contributions. Dipoles are indicated by grey boxes.

account (see Fig. E.2). In these calculations without the dipoles no transient CSR contributions are included. Since the difference in beam energy loss agrees with the 3D simulations without dipoles we conclude that space charge, and not transient CSR interactions are the important factor here.

The bunch length in the drift space between the third and the fourth dipole is minimal. Therefore, the space charge field is expected to reach its highest value along the chicane in this region. A change in horizontal beam size is correlated with the average energy loss (compare Fig. E.3). Since the beam is returning to its original width with diminishing horizontal dispersion, the potential energy in the space charge field increases.

For a Gaussian beam, we calculate a lower limit for the exchange of kinetic energy and electro-magnetic field energy in the longitudinal plane for the case of adiabatic compression. In a beam pipe with radius R, the electromagnetic field energy for $\gamma >> R/\sigma_z$ is approximately [ICFA05]:

$$W \approx \frac{q^2}{4\pi^{3/2}\varepsilon_0\sigma_z} \ln\left(\frac{R}{1.5\sigma_r}\right) \tag{E.1}$$

q is the bunch charge, σ_z the RMS bunch length, and σ_r the RMS beam radius. In the drift spaces of the chicane the bunch length does not change, to first order, but the transverse beam size change due to the changes of transverse dispersion. The lower limit for the compression work can be estimated by comparison of the initial and the final field energy W_1 and W_2, respectively. $\Delta W = W_1 - W_2$ is the compression work.

Compression work can also be studied for the whole chicane. To do this, we compare the field energy upstream and downstream of the chicane. If the beam is compressed from bunch length σ_{z1} to $\sigma_{z2} = \sigma_{z1}/C$, C being the compression factor, and the transverse beam dimensions are equal before and after compression, then the beam loses kinetic

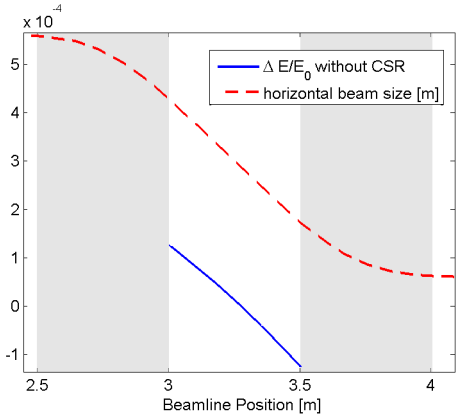

Figure E.3: Horizontal beam size is compared with the average beam energy between the third and the fourth dipole. Dipoles are indicated by grey boxes.

energy: $\Delta W = W_1 - W_2 = (C-1)W_1$.

This is a lower limit, which depends on the assumption of a beam pipe with a certain radius. This lower limit is not necessarily negligible compared to synchrotron radiation energy loss in free space. As an example, if a 1 nC beam with a radius of $\sigma_r = 100$ μm is compressed from 200 μm to 20 μm in a 1 cm round beam pipe, the compression work is $\Delta W = 0.107$ mJ-1.065 mJ$= -0.958$ mJ [Doh02]. For comparison, CSR interactions in a bending magnet with bending radius $R_0 = 10$ m and a projected length of $L = 0.5$ m with a $\sigma_z = 20$ μm long beam lead to a radiated power of $P = 375$ kW and an energy loss of $PL/c0 = 0.625$ mJ [Doh02].

This analysis of the energy profile along the chicane shows that space charge contributions, which are neglected in the 1D model, can have a siginficant effect on the beam energy.

E.3 Over-Compression

In the last section a standard compression scheme was studied. Now the over-compression situation, used in this thesis, is studied. The correlated energy spread is increased to achieve a symmetric over-compression case, so the final bunch length is equal to the initial one. Like in the earlier cases the energy loss is different for both methods (see Fig. E.4). Since the maximal peak current is reached during over-compression the total energy loss is larger.

From the particle distributions the centroid curves are determined by a fourth order polynomial fit (see Fig. E.5). The beam width is shown as error bars. Despite the differences in the energy loss the centroid curves are quite similar in both field calculation models. The transverse beam dynamics are not only described by the dispersion and the energy, but by the transverse forces as well. These forces are neglected in the 1D

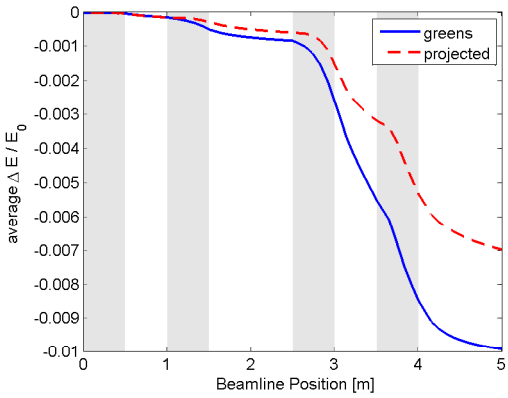

Figure E.4: Energy along the chicane calculated with the projected and the greens function model. Dipoles are indicated by grey boxes.

field model.

E.4 Transverse Effects

The transverse dynamics is not only given by the energy loss and dispersion but also by the transverse forces which are neglected in the projected model. Transverse beam dynamics are described by the equation of motion [Wie03b][Doh03b]

$$x'' + (K^2 - n)x = \frac{K\Delta E + F_x}{E_0}, \tag{E.2}$$

with the quadrupole strength n, the transverse CSR force F_x, and $K = 1/\rho^2$ with the dipole bending radius ρ. The sign of K represents the bending direction. Since ΔE and F_x are the variables in our study we investigate the right hand side of Eq. E.2. This value calculated from the projected method and the greens function method is compared in Fig. E.6. A four bend chicane with dipoles of bending radius $\rho = 10.35$ m, a distance between the first bend and second bend as well as the third bend and fourth bend of $L_o = 5$ m, and a distance $L_i = 1$ m between the second dipole and the third dipole was used. A 500 MeV beam with 1 nC charge is compressed from 200 μm to 20 μm. One notices that the parameter $\frac{K\Delta E + F_x}{E_0}$ is quite independent of the field calculation method. Transverse displacements, induced by the higher energy loss in the greens function model, are compensated by the transverse forces, which are neglected in the projected model. The resulting difference in the transverse dynamic for both models is smaller than expected from the energy loss differences.

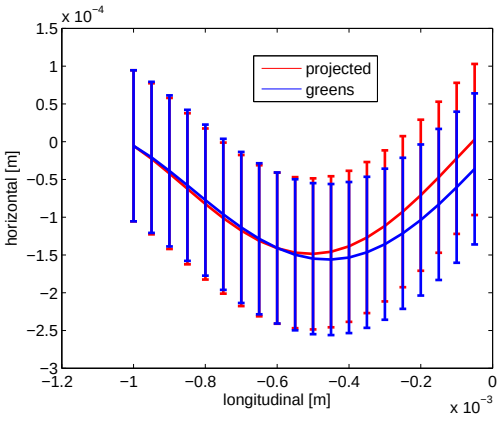

Figure E.5: Comparison of centroid curves. Horizontal beam size is indicated by the error bars.

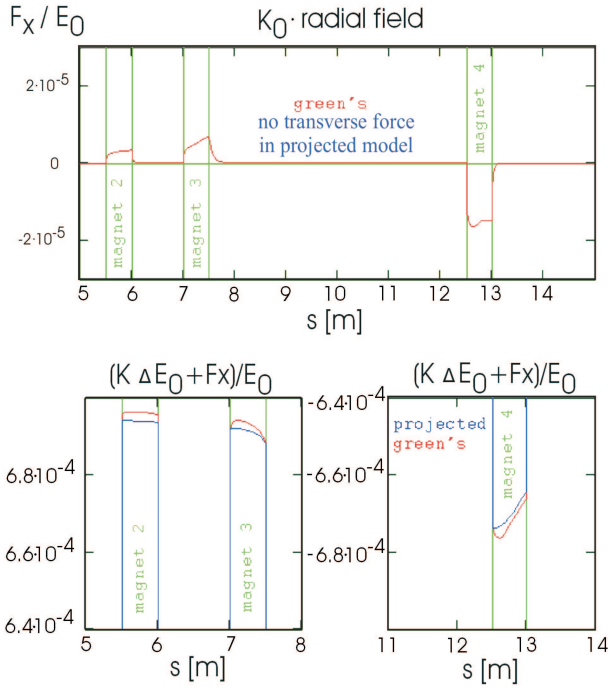

Figure E.6: Comparison of transverse dynamics between the greens function method and the projected method. K_0 is the absolute value of the bending parameter. Figure taken from [Doh03b].

E.5 Conclusion

To choose the appropriate field calculation method one has to estimate the strength of space charge effects. This can be done by calculating the longitudinal space charge (compare Sec. C) integrated along the chicane, and the estimation of the compression work (see Eq. E.1). If these values are well below the correlated energy spread one can use the projected model without large differences in the compression process and, therefore, the final bunch shape.

An upper bound of the transverse deviations between 1D and 3D field calculation methods can be obtained by estimating the energy deviation as above and combine it with the transverse dispersion of the chicane. From Sec. E.4 it is clear that this gives an upper bound, because the transverse CSR forces tend to compensate these effects.

Bibliography

[Ack07] W. Ackermann, G. Asova, V. Ayvazyan, et al. *Operation of a free electron laser from the extreme ultraviolet to the water window.* Nature Photonics, 1:336–342, 2007.

[XFEL] A. Aghababyan, M. Altarelli, C. Altucci, et al. *The European X-Ray Free-Electron Laser Technical Design Report.* DESY XFEL Project Group European XFEL Project Team Deutsches Elektronen-Synchrotron Member of the Helmholtz Association, 2006.

[Alt64] O. H. Altenmueller, R. R. Larsen, and G. A. Loew. *Investigations of Traveling-Wave Separators for the Stanford Two-Mile Linear Accelerator.* Review of Scientific Instruments, 35 4:438–442, 1964.

[And00] J. Andruszkow, B. Aune, V. Ayvazyan, et al. *First observation of self-amplified spontaneous emission in a free-electron laser at 109 nm wavelength.* Phys. Rev. Lett., 85(18):3825–3829, October 2000.

[Ayv06] V. Ayvazyan, N. Baboi, J. Bahr, et al. *First operation of a free-electron laser generating GW power radiation at 32 nm wavelength.* Eur. Phys. J. D, 37:297–303, 2006.

[Balandin] V. Balandin and N. Golubeva. *private comunication.*

[Ban05] K. Bane and P. Emma. *LiTrack: A Fast Longitudinal Phase Space Tracking Code with Graphical User Interface.* In *PAC05, Knoxville, TN*, 2005.

[Beu06b] B. Beutner, W. Decking, M. Dohlus, et al. *Beam Dynamics Experiments and Analysis on CSR Effects at FLASH.* In *FEL 2006 - Proceedings BESSY, Berlin, Germany*, 2006.

[Beu06a] B. Beutner, M. Dohlus, and M. Roehrs. *Beam Dynamics Experiments and Analysis in FLASH on CSR and Space Charge Effects.* In *FLS 2006 - Proceedings Hamburg, Germany*, 2006.

[Bol05] A. Bolzmann. *Investigation of the longitudinal charge distribution of electron bunches at the VUV-FEL using the transverse deflecting cavity LOLA.* Master's thesis, Bayrische Julius-Maximilians Universität Würzburg, 2005.

[Bon84] R. Bonifacio, C. Pellegrini, and L. M. Narducci. *Collective instabilities and high-gain regime free electron laser.* Opt. Commun., 50(6):373–378, July 1984.

[Bor00] M. Borland. *elegant : A flexible SDDS-Compilant Code for Accelerator Simulation.* APS LS-287, September 2000.

[Bro82] K. L. Brown. *A First- and Second-Order Matrix Theory for the Design of Beam Transport Systems and Charged Particle Spectrometers.* SLAC Report-75, 1982.

[MAD] CERN. *MAD-X Home Page.* http://mad.web.cern.ch/mad/.

[Der95] Y. Derbenev, J. R. bach E. L. Saldin, and V. D. Shiltsev. *Microbunch Radiative Tail-Head Interaction.* Technical report, TESLT-FEL 1995-05, 1995.

[Dohlus] M. Dohlus. *private communication.*

[Doh02] M. Dohlus. *Field Calculations for Bunch Compressors - Talk given at the ICFA Future Light Sources Sub-Panel Mini Workshop on Coherent Synchrotron Radiation and its impact on the dynamics of high brightness electron beams.* http://www.desy.de/csr/csr_workshop_2002/talks/m_dohlus/field_calculation_for_bunch_compressors.pdf, 2002.

[Doh03b] M. Dohlus. *Methods for CSR Tracking - Talk given at the ICFA Future Light Sources Sub-Panel Mini Workshop on Start-to-End Simulations of X-RAY FELs.* http://www.desy.de/s2e/Talks/Tuesday/s2eDohlus.pdf, August 2003.

[Doh03] M. Dohlus. *Two Methods for the Calculation of CSR Fields.* Technical report, TESLA-FEL-2003-05, 2003.

[Doh05] M. Dohlus. *CSR Calculation for TTF-II.* http://www.desy.de/xfel-beam/data/talks/talks/dohlus_-_s2e_ttf2_a_20051006.pdf, 2005.

[Doh00] M. Dohlus and T. L. A. Kabel and. *Coherent Effects of a Macro-Bunch in an Undulator.* Nucl. Instr. And Meth. A, 445:84–89, 2000.

[Doh04] M. Dohlus, K. Flöttmann, O. Kozlov, et al. *Start-to-end simulations of SASE FEL at the TESLA Test Facility, phase 1.* Nucl. Instr. And Meth. A, 530:217–233, 2004.

[Doh00b] M. Dohlus, A. Kabel, and T. Limberg. *Efficient Field Calculation of 3-D Bunches on General Trajectories.* NIM A, 445:338–342, 2000.

[CSRTrack] M. Dohlus and T. Limberg. *CSRtrack Version 1.2 Users Manual.* http://www.desy.de/xfel-beam/csrtrack.

[Doh04b] M. Dohlus and T. Limberg. *CSRTrack: FASTER CALCULATION of 3-D CSR EFFECTS.* In *Proceedings of the 2004 FEL Conference, 18-21*, 2004.

[ICFA05] M. Dohlus, T. Limberg, and P. Emma. *Bunch Compression for Linac-based FELs.* ICFA Beam Dynamics Newsletter, 38:15–50, 2005.

[Emm01] P. Emma, J. Frisch, and P. Krejcik. *A Transverse RF Deflecting Structure for Bunch Length and Phase Space Diagnostics.* In *Proceedings of the 2001 Particle Accelerator Conference, Chicago, Illinois, USA*, 2001.

[ASTRA] K. Flöttmann. *Astra User Manual.* http://www.desy.de/~mpy/ astra_dokumentation.

[pASTRA] L. Fröhlich. *A new Astra for parallel computing.* http://tesla.desy.de/~lfroehli/astra/.

[Gel06] G. Geloni, E. Salsin, E. Schneidmiller, et al. *Longitudinal Wake Field for an Electron Beam Accelerated through a Ultra-High Field Gradient.* Technical report, DESY 06-222, 2006.

[Gerth] C. Gerth. *private comunication.*

[Jac98] J. D. Jackson. *Classical electrodynamics*. John Wiley & Sons, Inc., 3rd edition, 1998.

[Mad71] J. M. J.Madey. *Stimulated Emission of Bremsstrahlung in a Periodic Magnetic Field.* Journal of Applied Physics, 42:1906–1913, 1971.

[Knu97] D. E. Knuth. *The art of computer programming, volume 2 (3rd ed.): seminumerical algorithms.* Addison-Wesley Longman Publishing Co., Inc., Boston, MA, USA, 1997. ISBN 0-201-89684-2.

[Kra04] M. Krasilnikov, K. Abrahamyan, G. Asova, et al. *Optimizing the PITZ Electron Source for the VUV-FEL.* In *Proceedings of EPAC 2004, Lucerne Switzerland*, 2004.

[RLi00] R. Li. *Analysis and Simulation on the Enhancement of the CSR Effects.* In *XX International Linac Conf., Monterey, CA*, 2000.

[Lim05] T. Limberg and M. Dohlus. *Impact of optics on CSR-related emittance growth in bunch compressor chicanes.* In *Particle Accelerator Conference (PAC 05) Knoxville, Tennessee*, 2005.

[Lim02] T. Limberg, P. Piot, and F. Stulle. *Design and Performance Simulation of the TTF-FEL II Bunch Compression System.* In *Proceedings of EPAC 2002, Paris, France*, 2002.

[Lim03] C. Limborg, Y. Batygin, M. Boscolo, et al. *Code Comparison for Simulation of Photo-Injectors.* In *Proceedings of the 2003 Particle Accelerator Conference*, 2003.

[Lip04] D. Lipka. *Untersuchungen zum longitudinalen Phasenraum an einem Photoinjektor fü r minimale Strahlemittanz.* Ph.D. thesis, Humbold-Universitä t Berlin, 2004.

[Loe05] F. Loehl. *Measurement of the Transveerse Emittance at the VUV-FEL.* Master's thesis, University Hamburg, 2005.

[Bow04] H. O. M.A. Bowler. *A Study of CSR induced microbunching using numerical simulations.* In *Proceedings of EPAC 2004, Lucerne, Switzerland*, 2004.

[Nag04] M. Nagl. *Physics of the Transverse R.F. Deflecting Structure.* Presentation, DESY, Hamburg, 2004.

[Pfl00] J. Pflüger. *Undulators for SASE FELs.* Nucl. Instrum. Meth A, 445:366–372, 2000.

[Pra06] E. Prat, W. Decking, and T. Limberg. *Measurement and Correction of Dispersion in the VUV-FEL.* In *Proceedings of EPAC 2006, Edinburgh, Scotland*, 2006.

[TESLA] F. Richard, J. R. Schneider, D. Trines, et al. (editors). *TESLA Technical Design Report.* DESY, 2001-011.

[Roehrs] M. Röhrs. *private comunication.*

[Ros06] J. Rossbach. *Results from FLASH.* In *Proceedings of EPAC 2006, Edinburgh, Scotland*, 2006.

[Sal97] E. L. Saldin, E. A. Schneidmiller, and M. V. Yurkov. *On the coherent radiation of an electron bunch moving in an arc of a circle.* Nucl. Instr. and Meth. A, 398:373–394, May 1997.

[Sal99] E. L. Saldin, E. A. Schneidmiller, and M. V. Yurkov. *The physics of Free Electron Lasers.* Springer-Verlag, Berlin, 1999.

[Sal04] E. L. Saldin, E. A. Schneidmiller, and M. V. Yurkov. *Expected properties of the radiation from VUV FEL at DESY (femtosecond mode of operation).* Technical report, Deutsches Elektronen-Synchrotron DESY, Hamburg, 2004.

[Sal05] E. L. Saldin, E. A. Schneidmiller, and M. V. Yurkov. *Statistical Properties of the Radiation from VUV FEL at DESY Operating at 30 nm Wavelength in the Femtosecond Regime.* Technical report, Deutsches Elektronen-Synchrotron DESY, Hamburg, 2005.

[Sch04] S. Schreiber. *Commissioning of the VUV-FEL Injector at TTF.* In *Proceedings of EPAC 2004, Lucerne Switzerland*, 2004.

[Sch96] J. Schwinger. *On radiation by Electrons in a Betatron.* LBNL-39088, July 1996. Transcribed by M.A. Furman.

[Ser97] L. Serafini and J. B. Rosenzweig. *Envelope analysis of intense relativistic quasilaminar beam in rf photoinjectors: A theory of emittance compensation.* Physica Review E, 55:7565–7590, 1997.

[Stu04] F. Stulle. *A bunch compressor for small emittances and high peak currents at the VUV Free-Electron Laser*. Ph.D. thesis, University of Hamburg, October 2004. DESY report DESY-THESIS-2004-041.

[TTF02] The TESLA Test Facility FEL team. *SASE FEL at the TESLA facility, phase 2*, June 2002. DESY report TESLA-FEL 2002-01.

[Wei03] T. Weiland and I. Zagorodnov. *The Short-Range Transverse Wake Function For TESLA Accelerating Structure.* Technical report, TESLA Report 2003-19, 2003.

[Wie03b] H. Wiedemann. *Particle Accelerator Physics I, Basic Prociples and Linear Beam Dynamics*. Springer, 2nd edition, 2003.

[Wie03] H. Wiedemann. *Particle Accelerator Physics II, Nonlinear and higher-order beam dynamics*. Springer, 2nd edition, 2003.

Acknowledgements

First of all, I would like to thank Prof. Dr. Jörg Roßbach for introducing me to the field of accelerator physics and giving me the opportunity to prepare my thesis at DESY. I also appreciate the helpful criticism and support he provided me with.

I am grateful to my supervisors Winfried Decking, Klaus Flöttmann, and Torsten Limberg. You were always there to help me with my experimental and theoretical work. You kept supporting me all the time. Without your help I would not have finished this thesis. Thanks a lot.

I am indepted to Martin Dohlus for many useful discussions about everything ranging from classical electrodynamics to the deep problems of numerical beam dynamics simulations. I learned a lot from your advice and explanations. Your computer codes proved to be a valuable tool for my work.

Thanks goes to Sigfried Schreiber and Bart Faatz for their support and all they told me about FLASH. The whole FLASH Team contributed to this thesis and the measurements. They provided advice, fruitful discussions, and support during the work on this thesis. I would like to thank all operators who were on shift with me during the last years.

Special thanks for Michael Röhrs and Christopher Gerth. The measurements would not be successful without your help. And thanks again Michael for answering all my questions about LOLA, your help, and the nice tools.

Furthermore, I am indepted to Nicoleta Babaoi, Andy Bolzmann, Jean-Paul Carneiro, Hossein Delsim-Hashemi, Lars Fröhlich, Kirsten Hacker, Florian Löhl, Sascha Meykopff, Eduard Prat, and Dmytro Pugachov for letting me keep them from work with endless but productive discussions on various physical and non-physical topics.

Very special thanks goes to Kirsten Hacker, Winfried Decking, and Lars Fröhlich for proofreading this thesis. Kirsten, I hope my english is not too awful. Thank You.

Besonderer dank gilt auch all meinen Freunden. Ihr konntet mir zwar nicht bei der Dissertation helfen, aber ihr habt mein Leben in den letzten Jahren angenehmer gemacht. Auf euch war Verlass auch wenn es mal nicht so gut lief.

Ganz besonders möchte ich mich natürlich bei meinem Bruder und meiner Mutter bedanken, sie haben mich immer unterstützt und an mich geglaubt. Ohne den aufopferungsvollen Einsatz meiner Mutter hätte ich nicht sorgenfrei aufwachsen und studieren können. Ihr verdanke ich mehr als ich in Worte fassen kann.